Experiments on internal wave attractors

with synthetic schlieren

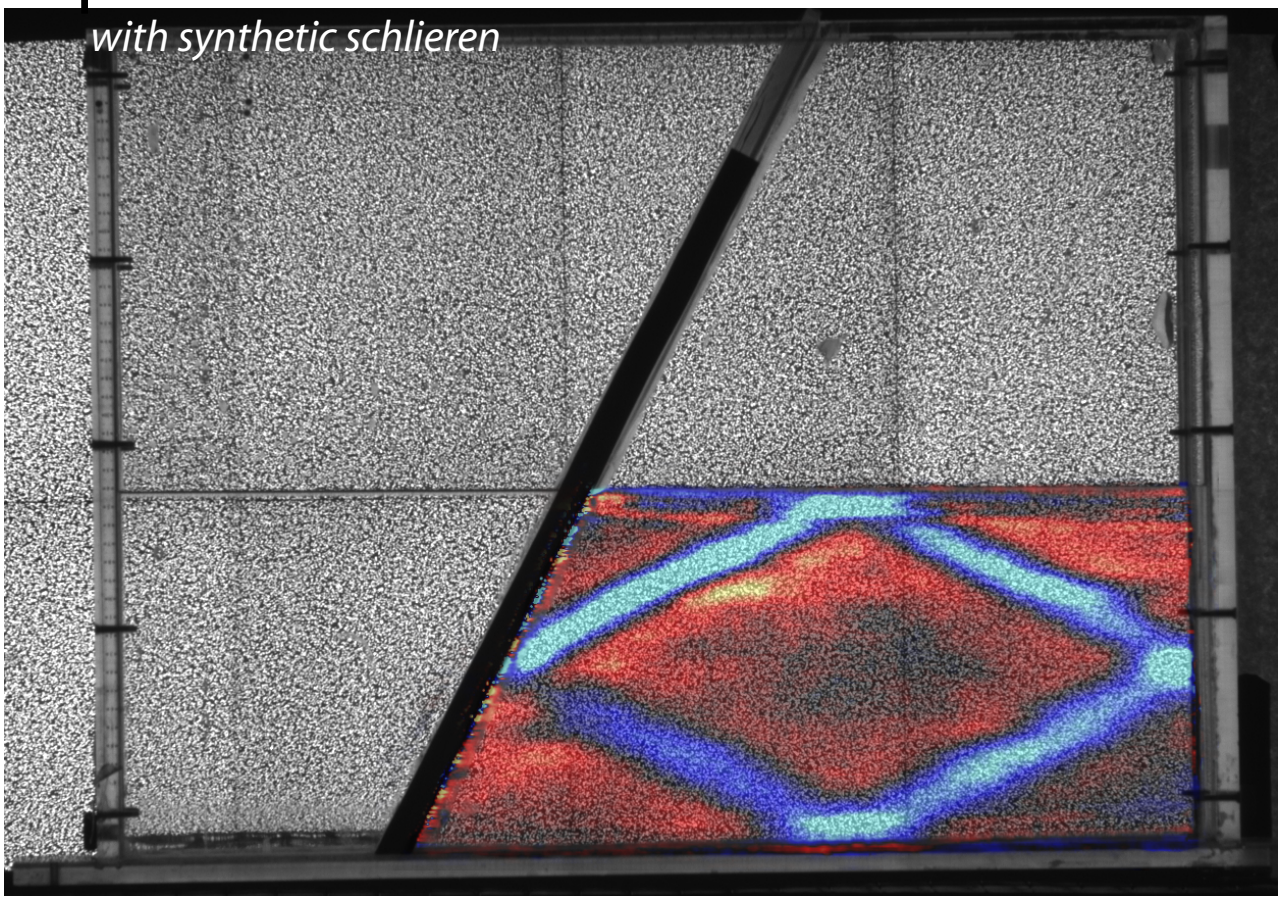

Master thesis Physical Oceanography, Meteorology and Climate
Pieter van Breevoort
August 2007

Supervisors: prof dr. L.R.M. Maas and prof dr. J.T.F. Zimmerman
Institute for Marine and Atmospheric research (IMAU)
Faculty of Science, dep. Physics and Astronomy
Universiteit Utrecht

IMAU
Institute for Marine and Atmospheric research Utrecht

Table of contents

Abstract

Here we present experimental results on internal wave attractors, obtained with synthetic schlieren. The dynamics of internal wave attractors in different geometries and with different frequencies were studied. We applied a mechanical (harmonic) forcing, but parametric (subharmonic) excitation was considered as well. The shape of the observed attractors satisfied the inviscid predictions. The observed temporal evolution from basin-scale waves towards smaller internal waves and the development of an equilibrium spectrum resulted in a simple theoretical model describing this evolution. We show that the shape of equilibrium spectra depends on the attractor length rather than the forcing strength. The influence of a rigid lid was tested, which revealed a diminishing effect on the attractor. The phase and amplitude fields observed in a parabolic channel were found to agree well with those obtained in a previous study with a numerical model. Besides the experimental results and analysis, suggestions for future research are given, related to the experimental set-up.

Used symbols/labels

Overview of symbols and labels employed in this thesis. The sections where they are introduced are indicated. The vertical is defined parallel to the gravitational direction.

symbol/label	description	section
N	buoyancy/Brunt-Väisälä frequency: $N^2 = -(g/\rho_0)(\partial\rho^*/\partial z)$	2.1
T	oscillation period of the platform	3.2.2
A	vertical amplitude of the oscillation of the platform	3.2.2
$\mathbf{b} = (b_x, b_z)$	perturbation density (ρ') gradient relative to the gradient of the unperturbed background stratification ($\rho^*(z)$): $\nabla\rho'/(\partial\rho^*(z)/\partial z)$	3.3.4
"at_xxx"	label of an experiment, numbered chronologically as "xxx"	3.5
H	water depth in the tank	3.4.2
L_a	length at the bottom of side "a" of the semi-2D tank (Fig. 3.6(b)) from "at_50" on $L_a = 14.5$ cm	3.4.2
L_b	length at the bottom of side "b" of the semi-2D tank (Fig. 3.6(b)) from "at_50" on $L_b = 45.3$ cm	3.4.2
α	angle the wave vector makes with the horizontal or the group velocity vector makes with the vertical	2.1
θ	angle of the slope in the semi-2D tank with the vertical, from "at_50", this slope was glued at $\theta = 27°$	3.4.2
stage 1	part of the experiment, when a forcing is applied by the oscillating platform	4.1
stage 2	part of the experiment, starting one period after the forcing has ceased	4.1

CHAPTER 1

Introduction

Internal gravity waves are supported in fluids with a non-uniform density. They can appear as waves propagating along isopycnals, when a fluid contains layers with different densities, or obliquely, when a fluid is continuously stratified. In a confined, stratified fluid, wave attractors can be supported. Wave attractors are closed paths on which an internal wave is focused as it propagates and reflects against the walls, i.e. the baroclinic response localises around a certain path. Here focusing means the decrease of the wavelength of the internal waves upon a reflection. An internal wave attractor was observed by Maas *et al.* (1997) in a laboratory. Movements in the fluid were visualised with dye-lines. Over the last ten years, new optical methods were developed to study fluid dynamics in more detail, among them the synthetic schlieren method. As part of the the project 'Internal Wave patterns in 3D' (IW3D), this technique was used to study internal (gravity) wave attractors. The IW3D-project is carried out by Jeroen Hazewinkel and is part of the NWO-program 'Dynamics of patterns'. The goal of that project is to study internal wave attractors in 3D, both mathematically and experimentally. I have collaborated during some phase of the project, the experimental results of this collaboration are presented in this master thesis. The experiments were performed at GK Batchelor Lab in Cambridge.
In this introduction, I will give an overview of the properties of internal waves and internal wave attractors, and a short (and incomplete) overview of the history of the research in this field.

1.1 Internal Waves

A wave is a travelling disturbance. Waves in fluid mechanics can be classified as mechanical waves, with a fluid as a medium. For waves to appear, the medium must be disturbed. Disturbing a system means to bring a system out of a situation where all forces acting on a fluid are in balance. The forces which are out of balance are the restoring forces. The dominant force acts on the system in such a way, that the system restores to equilibrium, and the dominant force diminishes. Parcels gain velocity and move through equilibrium, and the other restoring force now dominates. This force grows until the potential energy is equal to the energy which was brought in the system by the disturbance. Now the reversed principle occurs. A wave is born. If a part of the energy is converted to heat, by friction, or mixing, the amplitude of the wave fades in time and the system eventually

reaches its equilibrium, though slightly heated and/or mixed. A wave transports energy away from the source. The forces working on a (frictionless) geophysical fluid are gravity, the Coriolis force and pressure gradient forces. Surface waves arise when the force balance at the surface is perturbed. Inertial waves arise if the Coriolis force and the pressure gradient force are out of balance, and gravity waves when gravity and the pressure gradient are out of balance. A mix of these waves is called a inertia-gravity wave. Internal waves arise when force balances are perturbed in the interior of the fluid. Again, inertial waves, gravity waves or a combination of the two can arise. Gravity waves can only arise if the gravity force applied on the fluid is not uniform in space. In a homogeneous fluid, the gravity force acts with the same strength on each parcel. Density differences change this and allow gravity waves to arise.

1.1.1 Internal gravity waves

As mentioned before, two types of internal gravity waves can be distinguished. The first type is the interfacial internal waves, these are waves propagating along isopycnals. They have the same features as surface waves, but the effective gravitational forcing is now reduced. The other type is internal gravity waves in a continuously stratified fluid. They have features which differ from surface waves, for example the group velocity is perpendicular to the phase velocity and the dispersion relation is a function of the angle of propagation only, this in contrast to surface waves, where the dispersion relation is a function of the wave vector length. The angle of propagation is determined by the stratification and the frequency of the waves. Internal waves can be described in terms of modes. This means they are studied as standing vertical waves. This description becomes problematic with variations in depth. The other description is in terms of rays. These rays are parallel to the lines of equal phase (see for example Turner 1973).

1.1.2 Inertial waves

Inertial waves are supported in a uniformly rotating, homogeneous fluid. If this fluid is unperturbed, the centrifugal forces are in balance with the pressure gradient force. The centrifugal force is directed radially outwards and the pressure gradient force is directed radially inwards. If a parcel, maintaining its initial angular momentum, is displaced, radially inwards (outwards) the centrifugal force is stronger (weaker) than the pressure gradient force and the parcel is driven backwards to its original radial position. If a sloping wall (i.e. not perpendicular or parallel to the axis of rotation) is present, the horizontally propagating wave is forced upwards and downwards. This will generate internal waves. Like internal gravity waves, inertial waves have a dispersion relation which relates the frequency with the wave vector direction and have a group velocity perpendicular to the phase velocity.

1.1.3 History

One of the first written accounts of internal waves is by Benjamin Franklin in 1762. He observed an oil lamp, containing water and approximately the same amount of oil on top of this. The movements of the ship made the water move wildly while the surface of the oil moved quietly. Later, after arriving in America, Franklin experimented with the same set up. The interfacial

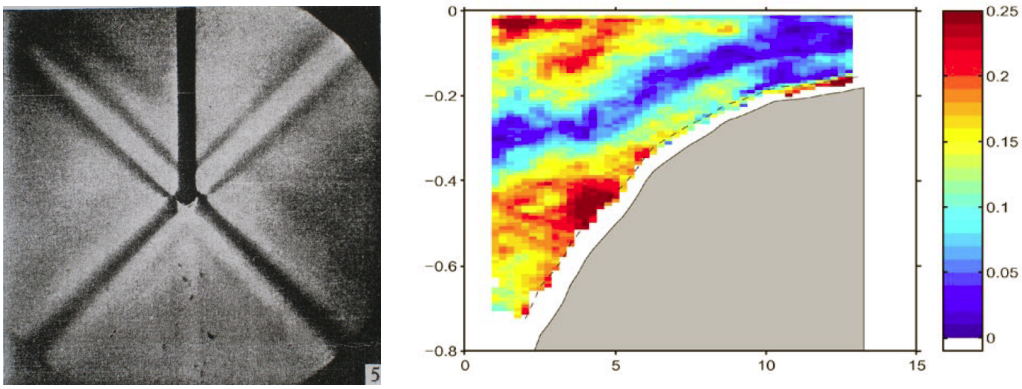

(a) (b)

Figure 1.1: (a) Side view (vertical is in the gravitational direction) of internal waves generated by an oscillating a cylinder in the middle of the tank. A shadowgraph technique is used, darker and lighter regions indicate perturbations in the density. The group velocity is directed along the lines of equal phase. From Mowbray & Rarity (1967)). (b) Amplitude of the baroclinic cross-slope velocity (m/s), obtained with harmonic analysis of ADCP-measurements in the Bay of Biscay. From Gerkema *et al.* (2004).

waves in a two-layer system were later suggested by V. Bjerknes in 1898 as an explanation for "dead-water". The phenomenon of "dead-water" has been known among sailors for centuries. A ship is in "dead-water" if it is unable to maintain its velocity which you would expect from the forcing (wind, rowing). Bjerkness suggested that, if a layer of fresh water is on top of salt water, a part of the forcing, meant to sail, is converted to internal waves, propagating along the interface between the fresh and the salt water. Ekman corroborated this theory with experiments (Gill 1981).

Mowbray & Rarity (1967) performed experiments on internal waves in a continuously stratified fluid, using the Toepler-schlieren method. They confirmed the theoretical prediction that the group velocity is perpendicular to the phase velocity and that the angle of propagation depends on the forcing frequency and the stratification. A shadowgraph image of the experiment is shown in Fig. 1.1(a). Internal waves have been observed in the oceans. Internal waves arise when a barotropic tide is forced over topography (see for example Baines 1973; Bell 1975; Rattray 1960). In the Bay of Biscay the generation of internal wave is relatively strong. Gerkema *et al.* (2004) report observations of the spatial structure of internal waves, the structure of the observed waves can be understood from the description in terms of rays. The observed structure, shown in Fig. 1.1(b), corresponds well with theoretical expectations.

1.1.4 Role in oceanography

Internal waves are relevant in oceanography. Internal waves produce a strong spatial structure in the distribution of velocity and thus create localised regions with mixing. This creates a spatial distribution of nutrients and sediments. Internal waves can be observed from space, around the areas of generation, see Fig. 1.2. Furthermore internal waves are expected to supply a part of the energy required to maintain the Meridional Overturning Circulation (MOC) (Munk & Wunsch 1998). Internal waves in the ocean are generated in regions with changing bottom topography and

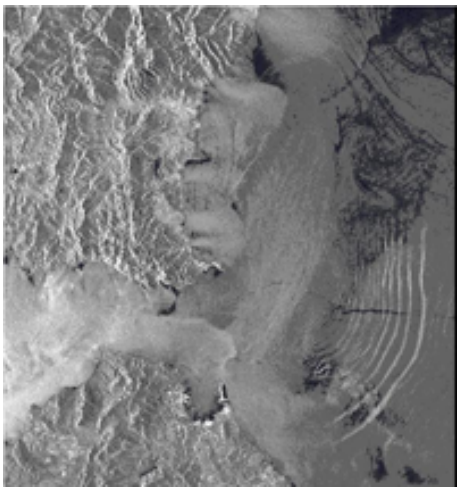

Figure 1.2: Internal waves observed with a satellite, emerging from the Strait of Gibraltar (Spain in the lower part, Morocco in the upper part of the image). Mediterranean water is relatively salt, flowing into the Atlantic Ocean, on top of this a less saline layer of Atlantic Water, flowing into the Mediterranean Sea. Internal waves are generated at a step in depth around the Strait of Gibraltar, they propagate on the interface between the two layers. The dynamics of the internal waves cause convergence and divergence of the flow at the sea surface, this organises the slick material at the surface in lines parallel to the phase lines of the internal waves. This effect makes internal waves visible from space. This is an ERS-1 SAR-image, ESA.

a barotropic (tidal) forcing. A part of the barotropic forcing is converted to a baroclinic signal at the topography change. This baroclinic signal appears as an internal wave. If the group velocity is directed to the bottom, kinetic energy is transported to the deeper parts of the ocean and wave breaking eventually leads to mixing. This mixing in the deeper ocean supplies energy to the MOC. Mixing by internal waves is still investigated, this research is embedded in the Long-term Ocean Climate Observations (LOCO) program in which the NIOZ, IMAU and KNMI take part (LOCO-proposal, 2002)).
At which scales internal wave energy dissipates by viscous damping is one of the topics studied with the experiments performed in Cambridge. The observed relations might contribute to the discussion about the amount of internal wave energy dissipating at certain wavelengths.

1.2 Internal wave attractors

Internal waves preserve their angle with the vertical (axis of rotation or gravitational direction) upon reflection and focus or defocus when they reflect on a sloping wall, see Fig. 1.3. Focusing leads to smaller wavelengths and focusing of the wave energy (compare this with surface wave, which preserve their wavelength upon reflection). In a confined geometry with at least one sloping wall, focusing dominates over defocusing (Maas & Lam 1995). In certain geometries, the internal waves are focused and during the series of reflections are attracted to a certain path (as shown in Fig. 1.4). This closed orbit is called an internal wave attractor. Since the wavelength decreases if they are focused, shear is expected to be relatively large around the attractor, and energy travels

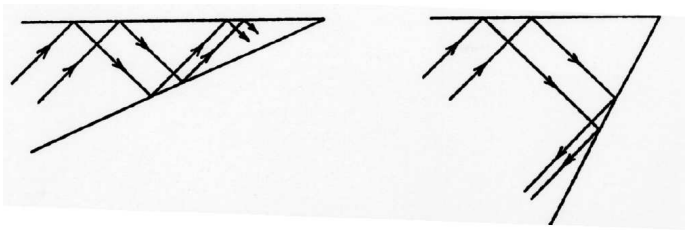

Figure 1.3: Example of a sub-critical reflection (left) and a supercritical reflection (right). Reflection at a horizontal or vertical boundary does not result in (de)focusing. Inverting the direction of the rays results in defocusing. From Turner (1973).

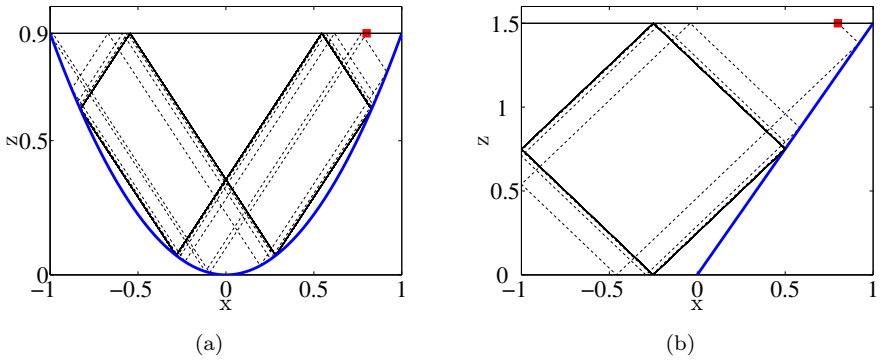

Figure 1.4: Rays, starting at the surface (red square) converging to an attractor in a (a) parabolic basin and (b) a rectangular tank with one sloping wall. x- and z-axis indicate arbitrary units.

along the closed path of the attractor. An attractor can be interpreted as a trapped mode, but will not appear for a discrete number of separated frequencies, like trapped surface modes, but arise within a certain range of frequencies, depending on the geometry.

1.2.1 History

Stewartson (1971) mathematically studied trapped modes in a rotating fluid. These trapped modes did not exist for a discrete number of frequencies (like for example trapped Poincaré surface waves), but for an infinite number of frequencies, within a certain range, depending on the geometry. The rays, starting within a certain interval, converge to a closed path, where the pressure and velocity fields develop singularities after an infinite amount of reflections.
Maas & Lam (1995) theoretically studied the focusing of internal gravity waves in confined two dimensional basins (with an ideal inviscid fluid). Several shapes were explored. They found that, globally, focusing dominates over defocusing and the internal waves are attracted to certain limit cycles. These limit cycles are attractors, which refers to the terminology used in dynamical systems. The existence and the structure of the attractors were studied as they varied the parameters of the geometry. The period of the attractor was studied, i.e. the number of reflections of an internal wave ray on an attractor before it returns to its initial position on the attractor. Low period

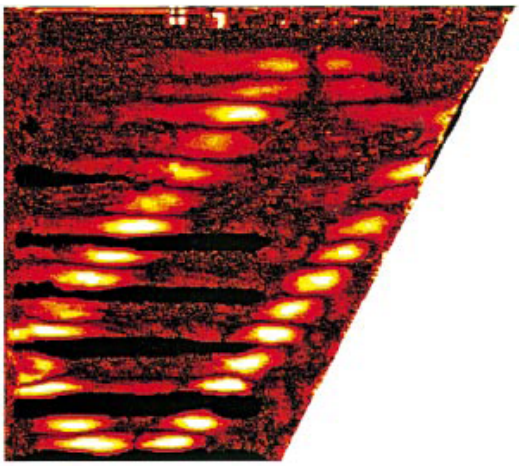

Figure 1.5: Figure of the difference between the maximal displacement of the dye-lines at the steady-state and the initial horizontal position. The displacement is clearly located around a rectangular loop. Figure taken from Maas *et al.* (1997).

attractors can change into high period attractors as the parameters of the geometries are varied. The convergence of internal wave rays towards the attractors reveals a fractal-like nature in the parameter space of the geometry.
Maas *et al.* (1997) found experimental evidence of an internal (gravity) wave attractor, in a square tank with one sloping wall. The internal waves were excited by parametric instability, by vertically oscillating the tank, and visualised with dye-lines. After about 300 periods of oscillation a steady state was reached and wave motions were localised around a closed, square path in the tank, the attractor. The phase propagation was revealed to be perpendicular to the attractor, from which one can conclude that the energy propagation takes place along the attractor. See Fig. 1.5.

1.2.2 Role in oceanography

Internal wave attractors imply areas with large shear since the wavelength decreases upon each reflection while the amplitude of the velocity increases. This implies that attractors define areas with relatively strong dissipation and mixing. Internal wave attractors determine the spatial distribution of energy. They might appear in a half open domain, where barotropic tides generate a baroclinic signal on a continental slope, as modelled by Drijfhout & Maas (2007). Internal wave attractors are also expected in stratified lakes, since they are a closed basin. Measurements which indicate this were performed by Antenucci *et al.* (2002). Attractors localise kinetic energy and this influences the distribution of sediments at the bottom. Measurements which suggest this were found by Fricker & Nepf (2000). Since strong shear is anticipated in an internal wave attractor, experimenting with attractors gives an opportunity to study the wavelengths at which dissipation overcomes the generation of shorter wavelengths. In other words, dissipation of kinetic energy in water can be studied in more detail. In our experiments, relations were found between the shape of an attractor and the scales at which dissipation by viscous damping becomes dominant.

1.3 Topics in this thesis

One of the aims of the experiments performed in November and December 2006, was to get used to synthetic schlieren and optimise the experimental set-up. Eventually, an experimental set-up has to be designed to study internal wave attractors in 3D. However, since visualisation of internal waves in a flat (semi-2D) tank is more straightforward, we started with experimenting on internal waves in a semi-2D tank with one sloping wall. We performed some experiments with larger (3D) tanks, a parabolic channel and a rectangular tank with one slope. The experiments with the semi-2D tank provided very good data about internal wave attractors. We varied the strength of the forcing, oscillation period (which influences the shape of an attractor) and stratification and studied the influence of a rigid lid. The experiments offered new information about the temporal evolution of the attractors and the typical scales associated with them. Waves have been generated by oscillating the tank vertically, which might invoke parametric instability, resulting in the excitation of internal waves at subharmonic frequencies, i.e. half (or multiples thereof) the forcing frequency. But the vertical oscillation generates waves at the harmonic frequency as well, by small horizontal movements, accompanying the oscillation; a barotropic movement is forced over the slope, where internal waves are generated. This mechanism appeared to be responsible for the generation of internal waves in the bulk of the experiments.
The experimental set-up is presented in chapter 3 and the results in chapter 4. These results are analysed further in chapter 5. At the end of these chapters, suggestions and adjustments regarding the experimental set-up are given.
In the next chapter I will give an overview of the theory about internal wave attractors.

CHAPTER 2

Theory

In this chapter I will only discuss internal gravity waves in a continuously stratified fluid, since these were studied during the experiments. Internal gravity waves are introduced in section 2.1, internal wave attractors in section 2.2. The theory is based on Maas & Lam (1995); Maas (2005); Lam & Maas (2007) .

2.1 Internal gravity waves in a continuously stratified 2D fluid

In a two-dimensional incompressible fluid, conservation of mass results in:

$$\frac{\partial u}{\partial x} + \frac{\partial w}{\partial z} = 0, \tag{2.1}$$

where u and w are the horizontal (x) and vertical (z) velocity components, respectively. The z-axis is chosen anti-parallel to the gravitational direction. Equation (2.1) allows the introduction of the stream function ψ:

$$(u, w) = \left(-\frac{\partial \psi}{\partial z}, \frac{\partial \psi}{\partial x}\right)$$

The Boussinesq approximation is used, so density differences are ignored in the momentum equations, except where heavy mass is considered. The density can be written as: $\rho = \rho_0 + \rho^*(z) + \rho'(x, z, t)$, where $\rho_0 \gg \rho* \gg \rho'$. The fluid is assumed to be non-rotating and inviscid. Since ρ' is small the momentum equations can be linearised; non-linear terms become very small, since they are products of two small quantities. For a non-rotating and inviscid fluid the linearised momentum equations and the conservation of density can be written as:

$$\frac{1}{\rho_0}\frac{\partial p}{\partial x} = \frac{\partial^2 \psi}{\partial t \partial z} \tag{2.2}$$

$$\frac{1}{\rho_0}\frac{\partial p}{\partial z} = -\frac{\partial^2 \psi}{\partial x \partial t} - \frac{\rho'}{\rho_0} g \tag{2.3}$$

$$\frac{g}{\rho_0}\frac{\partial \rho'}{\partial t} = N^2 \frac{\partial \psi}{\partial x}, \tag{2.4}$$

where p is the perturbation pressure, which is the total pressure minus the hydrostatic pressure, and

$$N^2 = -\frac{g}{\rho_0}\frac{\partial \rho^*}{\partial z}$$

is known as the buoyancy frequency or Brunt-Väisälä frequency. This parameter is an indication for the stability of a stratified fluid. The equations (2.1), (2.2), (2.3) and (2.4) now govern the system. If we take the z-derivative of (2.2) and the x-derivative of (2.3) and combine the results, we obtain:

$$\frac{\partial^3 \psi}{\partial t \partial z^2} + \frac{\partial^3 \psi}{\partial x^2 \partial t} + \frac{g}{\rho_0}\frac{\partial \rho'}{\partial x} = 0 \tag{2.5}$$

Combining the time-derivative of (2.5) and the x-derivative of (2.4) results in:

$$-\frac{\partial^2}{\partial t^2}\Big(\frac{\partial^2}{\partial x^2} + \frac{\partial^2}{\partial z^2}\Big)\psi - N^2\frac{\partial^2 \psi}{\partial x^2} = 0 \tag{2.6}$$

Assuming monochromatic wave solutions of the form:

$$\psi(x, z, t) = \psi_0(x, z)e^{-i(\omega t)},$$

where ω is the frequency, A the amplitude and k and m the horizontal and vertical wave numbers, respectively, and substituting this in (2.6) a hyperbolic PDE (Partial Differential Equation) is obtained:

$$\frac{\partial^2 \psi_0}{\partial z^2} - \frac{N^2 - \omega^2}{\omega^2}\frac{\partial^2 \psi_0}{\partial x^2} = 0 \tag{2.7}$$

which, for $\omega^2 < N^2$, is a wave equation, without an independent time variable. From (2.7) and by assuming plane wave solutions of the form: $\psi_0(x, z) = Ae^{i(kx+mz)}$, the following dispersion relation is obtained :

$$\omega^2 = N^2\frac{k^2}{\kappa^2} = N^2\cos^2\alpha \tag{2.8}$$

Here α represents the angle of the wave number vector ($\mathbf{k} = (k, m)$) with the horizontal and κ the wave number: $\kappa^2 = k^2 + m^2$. From the dispersion relation, (2.8), expressions for the group velocity $\mathbf{c}_g$ and the phase velocity $\mathbf{c}$ are found:

$$\begin{aligned} \mathbf{c}_g &= \Big(\frac{\partial \omega}{\partial k}, \frac{\partial \omega}{\partial m}\Big) = \frac{mN}{\kappa^3}(m, -k) \\ \mathbf{c} &= \Big(\frac{\omega k}{\kappa^2}, \frac{m\omega}{\kappa^2}\Big) = \frac{kN^2}{\kappa^2}(k, m) \end{aligned}$$

Note that $\mathbf{c}_g \cdot \mathbf{c} = 0$, which means that the group velocity is perpendicular to the phase velocity. The expressions above also show that when the group velocity has an upward (downward) component, the phase velocity has a downward (upward) propagating component. Internal waves in a

continuously stratified fluid thus have a clearly distinct dispersive behaviour from surface waves. For surface waves the frequency is dependent on the *length* of the wavenumber vector, while for internal waves the frequency depends on the *direction* of the wave number vector. Furthermore, the wave equation, obtained in (2.7), depends on spatial variables only. The wave equation describing surface waves includes a independent variable for time, which makes it convenient to solve it as a initial value problem. In case of internal waves in a confined geometry, (2.7) is solved as a boundary value problem.

2.2 Internal wave attractors in 2D

From the dispersion relation (2.8) and the fact that the frequency is not altered by reflection, follow that an internal wave preserves its angle with the vertical upon reflection, and thus does not obey Snell's law. Fig. 1.3 shows that a wave can be focused or defocused upon reflection on a wall which is neither vertical nor horizontal (with respect to the gravitational direction). As mentioned in section 1.2.1, Stewartson (1971), described trapped modes of inertial waves in a confined geometry. These trapped modes do not exist for a discrete number of frequencies, or eigenmodes, but within a continuous frequency domain. If in these confined areas focusing dominates over defocusing and a trapped mode exists, a singularity develops after an infinite number of reflections. This singularity is called an internal wave attractor. This also applies to internal gravity waves. A ray, starting at an arbitrary point, will reflect in such a way, that it will approach the attractor as it progresses along the trapped mode (see Fig. 1.4). In this section I will briefly summarise some features of internal wave attractors in a parabolic and a trapezoidal basin.

2.2.1 Characteristics, webs and fundamental intervals

Equation (2.7) can be rewritten in non-dimensionalised form:

$$\frac{\partial^2 \Psi}{\partial Z^2} - \frac{\partial^2 \Psi}{\partial X^2} = 0 \tag{2.9}$$

where $X = x/L$, L is the half-width of a basin, and the vertical is stretched: $Z = z/D$. D is defined as:

$$D = \frac{\omega L}{\sqrt{N^2 - \omega^2}}$$

Since equation (2.9) consists of spatial coordinates only, it is logical to solve this equation as a boundary value problem, considering a closed domain. Using the Dirichlet boundary conditions, where the value of a function is specified on the boundaries (i.e. the walls of the basin), impermeability requires a vanishing stream function at the boundaries: $\Psi_b = 0$. This means, no forcing is assumed on these boundaries. For a hyperbolic equation, a vanishing function at the boundaries does not result in a trivial solution only. But in order to define a well-posed problem, certain steps have to be followed.
First of all, we approach the problem with the method of *characteristics*. Characteristics are lines

on which a PDE has the same solution, or a line on which a PDE degenerates to an ODE (see for example Arfken 1995). This is also used as an approximate method in geometric optics, but in the case of internal waves it is exact. This can be understood by the fact that in geometric optics, the characteristics are perpendicular to the lines of equal phase, but in the case of internal waves they are parallel (to the lines of equal phase or $\mathbf{c}_g$). The method of characteristics is used in Fig. 1.4 in the Introduction. In the stretched coordinates, non-dimensional, description, internal waves and characteristics will have an angle of 45° with the vertical. Characteristics can be used to find solutions in a confined geometry. These are found by constructing a 'web' of characteristics. Fig. 1.4(a) and 1.4(b) show the web of the characteristic starting at the point indicated by the red triangle. This is seen if we express Ψ in (2.9) as:

$$\Psi(X, Z) = f(X + Z) - g(X - Z) \tag{2.10}$$

in which f and g are arbitrary functions. Fig. 2.1 shows how Ψ is composed from f and g, the thick solid line indicates a wall. The down-sloping function f intersects with the wall. This point defines the position of the upward sloping function g. Since Ψ_b (Ψ at the boundary) must vanish, f must be equal to g at the boundary. And since this must be true for any intersection at the boundary, f is invariant anywhere on the web. The intersection of g with a wall will be the new starting point for another characteristic, by repeating this, a web is created (i.e. a web is created by iteration). A constructed web is not the same as a wave propagating along it, but it is the path along which an internal wave signal could propagate. If the pressure field, Π is non-dimensionalised, $\Pi = (L/D)P$, from the momentum equations it can be deduced that the pressure field and the stream function are *hyperbolically conjugate*:

$$\begin{aligned} \frac{\partial \Psi}{\partial Z} &= \frac{\partial P}{\partial X} \\ \frac{\partial \Psi}{\partial Z} &= \frac{\partial P}{\partial Z} \end{aligned}$$

so the pressure field can be described as the sum of g and f:

$$P(X, Z) = f(X + Z) + g(X - Z), \tag{2.11}$$

that is why f and g are also referred to as partial pressure. By setting a pressure at the point of the red squares in Fig. 1.4(a) of 1.4(b) at the surface, the partial pressure is known on the entire web, so on the black lines in Fig. 1.4.

One can construct a solution by defining the pressure over a part of the boundary, and thus defining the partial pressure on the webs emerging from this domain, the pressure within the fluid is determined by the sum of two crossing characteristics. This is called dressing the web. The problem might become overdetermined if the pressure is specified over a too large interval. If, for example, a characteristic reflects at the surface where a pressure is already specified, two pressures appear on one point. An interval has to be chosen in order to have a well-posed problem, preventing that characteristic reflect at the surface where the pressure is already specified. This interval is named the fundamental interval. For a parabolic channel one fundamental interval is determined by the critical points. These are the points where the bottom slope is equal to one of the characteristics. The other fundamental interval is determined by one of the two points where

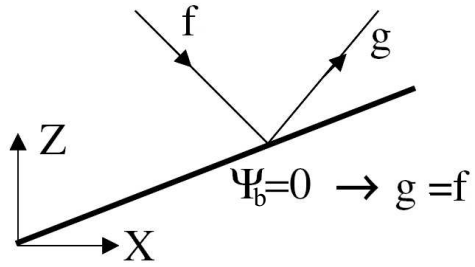

Figure 2.1: The invariant functions f and g. From Maas (2005)

a characteristic emerging from the other corner reaches the surface. In the trapezoidal basin also two fundamental intervals are present. One is between $x = 1$ and the x-position on the surface from which a characteristic reaches the left corner of the bottom and the other is between $x = -1$ and the position from which a characteristic reaches, via reflection on the wall, the point where the bottom and the slope coincide. The fundamentals intervals are coloured red in Fig. 2.2.

Defining the pressure over the whole surface.

The restriction of defining a pressure at the fundamentals interval only, can be loosened, as shown by Lam & Maas (2007). They showed that a pressure can indeed be specified over the whole surface, which is physically natural to do. The method is as follows: A pressure is defined over the whole surface. From the surface, characteristics are initiated and, by iteration, webs are created. A characteristics has a partial pressure equal to the pressure at the point of the surface from which it originated. Each time a characteristic reflects at the surface, the defined surface pressure at the point of reflection is not applied to the web anymore. So the surface pressure is only applied to a characteristic initiated there, but not to characteristics reflecting at the surface. This only applies for small perturbations. Furthermore, Lam and Maas assumed that work is done at a point only by the prescribed pressure at that point. So a surface pressure, a small sloshing at the surface, is not influenced by the reflection of internal waves at the surface. The stream function is a superposition of all the crossing characteristics, the stream function thus depends on the number of iterations, i. This last statement is not true in the analytical sense, since the analytical solution of Ψ is approximated as $i \to \infty$. However, in viscous fluids, viscosity damps the contribution as the number of reflections increase.

2.2.2 A parabolic basin

Using the depth (from the surface to the deepest point), H, and the half-width, L, of a parabolic basin, τ is defined as:

$$\tau = \frac{H}{L}\frac{\sqrt{N^2 - \omega^2}}{\omega}, \tag{2.12}$$

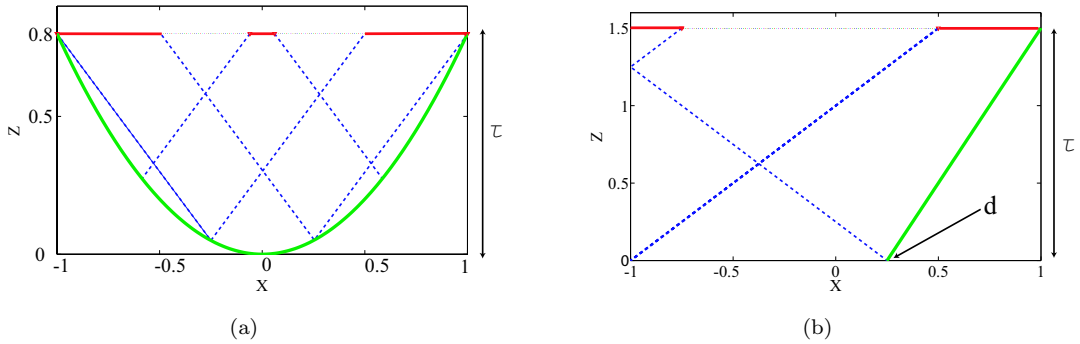

(a) (b)

Figure 2.2: Fundamental intervals (red) for (a) a parabolic basin ($\tau = 0.8$) and (b) a rectangular basin with one sloping wall ($\tau = 1.5$, $d = 0.25$). The blue dotted lines are characteristics emerging from (a) the two critical points and the two corners at the surface and (b) the two corners at the bottom. In (a) only one of the outer intervals must be used.

and the walls of a parabolic basin can be expressed (non-dimensional) as $Z = \tau(1-X^2)$. Note that τ includes both the ratio of N and the frequency of the internal waves and a ratio of the depth and the half-width. This means that different wave frequencies in different parabolic geometries can support an attractor with the same shape, as long as τ is constant. The shape of the attractor depends on τ. The attractor in Fig. 1.4(b) is a limit cycle which reflects at the surface twice, but for other values τ, attractors consist of more surface reflections. The structure can be studied by iteration, as shown in Fig. 2.3. A characteristic is initiated at the surface at x_0 and from this a web is created in the basin by iteration. The sum of all x-coordinates of the reflections of the web at the surface is calculated for 199 iterations for a web initiated at x_0. The total value is indicated by the colour. The structure of the plot reveals, moving along the x_0-axis, the x-positions where the attractor reflects at the surface. This can be seen in Fig. 2.3(b) where the x-position of the reflection at the surface is plotted for high number of iterations only (between 900 and 1100). These points are approximately the x-positions of the attractor reflecting at the surface. Regions of τ where the x-position gradually changes and regions where the periodicity rapidly changes can be separated. The periodicity is the number of reflections in an attractor; Fig. 1.4(a) shows a (2,1)-attractor, two reflections at the surface and one on each sidewall. It is clear that continuous regions of τ exist.
The stream function, or the pressure field, can be obtained by dressing the web. The obtained stream function, by setting a pressure in the fundamental intervals, is shown in Fig. 2.5.

2.2.3 A trapezoidal basin

This geometry was used in the majority of the experiments. The parabolic basin can be described with one non-dimensional parameter, τ. But for the rectangular tank with one sloping wall, two parameters are required, τ (as defined in equation 2.12) and d, which is the X-coordinate where the slope intersects with the bottom, as indicated in Fig. 2.2(b). From the fundamental intervals characteristics are launched, to construct webs. A value for the pressure can be specified on the fundamental intervals to construct a pressure field, and from this the stream function.

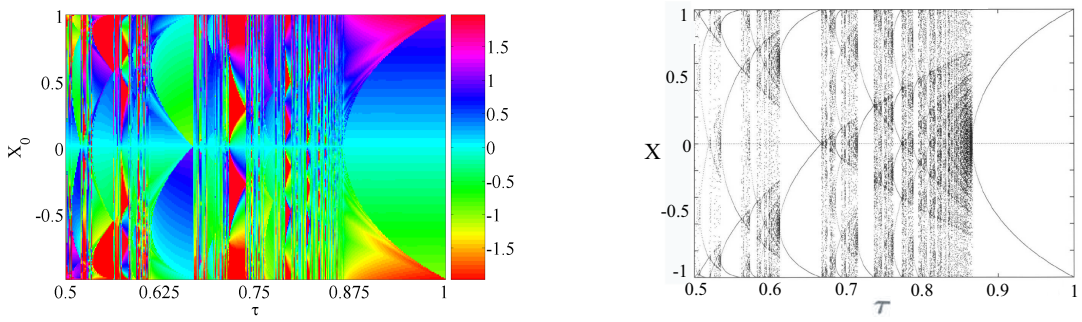

(a) (b)

Figure 2.3: (a) Sum of the x-positions of a characteristic starting at x_0 for 200 iterates and (b) the x-position for a characteristic at the surface from 900 to 1100 iterations, thus approximately indicating the x-position of an attractor reflecting at the surface. From Maas & Lam (1995)

In Fig. 2.3 the structure of an attractor is indicated in a τ-x_0-diagram. The positions where the attractor reflects at the surface are shown in Fig. 2.3(b). But for a rectangular tank with one sloping wall two parameters determine the character of an attractor, τ and d, and another way of presenting the occurrence of attractors is chosen. This is by plotting the Lyapunov-exponent in a τ-d-diagram. The Lyapunov-exponent indicates the strength of convergence towards an attractor. So if an attractor has a surface reflection at x_a, it will indicate how fast a characteristic initiated at $x_a + \Delta x$ converges to x_a. When the convergence is strong, this indicates a low periodic (low number of reflections) attractor. The Lyapunov exponent can numerically be calculated as:

$$\lambda = \frac{1}{N} \frac{x_N - x_a}{\Delta x} \tag{2.13}$$

Here N is the number of iterations and x_N the x-position of the characteristic crossing the surface after N iterations. A small value of λ indicates strong convergence. This is shown in Fig. 2.4, the white (darker) areas indicate strong (weaker) convergence. Below the line $\tau = 1 - d$, no limit cycles exist. In these areas, point attractors are expected, the webs are attracted toward the corner where the slope touches the surface. The periodicity of the attractors in the white areas are indicated in the plot; (1,1) means one reflection at the surface and one on each sidewall. In section 4.2, Fig. 4.1, the experiments which were performed in the trapezoidal tank, thus their value of d and τ, are indicated in the same figure.
Maas *et al.* (1997), performed experiments in a trapezoidal basin and found an attractor. A result is shown in Fig. 1.5. The energy propagated clockwise. This can be understood by the following: Internal waves propagating counterclockwise defocus upon reflection on the sloping wall, and will thus vanish after a few reflections.

2.3 Attractors in 3D

Until now, only attractors in a 2D system have been discussed. The goal of the IW3D project is to gain more knowledge about internal wave attractors in 3D, both experimentally and mathematically. The majority of the experiments discussed in this thesis were performed with a narrow,

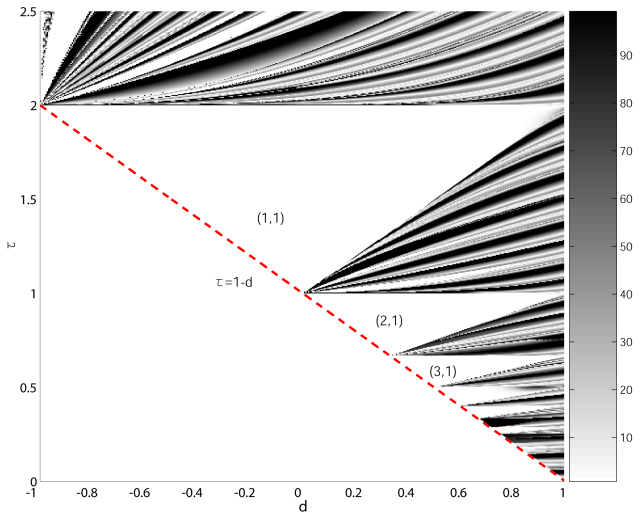

Figure 2.4: Convergence rate, λ, numerically obtained, of webs, initiated from two neighbouring points, x_a and $x_a + \Delta x$. This figure contains some small numerical errors, which are not important within the scope of this thesis. For more detailed and accurate plots, see Maas *et al.* (1997); Swart (2007).

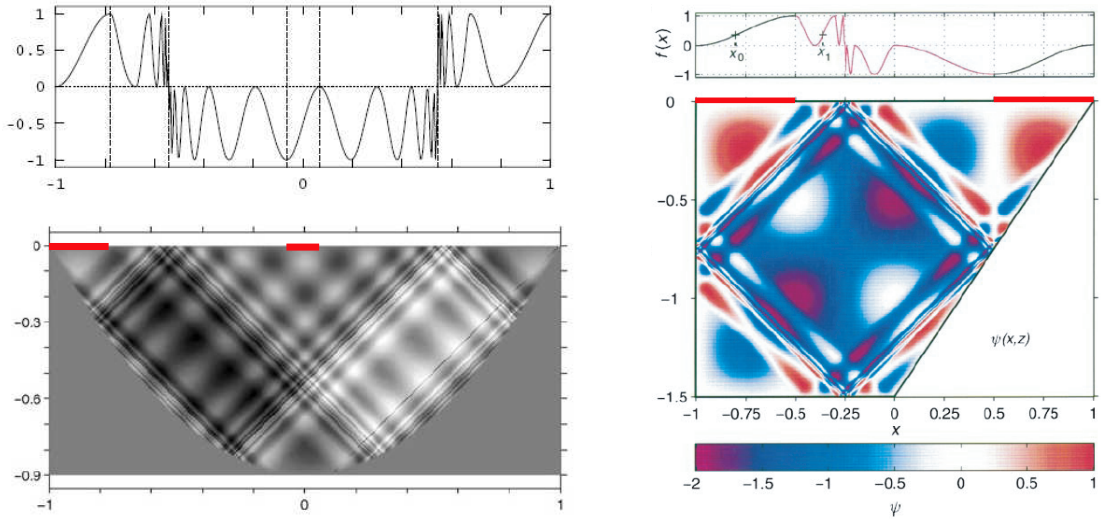

(a) (b)

Figure 2.5: Stream function in (a) a parabolic basin and (b) a rectangular basin with one sloping wall, obtained with the method of characteristics, a partial pressure is defined over the fundamental intervals bounded by the dashed lines and indicated by the red lines. The resulting pressure at the surface is also indicated. It can be seen that the pressure changes rapidly as one moves near the attractors. From (a) Maas (2005) and (b) Maas *et al.* (1997).

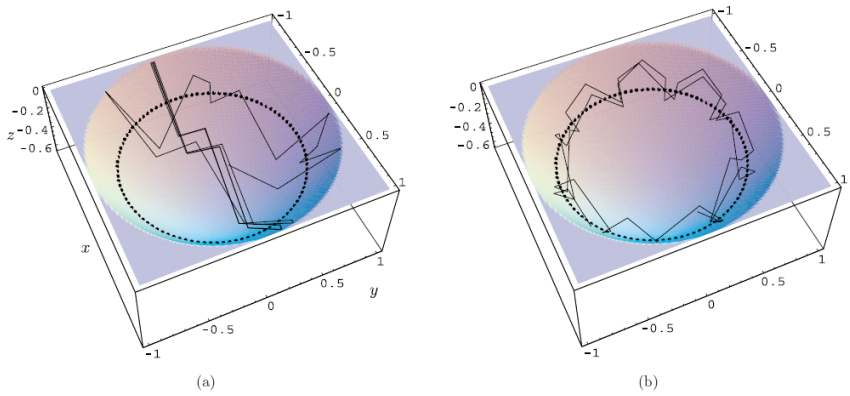

Figure 2.6: Internal wave 'rays' in a paraboloidal basin with (non-dimensional) depth $\tau = 0.65$. Rays emerge from two different points, x_0. One converges to a planar limit cycle (a) and one cycles around the critical line (b). From Maas (2005).

semi-2D tank, but one of the goals is to experiment with geometries with a 3D character. We performed experiments in more extended (3D) tanks, a parabolic channel and a rectangular tank with one sloping wall. These are discussed in sections 4.3, 4.4, 5.2 and 5.3.
Analytical solutions in a 3D geometry are more difficult to obtain. In the previous section, characteristics were used. But now a characteristic is no longer a line, but a cone with a fixed angle, determined by the dispersion relation. The pressure is an integral over this cone instead of the sum of two partial pressures. But if wave beams are assumed and we neglect diffraction upon reflection, some insight can be gained about internal waves in a confined 3D geometry. We assume a beam to propagates along a line.
If a beam reflects at the bottom, the angle with the vertical is preserved (according to the dispersion relation), but the horizontal direction is altered, depending on the slope of the bottom. Again, sub-critical and supercritical reflections can occur. A paraboloidal basin as shown in Fig. 2.6, contains a supercritical slope (upper part) and a sub-critical slope (near the bottom). These areas are separated by the critical line, where the vertical gradient is equal to the angle of propagation of the beam. This is indicated by a dotted line in Fig. 2.6. If a ray is introduced at x_0 at the surface, we see that the beam can converge to a plane (Fig. 2.6a), where it gets trapped in a limit cycle, similar to an attractor in the 2D parabolic basin. Another possibility is that it focuses and defocuses around the critical line (Fig. 2.6b). These waves are called internal edge waves. The occurrence of these two situations depend on depth τ and starting point x_0.
Internal edge waves only appear if a critical line exists, so a supercritical and a sub-critical slope. Observations by Horn & Meincke (1976); Huthnance (1982); Lerczak *et al.* (2003) at the foot of a continental slope suggest their existence.

2.4 Experimental topics related to the theory

- Consider Fig. 2.4. In this plot the white areas indicate the existence of a strong attractor (in the inviscid case) and the darker areas where the convergence, thus the attractor, is

weaker. The different white areas represent attractors with different shapes. As indicated in the figure, the largest white area represents a (1,1)-attractor. The area below that a (2,1)-attractor, which is longer (assuming the same dimensions of the basin). We compared the different attractor shapes by varying the period of oscillation, in the same tank with the same stratification. Viscosity acts on the waves along the attractor, so on longer attractors, the damping by viscosity during one cycle will increase. It appeared that the shape of the attractors could be described by the inviscid description. But the (2,1)-attractor (longer and more reflections) was found to have weaker amplitudes than the (1,1)-attractors. We performed experiments with a τ and d in the dark areas of Fig. 2.4 but no baroclinic response was observed during these experiments. The results and analysis of this are presented in section 4.2.2 and 5.1.3, respectively.

- Fig. 2.5 reveals that around the attractor the gradients in Ψ or in the pressure field are large. These areas are associated with stronger shear. It is interesting to observe what happens in nature on these small scales, where mixing and non-linear effects are expected (and viscosity cannot be ignored). We varied the amplitude of the forcing and the shape of the attractor (see previous point) and analysed the wave number spectra. The strongest wave numbers of the attractors are an indication for the scale at which viscosity becomes dominant. The experiments showed that the shape of the wave number spectrum did not depend on the amplitude of the forcing, but it does depend on the attractor length. This is discussed in section 5.1.

- The wave equation, (2.9) is solved as a boundary value problem (though iteration might be interpreted as an evolution in time), but how does an attractor evolve in time? The build up of an attractor and its decay, after the forcing is ceased, were studied. During the build up, the wave number increased, until at a certain wave number a steady state was reached (see the previous point). During the decay, the dominant wave number increased further. The evolution of the wave number spectrum appeared to depend on the length of the attractor (section 5.1). We did not observe an indefinite increase in wave number (as around the singularities in the inviscid description). This is explained by the fact that while the wave number spectrum evolves from longer to shorter waves during the build up, it saturates because shorter waves travel slower and give viscosity time to annihilate them.

- Lam & Maas (2007) studied an attractor model, forced by a surface sloshing. Can a sloshing surface mode generate internal wave attractors? We found that if a rigid lid was placed on the surface, the strength of the internal wave attractor diminished dramatically (section 4.2.3). So, a free surface was in our set-up important in the generation of internal waves. An analysis of this result is given in 5.1.5.

- How do attractors reveal themselves in 3D? Drijfhout & Maas (2007) modelled a half open parabolic channel with a slope, where an attractor, trapped in a plane was found. We compared this result with an experiment in the parabolic channel. We observed an attractor as well, which showed similarities with the result of Drijfhout & Maas.

CHAPTER 3

Experimental set-up

In the framework of IW3D we applied the synthetic schlieren technique to study internal wave attractors. The experiments were performed in the GK Batchelor Laboratory at the Department of Applied Mathematics and Theoretical Physics (DAMTP) of the University of Cambridge, in November and December 2006. The final goal of the experiments for IW3D is to observe wave attractors in tanks which are extensive in 3D. However, the major part of the reported series of experiments, were performed with a narrow (semi-2D) trapezoidal tank (one sloping wall) which resulted in interesting observations and knowledge about the experimental method. In this chapter I will introduce the synthetic schlieren technique (section 3.3), methods to create a stratification in a tank (3.4), generation of internal waves (3.2) and the experimental set-up (Fig. 3.4). In the next chapter, the parameters, experimental conditions and results are presented.

3.1 The GK Batchelor Lab

The experiments were performed in the GK Batchelor Laboratory of the University of Cambridge. It is named after George Keith Batchelor (1920-2000), an influential fluid mechanic researcher. He is the author of the standard work *Introduction to fluid mechanics* and involved in the founding of DAMTP in 1959 and the laboratory at this department. His idea was that theoreticians should be able to design and/or perform experiments on fundamental features of fluids, which is the reason it is part of the DAMTP. In 2002 the department and the lab were moved from Silverstreet to the new Centre for Mathematical Sciences (CMS) at Wilberforce road, together with the Department of Pure Mathematics & Mathematical Statistics and the Isaac Newton Institute. The lab at CMS is now named the GK Batchelor Laboratory. Stuart Dalziel, current director of the lab, was involved in the design of the new laboratory. The present laboratory is constructed to enable very precise and modern experimental techniques, e.g. synthetic schlieren and particle image velocimetry (PIV). Present research involves internal waves, rotating fluids, turbulence in homogeneous and stratified fluids and also avalanches. Furthermore, there is a lot of technical expertise available. We used Digiflow to collect and analyse our data. This program is designed by Stuart Dalziel, and, since every experiment has its own technical demands, it was of pivotal importance that he was available to apply the required adjustments to the program.

3.2 Generation of internal waves

3.2.1 Parametric Instability

The internal waves described in Maas *et al.* (1997) were generated by parametric instability. Instability refers to the exponential growth of a perturbation. The principle of parametric instability can be understood by considering a driven pendulum, with length l. The pendulum is driven by a vertically oscillating pivot, oscillating with frequency ω_e and amplitude Z_0. It's angular displacement, ζ, can be described by a damped Mathieu differential equation:

$$\ddot{\zeta} + 2Q\dot{\zeta} + \omega^2[1 + F\cos(\omega_e t)]\sin\zeta = 0, \tag{3.1}$$

where $\omega = \sqrt{g/l}$ is the natural frequency of the pendulum, $F \equiv Z_0\omega_e^2/g$ is the excitation parameter (or the forcing) and Q is the friction coefficient. One can say that the gravitational acceleration is modified by the oscillating pivot, the apparent gravity is $g + Z_0\omega_e^2\cos\omega t$. Equation (3.1) describes a non-linear system. Whether instability occurs depends on the ratio between the natural and forcing frequency, the forcing parameter and the friction coefficient. Compare this to a yoyo: You have to move your hand up and down with a specific period to force the yoyo to move up and down. Moving too slow or too fast will not cause the intended movement of the yoyo. In a driven pendulum, instability occurs when $\omega_e/\omega \simeq 2/n$, n being an integer. The regime around $n = 1$ has the lowest threshold (caused by friction). For higher integers, much higher thresholds have to be overcome, thus requiring stronger forcing. So, when doing experiments it is important to investigate whether one can expect instability at the frequency one is working with. And whether one's forcing overcomes the threshold, though this threshold is harder to predict, since dissipative effects can become very complex in fluids (Benielli & Sommeria 1998). Fig. 3.1 shows an "instability tongue", this indicates the parameter domain where instability can be expected. The subharmonic instability at $\omega_e = 2\omega$ is easy to understand: When the pendulum moves down and the pivot moves upwards, the apparent gravity increases, enhancing the downward movement. When the pendulum moves upward, the pivot moves downward, decreasing the apparent gravity, thus enhancing the upward movement of the pendulum (compared to a fixed pendulum). Similar arguments are involved in the excitation of internal waves by parametric instability (Benielli & Sommeria 1998).

3.2.2 The oscillating platform

In our experiment, a vertically oscillating platform was used to provide the forcing for the parametric instability. The platform was controlled by a computer, with the program Wavetab, designed by Frans Eigenraam. Frequency, acceleration and amplitude, A, could be adjusted within a certain range, the range of the amplitude vs. oscillation period, T, is indicated in Fig. 3.2(b).

As can be seen in Fig. 3.2(a), the supporting construction had a scissor structure. Removable strings, attached at the bottom of the frame, compensated for the weight of the tank. Especially when the platform had to oscillate with a heavy tank, weighing around 70-120 kg, gravity caused the oscillation to become asymmetric, i.e. the platform "fell" down during the downward movement. Strong springs could balance the effect, but during our experiments the springs were too long. Since most experiments were performed with a narrow tank, which only weighed around 10

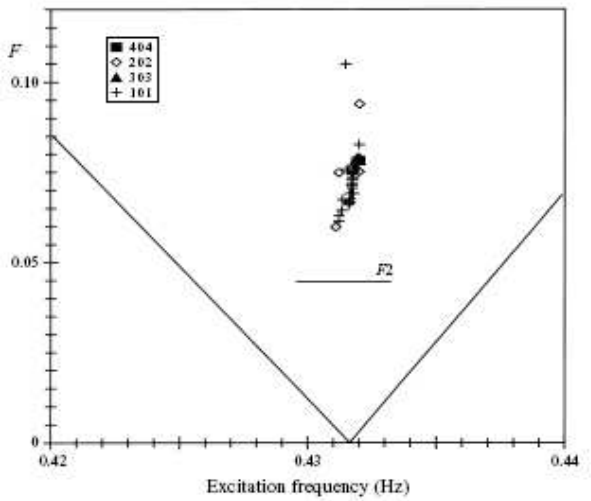

Figure 3.1: An "instability tongue" from Benielli & Sommeria (1998) of a uniformly stratified fluid. The solid lines indicate the theoretical inviscid limit for parametric instability to appear. The points indicate parameters for which parametrically excited waves are observed in their experiments. $F2$ indicates the threshold, calculated with a value for the viscosity obtained from a decay time.

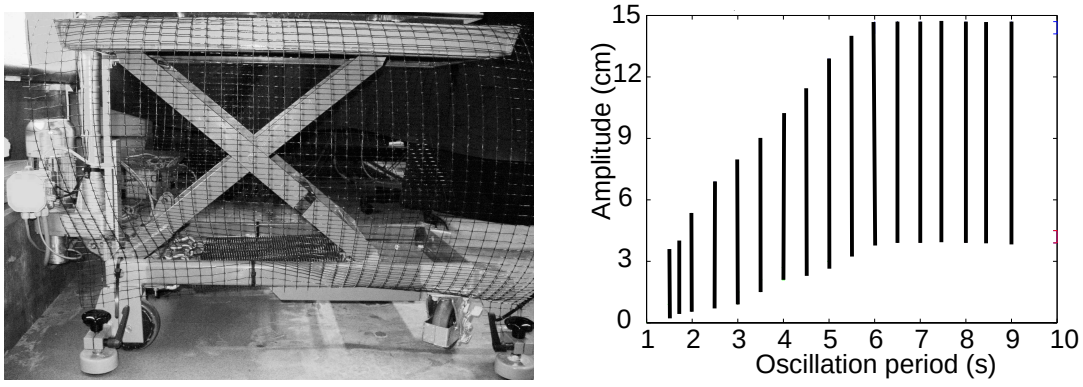

(a) (b)

Figure 3.2: (a) The scissor structure, supporting the platform and (b) the amplitude range vs. oscillation period of the platform.

kg, the oscillation was sinusoidal as required, without the springs. The limiting factor appeared to be the frequency with which the motor could oscillate the platform. There is a trade-off between amplitude and frequency; higher frequencies were possible, but this meant in some cases that the amplitude had to decreased, as indicated in Fig. 3.2(b). So it was difficult to generate/amplify waves by parametric instability, because thresholds (caused by dissipation) could not be overcome. However, we did find internal waves with a forcing lower than the threshold for parametric instability. These waves had a frequency equal to the frequency of the forcing instead of half of that. The reason for them to appear that the position of the platform was probably not purely horizontal, resulting in small horizontal movements along the vertical oscillation. This resulted in a barotropic movement, forced by the slope into (baroclinic) internal waves.

The tank on the platform was observed with a camera. In order to analyse them, the captured frames had to be taken from a stationary position (see chapter 3.3). This was solved as follows: The motor continuously gave a signal with the position (height) of the platform to the computer, which controlled the oscillation. In Wavetab, a height could be defined where the camera had to grab a frame. As soon as the table reached a defined position, a signal triggered a computer. On this computer Digiflow was installed, which controlled the camera. After Digiflow registered a signal, it triggered the camera to grab a frame. Multiple frames could be grabbed during one oscillation of the platform. Since synthetic schlieren (see next section) requires a series of images at exactly the same location and the platform moves rapidly, it is important that the timing of the trigger signal is constant and the response time is fast.
The position of the table is expressed in counts (cnts). One count is one rotation of the screw which drives the vertical movement of the table. One cnt=5.82 $\times 10^{-6}$ m, or 10000 cnts=5.82 cm.

3.3 Synthetic Schlieren

3.3.1 Introduction

Internal waves and internal wave attractors have been studied with shadowgraph techniques (Mowbray & Rarity 1967) and with dye-lines (Maas *et al.* 1997). Dye-lines allow observations with a precision in the order of mm's. The synthetic schlieren technique allows observations on a finer scale, an example of this sensitivity is shown in Fig. 3.5(a). This very sensitive method was introduced by Dalziel *et al.* (2000) to study density differences in fluids quantitatively. The sensitivity allows a detailed study of internal wave attractors, such as the development and decay of attractors and their dispersive behaviour. In this section, the synthetic schlieren method and the experimental set up are discussed.

3.3.2 From classical schlieren to synthetic schlieren

The schlieren technique is based on the fact that density gradients in a medium are accompanied by a gradient of the refractive index, n. Fermat's variational principles states that the optical path of a beam of light between two points is such that it is travelled in the least time. In other words, light takes the shortest optical path, s. When light enters a medium with a different refractive index it is refracted in all directions, but cancelled everywhere as a result of destructive interference

except on the shortest path, where constructive interference takes place, this is Huygens principle. Fermat's variational principle can be expressed as:

$$\delta \int n(x, y, x) ds = 0 \tag{3.2}$$

If the density gradients of a medium change in time, this can be observed by a change of the path of a ray crossing the medium. The classical schlieren set-up is shown in Fig. 3.3(a). The method can be described as follows: Assume that light rays enter a medium parallel, then the light rays will be bent towards the gradient of its refractive index. If the rays are focused by a parabolic mirror after leaving the medium and a knife edge is positioned in the focal point of the mirror, it will depend on the direction of the gradients, whether more or less light reaches the screen. If the direction of light is altered, it will be directed in the direction of the knife edge, or away from the knife edge. In the first (second) case, more (less) light will be obscured by the knife edge, so less (more) light reaches the screen.
Technological progress and increasing computational power allowed the introduction of a quantitative version of the schlieren method, the synthetic schlieren method. This method can be used to quantify density changes by translating changes in refractive index, thus the path of a light ray, to density changes. In this method, the refractive index is not visualised by the intensity of the light on a screen, but by an apparent change of a pattern, placed behind a fluid. If one looks to an object through a medium, with a varying refractive index, the object appears to move. Everyone has seen this on a hot day, when a hot road heats the air. The heated, rising air changes the refractive index and the background appears liquid and moving. In the case of synthetic schlieren, a background pattern is placed behind the tank, and apparent changes in this pattern are observed. Its set-up is shown in Fig. 3.3(b).

3.3.3 Optics

The coordinates x, y and z are as indicated in Fig. 3.3(b). We assume that all rays have a component in the y-direction. The Euler equations obtained from the variational problem (3.2) result in the following coupled ordinary differential equations which describe the curvature of the paths as a result of gradients of n (Weyl 1954):

$$\frac{d^2\xi}{dy^2} = \left[1 + \left(\frac{d\xi}{dy}\right)^2 + \left(\frac{d\zeta}{dy}\right)^2\right] \frac{1}{n} \frac{\partial n}{\partial x} \tag{3.3}$$

$$\frac{d^2\zeta}{dy^2} = \left[1 + \left(\frac{d\xi}{dy}\right)^2 + \left(\frac{d\zeta}{dy}\right)^2\right] \frac{1}{n} \frac{\partial n}{\partial z} \tag{3.4}$$

$$\tag{3.5}$$

Here ξ and ζ describe the path of a ray of light: $x = \xi(y)$ and $z = \zeta(y)$. Assuming light travels approximately parallel to y, $(d\xi/dy)^2$ and $(d\zeta/dy)^2$ can be neglected, thus decoupling the two equations. Using the angle at which the ray enters the medium ($(d\xi/dy)_{y=0}$, $(d\zeta/dy)_{y=0}$) and the location where the ray enters the medium (ξ_i and ζ_i) as integration constants, integrating the simplified equations results in:

$$\xi = \xi_i + y\tan\phi_\xi - \frac{1}{2}y^2\frac{1}{n}\frac{\partial n}{\partial x} \tag{3.6}$$

$$\zeta = \zeta_i + y\tan\phi_\zeta - \frac{1}{2}y^2\frac{1}{n}\frac{\partial n}{\partial z} \tag{3.7}$$

n can be decomposed into the nominal value, n_0, the unperturbed variations, n_{base} and the variations caused by perturbations, n'. If the medium is perturbed a ray will appear to emerge from a different location. The apparent shift, $\Delta\xi$, $\Delta\zeta$, caused by the perturbation can be calculated. In a system with a medium of width W at a distance B from the light source a ray enters the medium at $y = B$ and leaves the medium at $y = W + B$. Now, back-tracing results in the following relations between $\Delta\xi$, $\Delta\zeta$, the geometry of the system and the perturbations in refractive index:

$$\Delta\xi_a = \frac{W(W+2B)}{2n_0}\frac{\partial n'}{\partial x} \tag{3.8}$$

$$\Delta\zeta_a = \frac{W(W+2B)}{2n_0}\frac{\partial n'}{\partial z} \tag{3.9}$$

The density of the fluid is approximately related to the refractive index by:

$$\nabla n = \frac{dn}{d\rho}\nabla\rho = \beta\frac{n_0}{\rho_0}\nabla\rho, \tag{3.10}$$

with:

$$\beta = \frac{\rho_0}{n_0}\frac{dn}{d\rho} \approx 0.184$$

The apparent shift can be measured by comparing an image of the light source which travelled through an unperturbed medium with an image of a perturbed medium. This apparent shift can be related to a density gradient. The program Digiflow is used to calculate the changes in density gradients, by supplying the program with the required parameters (B, W, thickness of the walls of the tank, distance between pattern and camera and between tank and camera). But this can only be done if the changes in the paths of light are made visible. This is done by placing a mask with a pattern in front of the light source.

3.3.4 Imaging

If we place a pattern with horizontal (vertical) lines in front of the light source, vertical (horizontal) density changes can be measured as apparent displacements. The sensitivity to changes depends on the resolution of the CCD, the distance between the lines and thickness of these lines. A high density of thin lines can reveal smaller density changes, the disadvantage is that large perturbations will cause $\Delta\xi$, $\Delta\zeta$ to be larger than the spacing between the lines. This makes it harder to relate the perturbed image with the original image, since a line in the perturbed image cannot be related to the closest line in the original image anymore. If we use dots instead of lines, both horizontal and vertical density gradients can be resolved. And if these dots are distributed in a irregular pattern, restrictions concerning the size of the apparent shifts can be loosened. This

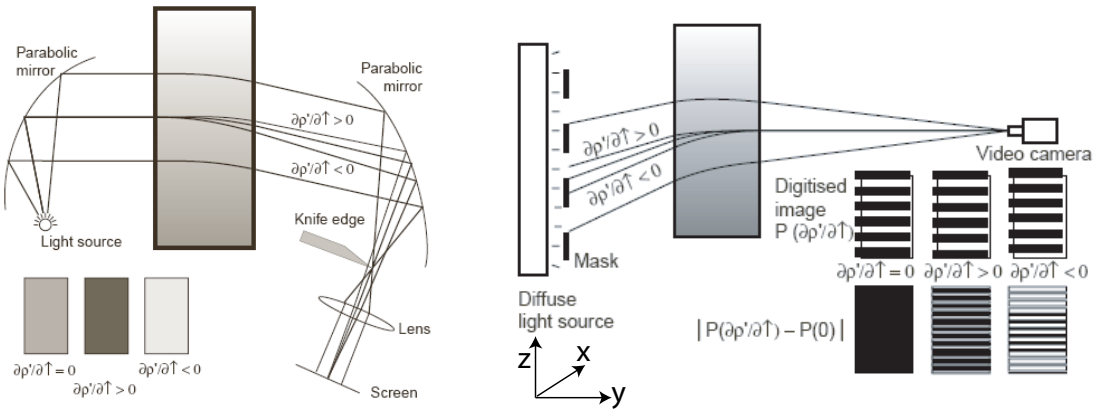

Figure 3.3: (a) A classical schlieren method, where a knife-edge obscures more or less light, depending on the changes in refractive index of the medium and (b) the synthetic schlieren method, with horizontal lines to observe vertical changes in the density gradient. Vertical lines would reveal horizontal changes and with a random dot-pattern, changes in both directions can be measured. From Dalziel *et al.* (2000).

method is called pattern matching refractometry. CPU-time increases as the pattern-matching has to be performed over a larger range of pixels. Another restriction is that the curvature terms, $\partial^2\rho'/\partial x^2$ and $\partial^2\rho'/\partial z^2$, should not distort the pattern too much (otherwise we cannot relate it with the original pattern). Furthermore, the sensitivity of the pattern matching depends on the size of the dots and the density of dots. The camera which was used was a 1.3 MPixel monochrome Jai CV-M4+CL.
Synthetic schlieren measures changes in refractive index and Digiflow translates this to perturbations in the density gradients. It gives a non-dimensional quantity, $\mathbf{b} = (b_x, b_z) = \nabla\rho'/(\partial\rho^*(z)/\partial z)$. When experiments are represented in this thesis, the colour in the figures represents b_z or b_x. These quantities can be understood if we take a look at Fig. 3.5(b). In this illustration, pycnoclines (solid), perturbed from the background stratification (dotted) by an internal wave (along the red dashed line) are plotted. If one follows the arrows, one observes gradients in the perturbation density (with respect to the background stratification) in both directions, i.e. the perturbation heights of the pycnoclines change along the arrows.

All the elements in the experimental set-up have been discussed above. The whole set-up, with the platform, camera and pattern is shown in Fig. 3.4.

3.4 Filling the tanks

The aim of the experiments was to investigate internal wave attractors in a uniformly stratified fluid. We used salinity to create density differences. For a tank with a constant length and width with increasing height, the well-known double bucket method was used. But in the case the horizontal area varies with height, this method does not result in a linear stratification. Instead, we used two pumps to create a linear stratification, which could be regulated with a computer. The

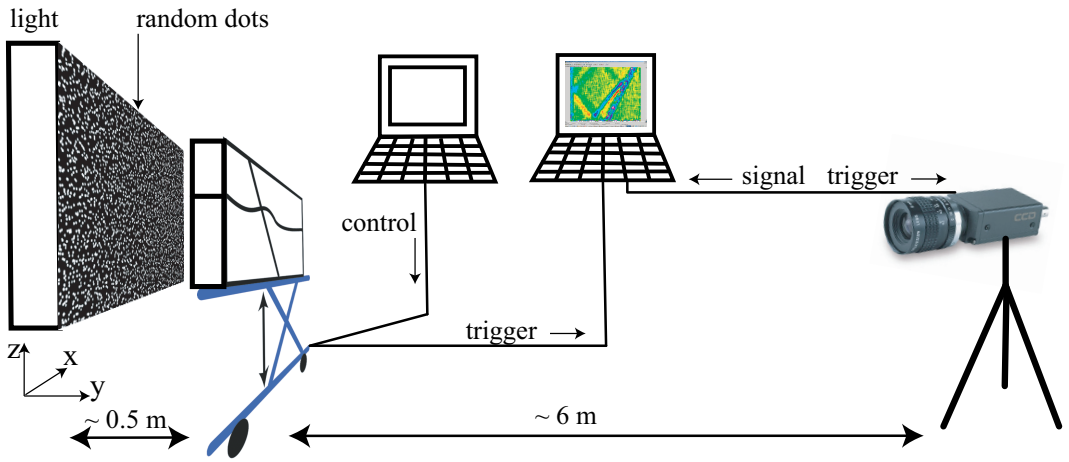

Figure 3.4: Schematic experimental set-up.

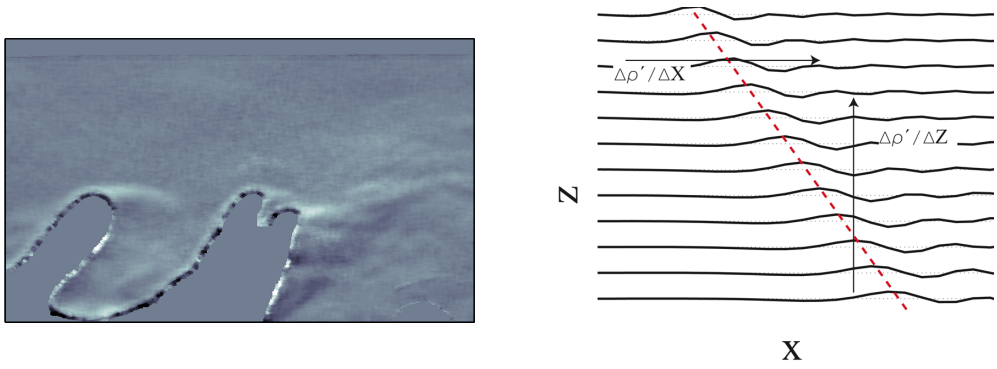

(a) (b)

Figure 3.5: (a) An example of the sensitivity of synthetic schlieren: Density perturbations, caused by a hand exchanging heat with the air. (b) Qualitative illustration of b_x and b_z. The solid black lines indicate the pycnoclines, perturbed by an internal wave. If the arrows are followed, a gradient in the perturbation height (thus density) is observed in the x- and z-directions.

two procedures are explained below.

3.4.1 The double bucket method

The double-bucket method is a very simple method to create a linear stratification in tanks with a constant length and width along the height. As the name of the method suggests, two buckets are involved. One bucket contains fresh water (BF) and the other contains salt water (BS). The tanks are connected via a tube, they are communicating. If the inflow is at the bottom of the tank, you start with water from BF. As the water is pumped in the tank, the water level in BF decreases and is balanced by an inflow of water from BS. This means the salinity of BF increases linearly with the amount of water pumped out of BF into the tank. The water pumped in the tank becomes saltier and pushes the fresh water up. If the inflow is at the surface in the tank, the procedure is the other way around. Water from BS is pumped in the tank and BS becomes fresher gradually. The strength of the stratification depends on the salinity of the water in BS, the volume of water in BS and BF and the desired volume in the tank. This means that the maximum stratification is obtained if the volume of both BS and BF is half the volume desired in the tank. In this case, BS and BF are empty at the end of the process.

3.4.2 Two pumps

If the horizontal dimensions of a tank vary with height, the doubled bucket method does not result in a linear stratification. To obtain a linear stratification, two pumps are used. The evolution of the flow rates in time depend on the geometry of the tank.
During the experiments we pumped water in a floater at the surface. A stratification with salinity S_B at the bottom and salinity S_A at the surface of the tank has to be created. We define a pump P_A and a pump P_B, with flow rate c_A and c_B, respectively. The flow rate into the floater, c_T then becomes: $c_T = c_A(t) + c_B(t)$. P_A (P_B) pumps water from a bucket with salinity S_A (S_B). At $t = 0$ we start with $c_A = 0$. The desired salinity of the tank is defined as: $S(z) = S_B - \lambda z$ where $\lambda = (S_B - S_A)/H$, H being the water level after filling. Or in terms of density: $\rho(z) = \rho_b - \frac{\rho_0}{g} N^2 z$, where ρ_B is the density at the bottom and ρ_0 is the average density. The flows from the two pumps merge in a tube, where they can mix. The salinity of the water from this tube is:

$$S_T = \frac{c_A S_A + C_b S_B}{c_T} \tag{3.11}$$

Defining $h(t)$ as the water level in the tank as a function of time, rearranging and using the definitions above results in:

$$c_A(t) = c_T - c_B(t) = \frac{c_T h(t)}{H} \tag{3.12}$$

If we assume the temperature of the water to be constant and neglect pressure differences in the tank, the relation between salinity and density becomes linear. The salinity is used for further calculations. Three different tanks were used during the experiment: A narrow rectangular tank with one sloping wall (semi-2D), one broad rectangular tank with one sloping wall (3D, this tank could be filled with the double bucket method) and a parabolic channel (3D). The narrow

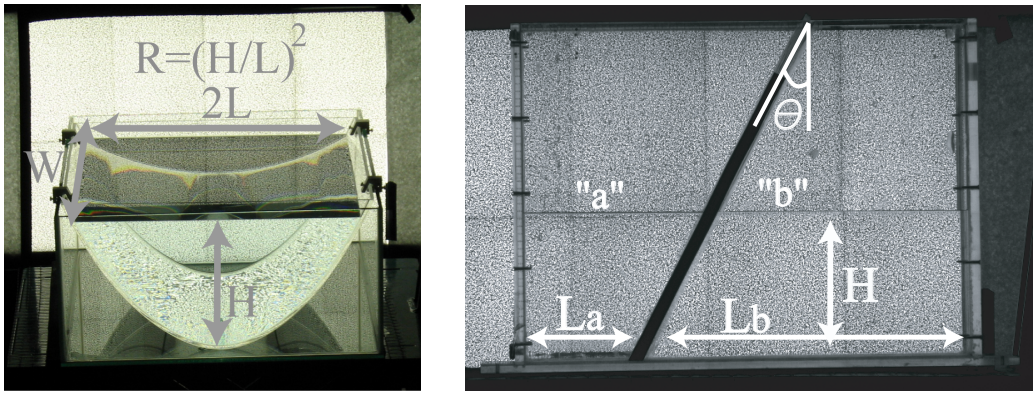

(a) (b)

Figure 3.6: (a) The parabolic channel and (b) the narrow rectangular tank with one slope (the trapezoidal basin).

rectangular tank with one sloping wall, was first filled with the double bucket method and the slope was inserted after the filling. But later, the slope was glued in the tank, because inserting the slope caused mixing, and the two pumps had to be used. The flow rates as a function of time, required to control the pumps, are calculated below for the narrow tank with a sloping wall and for the parabolic channel.

A trapezoidal basin

First we have to find $h(t)$ for a rectangular tank with a slope (or trapezoidal basin), which has two parts (as indicated in Fig. 3.6b). Part "a" has an increasing surface with height and part "b" a decreasing surface. The tank has width W, length at the bottom L_a (part "a") or L_b (part "b") and a slope with angle θ to the vertical, as indicated in Fig. 3.6(b). The total flow rate c_T is taken constant. Now the time-dependent volume, $V(t)$, in the tank in part "a" can be written as:

$$c_T t = V(t) = hWL_a + \frac{1}{2}Wh^2 \tan\theta \tag{3.13}$$

From this $h(t)$ can be obtained:

$$h(t) = \frac{-WL_a + \sqrt{W^2L_a^2 + 2W\tan\theta c_T t}}{W\tan\theta} \tag{3.14}$$

And for part "b" $V(t)$ is:

$$c_T t = V(t) = hWL_b - \frac{1}{2}Wh^2 \tan\theta \tag{3.15}$$

leading to an expression for $h(t)$:

$$h(t) = \frac{WL_b - \sqrt{W^2L_b^2 - 2W\tan\theta c_T t}}{W\tan\theta} \tag{3.16}$$

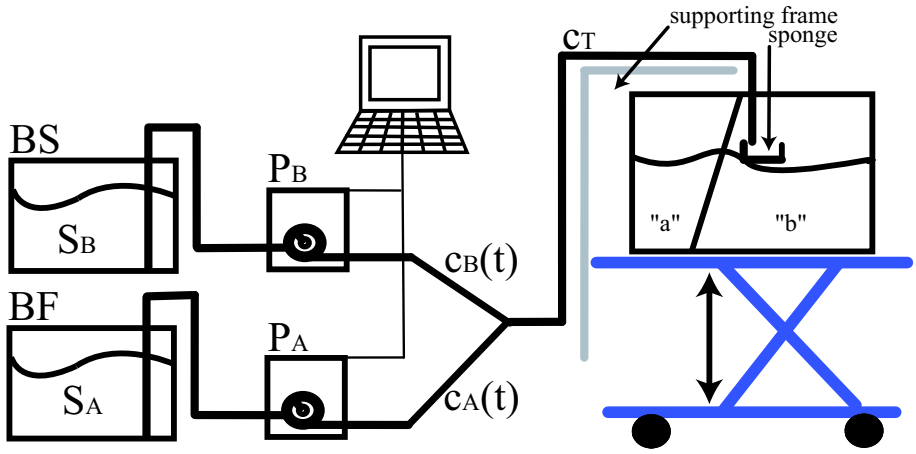

Figure 3.7: Schematic overview of the set-up during the filling process: pump P_A (P_B) pumps water with salinity S_A (S_B) with flow rate c_A (c_B), $c_T = c_A + c_B$.

Now (3.14) and (3.16) are substituted in (3.12) to obtain expressions for $c_A(t)$ and $c_B(t)$. After the slope was glued in the narrow tank, L_a, L_b and θ were: $L_a = 14.5$ cm, $L_b = 45.3$ cm and $\theta = 27°$.

A parabolic channel

The volume of a parabolic channel can be expressed as:

$$c_T t = V(t) = \frac{4WRh^{3/2}}{3\sqrt{H}}, \tag{3.17}$$

where R represents the curvature of the parabola, as indicated in Fig. 3.6. Again, h can be found:

$$h(t) = \left(\frac{3\sqrt{H}c_T t}{4WR}\right)^{2/3} \tag{3.18}$$

From the expressions for $c_A(t)$ and $c_B(t)$, a list is created with the flow rates on different times. This list is read by the program which controls the pumps and the flow rates change according to the produced list. Usually c_T is set around 0.5 litres/min. The two pumps are peristaltic Masterflex pumps. The water streams from the tube into a floater, a sponge, at the surface of the tank. The sponge prevents the inflow to penetrate too deep in the water, but promotes a more quiet inflow in the tank. During the filling, the table was moved down gradually, because the end of the tube was fixed and the water level rises. The set-up during the filling is shown in Fig. 3.7.

3.5 Adjustments of the set-up, after the first experiments

During the first experiments, we adjusted parameters in order to improve the measurements. I will discuss the most important adjustments in this section. The experiments are labelled as: “

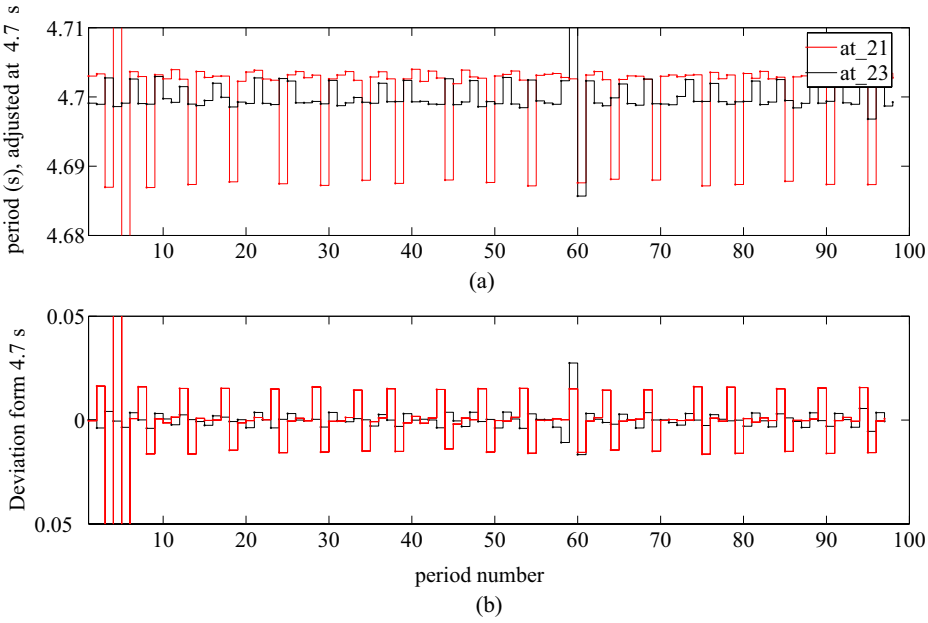

Figure 3.8: Timing of experiments "at_21" (red) and "at_23" (black), "at_23" was performed after changing wires in the COM-plug. (a) displays the time interval between the triggers and (b) the derivation from the set period (4.7 s). The variations in the interval are obviously reduced. Note the large variation at the start. This is probably caused by the build up of the oscillation.

at_xxx". "at" is an abbreviation of attractor (we were positive!) and "xxx" is the number of the experiment. The numbering is in order of realisation.

3.5.1 Timing

Since frames are compared to measure apparent movement of the dots, the frames have to be captured exactly at equal height, while the platform is oscillating . In order to do this, the trigger signal has to reach the camera after a constant interval. During the first trials, the timing appeared to be varying (around 2×10^{-2} s), as indicated by the red lines in Fig. 3.8, which shows the timing of "at_21"(red) and "at_23"(black) (with $T = 4.7$ s). Fig. 3.8(a) shows the time interval between each trigger and (b) shows the deviation from 4.7 s of these intervals. For an experiment with an amplitude of 5.8 cm and a period of 4.7 s, this implies that the height of the platform varies around of 0.5 mm, at the moment a frame is captured. This is large enough to be observed with synthetic schlieren. The trigger is a block-signal. The start of the block signal depends on the trigger, but the end of the block signal on the synchronisation with the clock of the computer. The computer that controlled the camera with Digiflow, responded to the end of the block signal. By changing poles in a COM-plug, the computer (and the camera) responded on the start of the block signal. The variations in the interval were now reduced to 5×10^{-3} s, which is shown in Fig. 3.8.

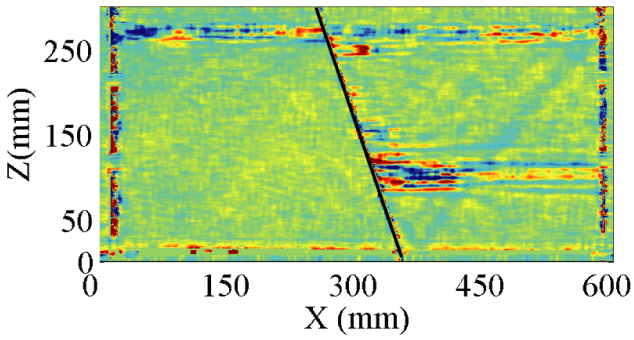

Figure 3.9: Frame of "at_7", taken just after the oscillation stopped. On the right-hand side of the slope, the horizontal lines indicate mixing layers. Colours indicate b_z (qualitative).

3.5.2 Visualisation

The quality of a synthetic schlieren measurement depends, among others, on the dots on the background image. On the camera, the dots should at least be larger than a pixel on the CCD. A random dot-pattern was used with white dots (25 % of the surface) on black (75 % of the surface). This pattern is a .ps file, specially created for synthetic schlieren. These were printed on A4 transparencies. For a camera-to-pattern distance of $\approx$ 5 m we used the following parameters in `DotsRand_Black.PS` . These were chosen in such a way that a white dot had the size of about 1.5 pixel on the CCD:

```
/inch 36 mul def
/mm  25.4 div inch  def
```

3.5.3 Stratification

During the first experiments, the slope was inserted after the narrow tank was filled (until "at_38", see Appendix A). Inserting the slope caused mixing, which was amplified during the oscillation of the tank (see Fig. 3.9, which shows b_z just after the oscillation is ceased). To prevent this the slope was glued in the tank, at an angle of 27° with the vertical. Some leakage still caused mixing layers, but this problem could be decreased by filling both parts of the tank simultaneously (one side with fresh water). Still, some mixing could not be prevented, this is visible in the synthetic schlieren images by horizontal lines and perturbations in the branches of the attractor.

CHAPTER 4

Experimental results

In this chapter I will present results of the experiments. Internal wave attractors were studied, but the series of experiments was an investigation of the experimental method itself as well. At the end of this chapter I will briefly discuss the experimental method. In chapter 5, analysis of the data and suggestions related to the experimental method are presented.
An overview of the experiments is given in Appendix A. Snapshots are shown of the experiments, just after the oscillation of the platform was stopped. The colour scale represents b_x or b_z (see section 3.3.4). Since we performed many experiments, only the most interesting, or representative ones are discussed below. The experimental set-up is shown in Fig. 3.4.

4.1 The basic outline of an experiment

Every experiment consisted of two parts. One part in which the tank was vertically oscillated (stage 1), with oscillation periods ranging between 1.5 and 12 s, and one in which the tank was at rest after the oscillation (stage 2). The oscillation was build up and ceased within two periods. During stage 1, the camera captured between one and four frames per period on fixed heights and in stage 2 the camera captured 24 frames per second. The first frames, one for each height, in stage 1 were used as reference images for the analysis of stage 1 with Digiflow. For stage 2 the last frame was used as a reference image.
Initially, we aimed on exciting internal waves by a subharmonic parametric forcing, but it appeared that the required forcing could not be supplied. However, the harmonic forcing as discussed in section 3.2.2, generated waves strong enough to be observed with synthetic schlieren. With this forcing, a stable attractor could appear in about 20 periods (cf. Maas *et al.* 1997, where it took 150 periods, with parametric excitation), this is explained in chapter 5 and by Hazewinkel *et al.* (Appendix B). From this, stage 1 was decided to take about 50 periods. Stage 2 was captured over periods lasting between 100 and 300 s, depending on the amplitude of the oscillation. By decreasing the oscillation period, a few attempts have been made to generate waves by parametric excitation, in these cases, stage 1 required more periods (of oscillation of the platform), as will be discussed in 4.2.4.
We performed the major part of the experiments with a narrow, semi-2D, tank. The amplitude of

oscillation (A) and the period of oscillation (T) were varied and surfaces with and without rigid lid were compared. A rigid lid on the surface prevents surface movements.
Apart from the narrow tank (presented in section 4.2), experiments with a parabolic channel and a big rectangular tank, with a slope, are pointed out as well (section 4.3 and 4.4, respectively). I call this 3D, though there are no along channel variations in these geometries. But the more extended along channel dimensions might allow variations in this direction.
The figures shown in this chapter are snapshots taken just after we stopped the oscillation of the platform, the colour scale represents b_x or b_z.
Values for N were calculated from the difference in density in the two buckets, BS and BF (see Fig. 3.7) and H.

4.2 The semi-2D trapezoidal basin

The experiments, discussed in this section, with the narrow basin were all performed with the slope glued into the basin. Stratification (N), depth (H), oscillation period (or frequency: $\omega = 2\pi/T$) and amplitude have been varied. Since the angle of propagation of internal waves is determined by the ratio of N and ω, varying these parameters appears interchangeable. But a stronger stratification enhances the visualisation. Since synthetic schlieren is sensitive to changes in density, a wave with equal amplitude will cause a stronger density perturbation in a fluid with higher N, since the vertical density gradient is larger. The measured perturbations were an order of 10^5 smaller than the mean density and not much larger than the noise level. Experiments "at_138" until "at_160" were performed in a very strong stratification $N \approx 3$ s^{-1}. This is reached by having a density variation of 20 % (a salt concentration between 1 gram/cm^3 and 1.2 gram/cm^3) over 20 cm. The Boussinesq approximation thus becomes questionable, but we do not consider this effect. The results could still be explained with the Boussinesq approximation. All the experiments performed with the narrow tank are indicated in Fig. 4.1, as a function of d and τ. In section 4.2.1 the results related to the variation of A are presented, section 4.2.2 is about the variation of T, the influence of a rigid lid is shown in 4.2.3 and the attempts to generate waves by parametric instability are described in 4.2.4.

The dimensions of the tank were (see Fig. 3.6): $L_a = 144$ mm, $L_b = 453$ mm, $W = 101$ m and $\theta = 27°$.

4.2.1 Varying the amplitude of the forcing

To study the effects of the forcing on an attractor (decay time, shape), we varied the amplitude of oscillation, while the other parameters were kept fixed. The experiments which will be compared are listed in table 4.1. The stratification was placed in part "a" of the tank (Fig. 3.6), $N = 1.8$, $H = 29.5$ cm and $T = 4.7$ s.

In Fig. 4.2 b_z is shown. Fig. 4.3 shows that similar results are obtained by choosing b_x, though the mixing layers (horizontal lines) are not visible in this case. The horizontal mixing layers moved up and down, which had no influence on b_x. The phase of a branch of an attractor changes upon a reflection for b_x but not for b_z, this is shown in Fig. 4.3(a). Frames captured with a phase shift of $\pi/2$ in time, with respect to Fig. 4.3, would reveal a phase shift upon each boundary reflection

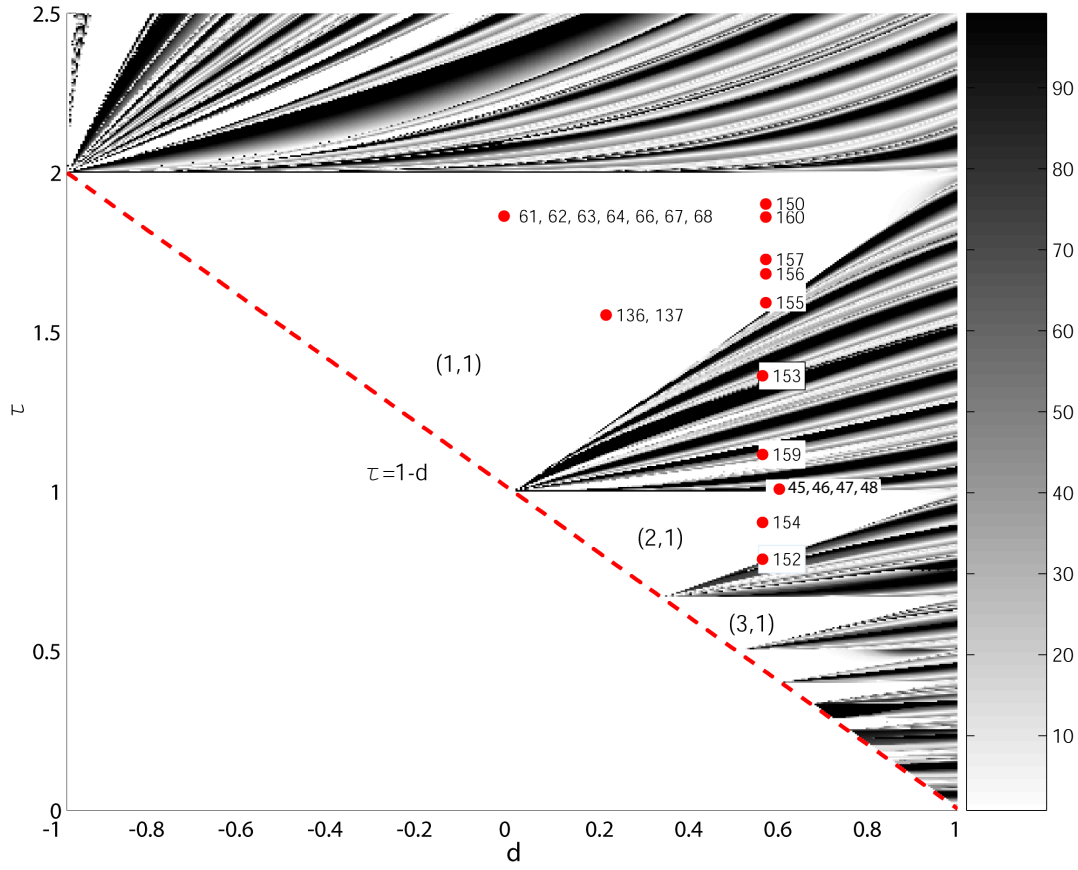

Figure 4.1: The convergence rate as a function of τ and d (see section 2.2). The values of τ and d for the experiments, discussed in this chapter, are indicated by a red dot. Their numbers correspond to the label of the experiments, thus 61 refers to experiment"at_61".

experiment (Fig. 4.2)	A (cm (cnts))
at_61 (a)	3.5 (6000)
at_62 (b)	4.7 (8000)
at_63 (c)	5.8 (10000)
at_64 (d)	7.0 (12000)
at_66 (e)	8.1 (14000)
at_67 (f)	9.3 (16000)
at_68 (g)	10.5 (18000)

Table 4.1: Overview of the series of experiments where the amplitude was varied, with $T = 4.7$ s.

in b_z, similar as those now present in b_x. The mixing layers are caused by a leak in the slope. During the filling (homogeneous water was inserted in side "b") water leaked through the slope if there was a difference in water level between both parts. After the filling, we made sure that both sides were in balance (this could be observed with synthetic schlieren), though during stage 1 some interchange might have occurred.
Attractors are clearly visible in Fig. 4.2 and the amplitude of the attractor increases as the amplitude of oscillation increases. Fig. 4.2(e), (f) and (g) show a square attractor, while in Fig. 4.2(a), (b), (c) and (d) the attractor is rectangular. If we study a sequence of frames, the direction of the phase speed is obtained. From this it can be concluded that c_g is directed clockwise along the branches. This can, implicitly, be concluded from the weakening of amplitude along the attractor. I will discuss the results more extensively in chapter 5.

4.2.2 Varying the period of oscillation

Fig. 4.1 is the same as Fig. 2.4, but now the experiments, discussed in this chapter, are indicated in it. The white areas in Fig. 4.1 indicate fast convergence towards an attractor, this is where attractors in a viscous system are expected. It is interesting to study what is observed for different values of τ, since the Lyapunov exponents are calculated for an inviscid system. By varying the period of oscillation, we varied τ.
The results, b_z, are shown in Fig. 4.4. The experiments were performed in part "b", $L_b = 453$ mm, $N = 2.9$ s^{-1} and $H = 19.5$ cm. The other experimental parameters are listed in table 4.2. H, measured at the start of the experiments, was not the depth used in the calculations of τ. A surface mixing layer was apparent, reducing the effective depth to 19 cm for "at_150" (in the beginning of the series) and 18 cm for the rest of the experiments. This caused "at_150" to have a larger τ than "at_160", despite its smaller T. In Fig. 4.4 and table 4.2, the experiments are indicated in order of decreasing τ, not chronologically, which is indicated by the label of the experiments. The white lines in Fig. 4.4 represent the theoretically expected shapes of the attractors.

During the first experiments, "at_150" (Fig. 4.4b), "at_152"(i) and "at_153"(j), we kept the amplitude low to prevent mixing. Furthermore, "at_154"(h) and "at_159"(g) could not be performed with an amplitude of 10.4 cm. This was limited by the short period of oscillation (see Fig. 3.2). In these experiments N was very high. This obviously enhances the clearness of the signal (compared to "at_61" - "at_70"). Fig. 4.4 shows that the shape and existence of an attractor depends on τ and that certain values for τ do not support attractors ("at_153"(f), "at_159"(g) and "at_152"(i)).

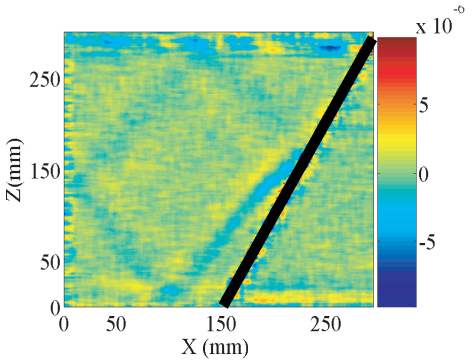

(a) at_61, $A = 3.5$ cm

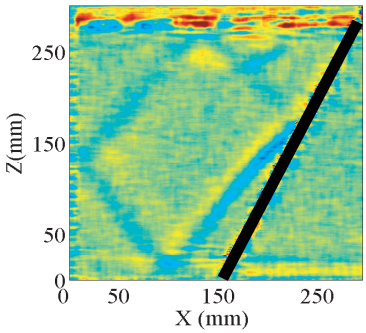

(b) at_62, $A = 4.7$ cm

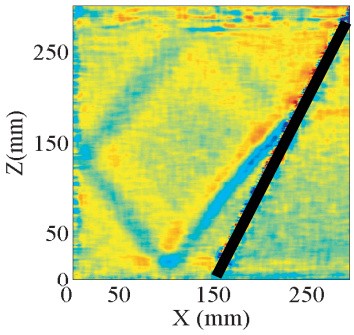

(c) at_63, $A = 5.8$ cm

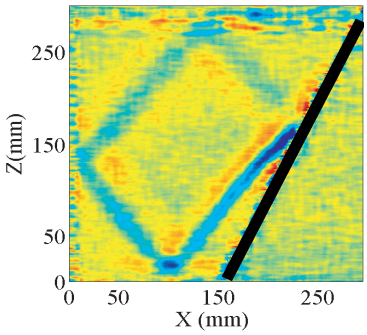

(d) at_64, $A = 7.0$ cm

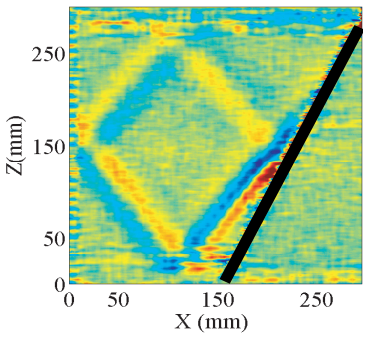

(e) at_66, $A = 8.1$

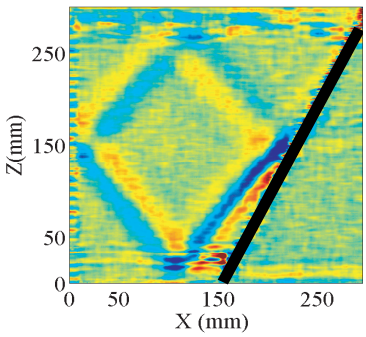

(f) at_67, $A = 9.3$ cm

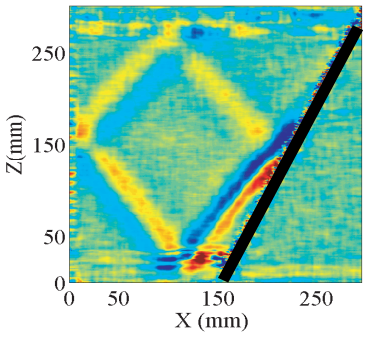

(g) at_68, $A = 10.5$ cm

Figure 4.2: Frames showing attractors, the amplitude of the forcing increases from (a) to (g). The colour scale indicates b_z as indicated by the colourbar in (a). The black lines indicate the slopes. A barotropic sloshing is converted along the slope into internal waves; the attractor weakens in a clockwise direction. The top-right branch is hardly visible in (a) and becomes clearer as the amplitude increases, from (b) to (g).

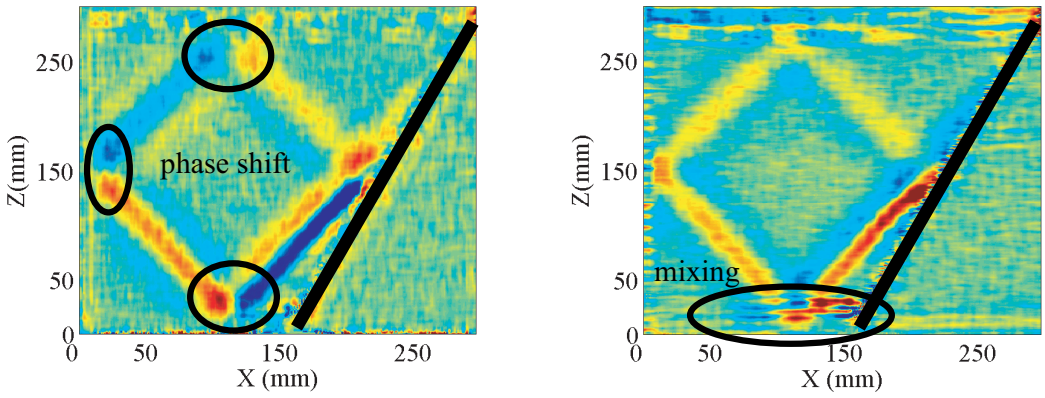

(a) at_68, b_x

(b) at_68, b_z

Figure 4.3: Example of the difference between (a) b_x and (b) b_z. In (a) a phase shift of the branches after reflection is visible (in the ellipses), this is not present in (b), but (b) clearly reveals mixing (inside the ellipse). Vertical movement causes a change in b_z; b_x is not influenced by this.

experiment (Fig. 4.4)	T(s)	τ	A (cm (cnts))
at_150 (a)	5.1	1.81	5.8 (10000)
at_160 (b)	5.3	1.80	8.7 (15000)
at_157 (c)	5	1.67	10.4 (18000)
at_156 (d)	4.9	1.63	10.4 (18000)
at_155 (e)	4.7	1.55	10.4 (18000)
at_153 (f)	4	1.32	5.8 (10000)
at_159 (g)	3.5	1.03	8.7 (15000)
at_154 (h)	3.1	0.83	8.7 (15000)
at_152 (i)	2.9	0.76	5.8 (10000)

Table 4.2: Overview of the series of experiments where the period of oscillation was varied.

In Fig. 4.4(f), (g) (i), where no attractors are visible, the movements near the bottom appears much stronger than in the experiments where the attractors were observed, in Fig. 4.4(g) stronger movements around the slope are visible as well.

4.2.3 With and without rigid lid

Lam & Maas (2007) described how a surface seiche can contribute to the formation of an attractor (see section 2.2.1). Here experiments are compared with equal parameters, but with and without a rigid lid. Results are shown in Fig. 4.5. Experiment "at_64" is compared with "at_70", which is a repetition of "at_64" but with a rigid lid. See the table 4.1 for the parameters. It is clear that the strength of the attractor became much weaker after the rigid lid was placed on the surface, but an attractor was still present.

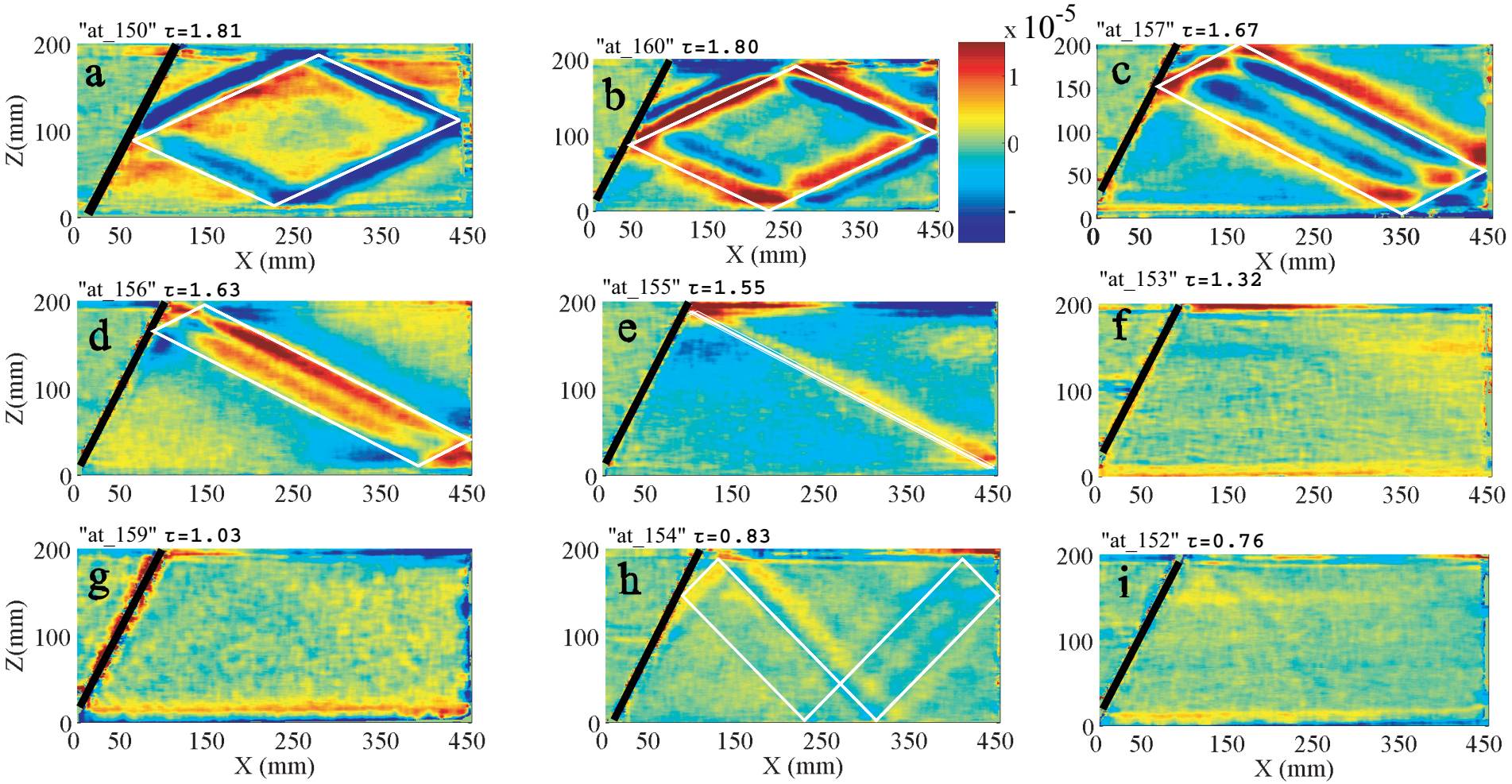
"at_150" τ=1.81
a
"at_160" τ=1.80
b
x 10^-5
1
0
-
"at_157" τ=1.67
c
"at_156" τ=1.63
d
"at_155" τ=1.55
e
"at_153" τ=1.32
f
"at_159" τ=1.03
g
"at_154" τ=0.83
h
"at_152" τ=0.76
i
Z(mm)
X (mm)
0
50
100
150
200
250
350
450

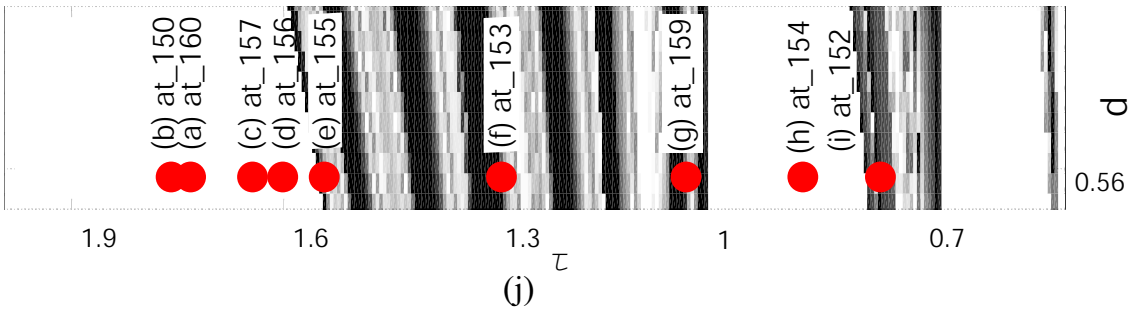

Figure 4.4: (j) A zoom of Fig. 4.1 and on the previous page: b_z in experiments (a) at_150, $\tau = 1.81$, (b) at_160, $\tau = 1.80$, (c) at_157, $\tau = 1.67$, (d) at_156, $\tau = 1.63$, (e) at_155, $\tau = 1.55$, (f) at_153, $\tau = 1.32$, (g) at_159, $\tau = 1.03$, (h) at_154, $\tau = 0.83$, (i) at_152, $\tau = 0.76$. In the experiments in the white areas of (j), an attractor is observed, while the experiments outside the white areas (or in the case of (i), on the boundary) do not reveal any attractor.

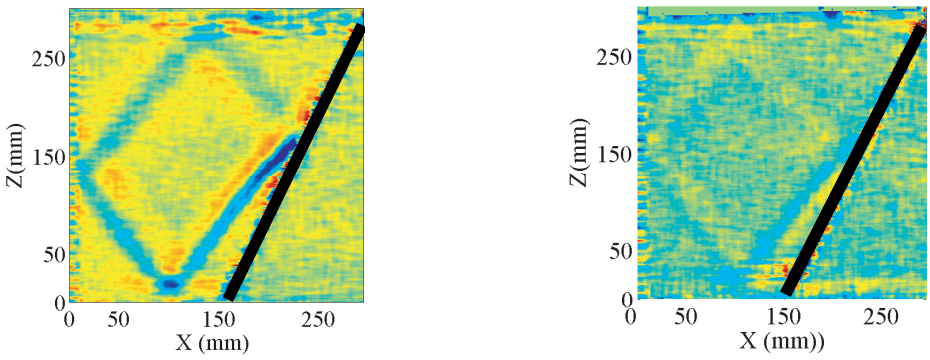

(a) at_64, without a rigid lid

(b) at_70, with a rigid lid

Figure 4.5: Experiments, b_z, (a) without and (b) with a rigid lid. See Fig. 4.2(a) for the colourbar. The attractor clearly weakens after inserting a rigid lid.

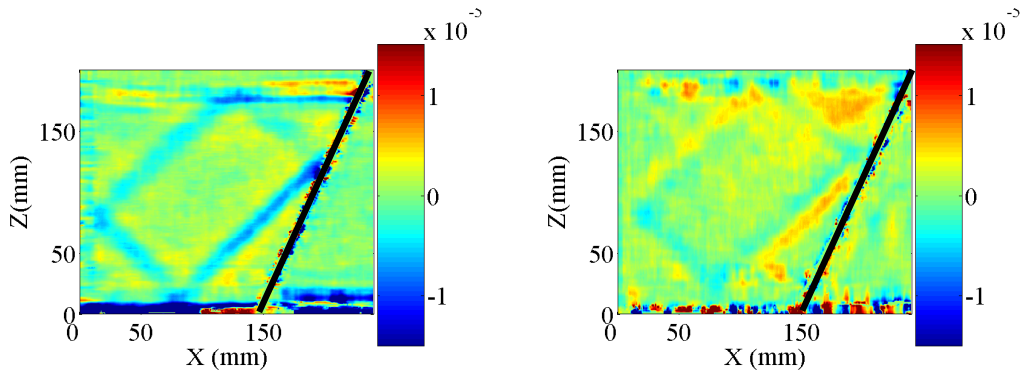

(a) at_136, $T = 3.3$ s

(b) at_137, $T = 1.65$ s

Figure 4.6: Experiments, b_z, (a) "at_136", where internal waves are generated harmonically and (b) "at_137", where internal waves are generated sub-harmonically.

4.2.4 Waves generated by parametric excitation?

Maas *et al.* (1997) generated internal waves by a parametric (subharmonic) forcing. The trade-off between amplitude and frequency (Fig. 3.2) made it very difficult, or impossible, to generate sub-harmonic waves with the platform we used. Different attempts were made, Fig. 4.6(b) shows the strongest resemblance to an attractor. Experiments "at_136" ($T = 3.3$ s) and "at_137" ($T = 1.65$ s) were taken in part "a" with $N = 3$ s^{-1}, $H = 18.5$ cm and $A = 5.8$ cm during "at_136" and 5.2 cm during "at_137", because 5.8 cm was outside the range of the platform. For "at_137" this implies $F = 0.08$ (see section 3.2.1). During "at_137" stage 1, the platform oscillated 390 times, stage 1 of "at_136" took 50 periods.
Stage 1 of "at_137" was not recorded well, the oscillation was not sinusoidal anymore, since it oscillated on the limit of its range. The triggering did not respond precisely to this rapid movement, so the captured frames could not be compared.
We also experimented with a tank with a weaker stratification, $N = 1$. This allowed lower frequencies of oscillation ($T = 4.1$ s, "at_35"), thus allowing higher amplitudes (9.9 cm), but with this forcing we did not observe parametric instability (but this is understandable since $F \sim A\omega^2$, so a decrease in ω has a stronger effect on F than the increase in A). Forcing with $T = 8.2$ ("at_36"), resulted in harmonic generation of internal waves and an attractor.

4.3 The parabolic channel

The parabolic channel contains more water than the narrow tank and this caused stronger surface movements. First "at_107" will be discussed. At the surface the horizontal dimensions were: 57 × 70 cm, in the cross and along channel direction, respectively. The depth at the deepest point was 24.7 cm, $N = 2.3$ s^{-1}, $T = 4.5$ s and $A = 10.5$ cm. In Fig. 4.7 b_x (a) and b_z (b) are shown. Different structures are revealed by the x-gradient and the z-gradient. The structures are less pronounced than the attractors in the narrow tank. This is partly caused by the stronger sloshing, which is visualised at the surface in Fig. 4.7(b) by the red and blue vertical lines. Smaller surface

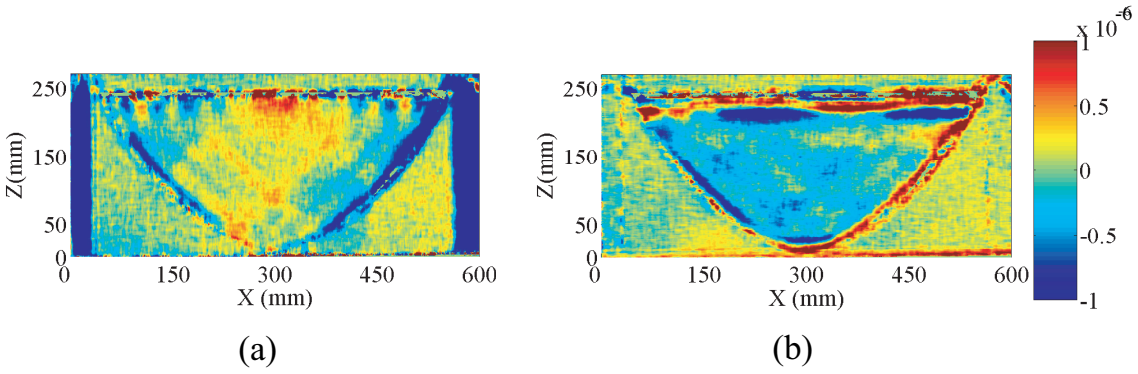

Figure 4.7: Experiment "at_107" in a parabolic channel: (a) b_x and (b) b_z. The figures reveal different structures. From b_z the larger surface movements can be distinguished, a standing mode (the red and blue horizontal lines). The field of b_x reveals smaller scale surface movements.

modes are observed from b_x. The larger sloshing, revealed in Fig. 4.7(b) is probably a result of the smaller horizontal (harmonic) movements of the platform during the oscillation and the smaller scale surface waves visible Fig. 4.7(a), which have other frequencies (1 s^{-1}), might be excited by other vibrations of the platform or parametrically.
A mixing layer with a thickness of 5 cm was present, which is visible in the field of b_z. The effective depth thus decreases to 20 cm, this results in $\tau = 0.9$. From Fig. 2.3 a (2,1)-attractor can be expected and such an attractor is vaguely present in Fig. 4.7.
The images are distorted by reflections of the random dot pattern at the walls of the tank. The camera was too close to the tank, so the sides of the tank were observed as well. In order to clean up the results, a harmonic analysis was performed on the movie of stage 2 and is presented in chapter 5.

4.3.1 With and without a rigid lid

We studied the influence of a rigid lid on the surface, in a parabolic channel. Experiment "at_113" and "at_114" are compared where: $T = 5$ s, $A = 8.7$ cm, $H = 26.3$ cm the cross channel length is 58 cm and $N = 1.7$ s^{-1}, so $\tau = 0.82$. A mixing layer is suggested in Fig. 4.8(b) of about 5 cm, which decreases τ to 0.7. From these values of τ, no attractors are expected. Indeed, no attractor can be distinguished in Fig. 4.8.
As can be seen in Fig. 4.8, and as expected, the surface modes are damped by the rigid lid. But the rigid lid did not cover the whole surface. At the sides, the surface was not covered by the rigid lid and beams appear to emerge from these points, mainly from the left side. This beam reflects at the bottom. If we compare Fig. 4.8(a), (b) with Fig. 4.8(c), (d) it is clear that the surface modes are effectively damped by a rigid lid, though a thicker rigid lid would probably damp more surface movements (now its thickness was about 1 cm).

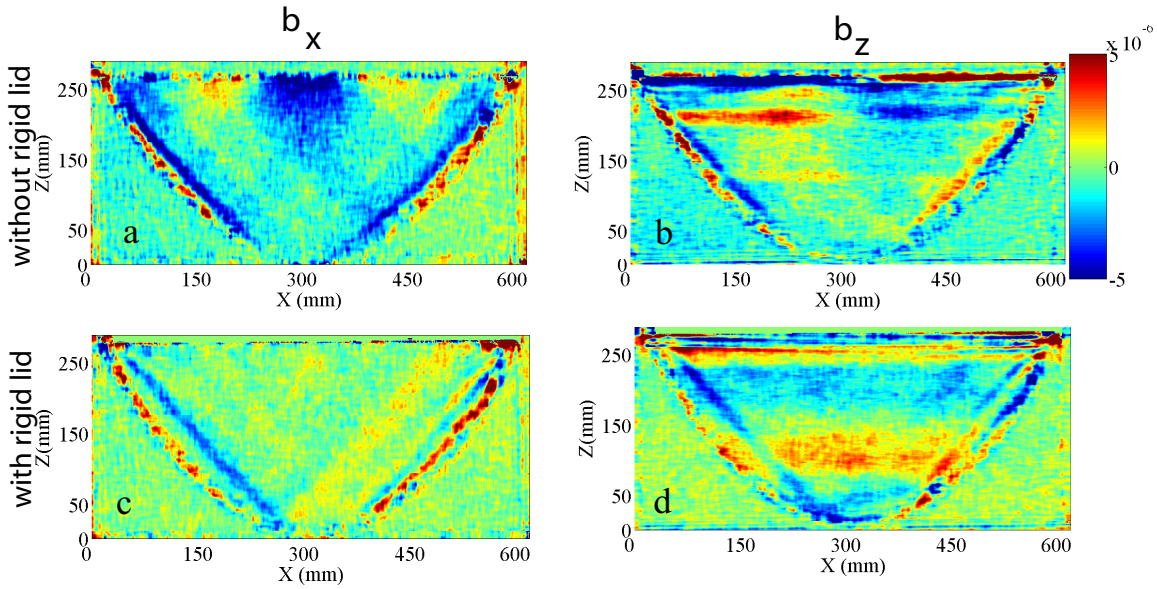

Figure 4.8: Experiments in a parabolic channel with ("at_113", (a) and (b)) and without ("at_114", (c) and (d)) a rigid lid: (a) b_x of "at_113", (b) b_z of "at_113", (c) b_x of "at_114" and (d) b_z of "at_114"

4.4 The 3D rectangular tank and miscellaneous observations

4.4.1 The 3D rectangular tank

The 3D, rectangular tank with a sloping wall contains about 90 litres of water. The dimensions of the tank were (along × cross channel) 72×62 cm. Four experiments are shown here, with $A = 5.8$ cm, $N = 2.2$ s^{-1}, $H = 25$ cm and $T = 4.7$ s. The slope was placed parallel to the along channel direction of the tank, at an angle of 26° with the vertical. During two experiments the short side of the tank faced the camera; "at_45" (Fig. 4.9a), without rigid lid and "at_46" (Fig. 4.9b), with rigid lid. During the other two experiments, the long side of the tank faced the camera; "at_47" (Fig. 4.10c, d), with rigid lid, and "at_48" (Fig. 4.10a, b), without rigid lid. Without rigid lid the surface modes were very strong, but with rigid lid the surface modes were damped. However, the rigid lid appeared to be flexible, thus allowing some surface modes. Sloshing is visible in Fig. 4.10(c) (yellow and blue interior) and (d) (red and blue at the surface). For "at_45" and "at_46" b_x is not shown here, because these images reveal similar structures as b_z. Comparing Fig. 4.9(a) with 4.10(a) we can conclude that the smaller seiche propagated along the length of the tank.
From the given parameters it follows that $\tau = 1.1$ and $d = 0.62$ (as indicated in Fig. 4.1). From Fig. 4.1 it follows that an attractor is not expected with these parameters. However, Fig. 4.10(b) reveals a mixing layer with a thickness between 2-3 cm, reducing the effective depth. With $H = 22$, τ reduces to a value just below 1. With this value an attractor with a V-shape is supported, as indicated in Fig. 4.9. Since the camera was too close to the tank, reflections of the dots at the slope and the walls distorted the images. Especially in Fig. 4.9, this effect is present, because reflections at the slope are visible as well in this case.

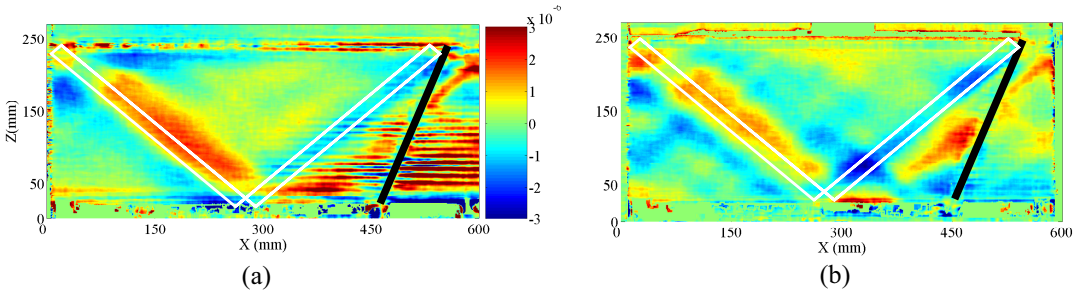

Figure 4.9: Experiments, b_z, (a) "at_45", without a rigid lid and (b) "at_46", with a rigid lid. The shape of an attractor with $\tau = 0.99$ and $d = 0.62$ is indicated (white lines).

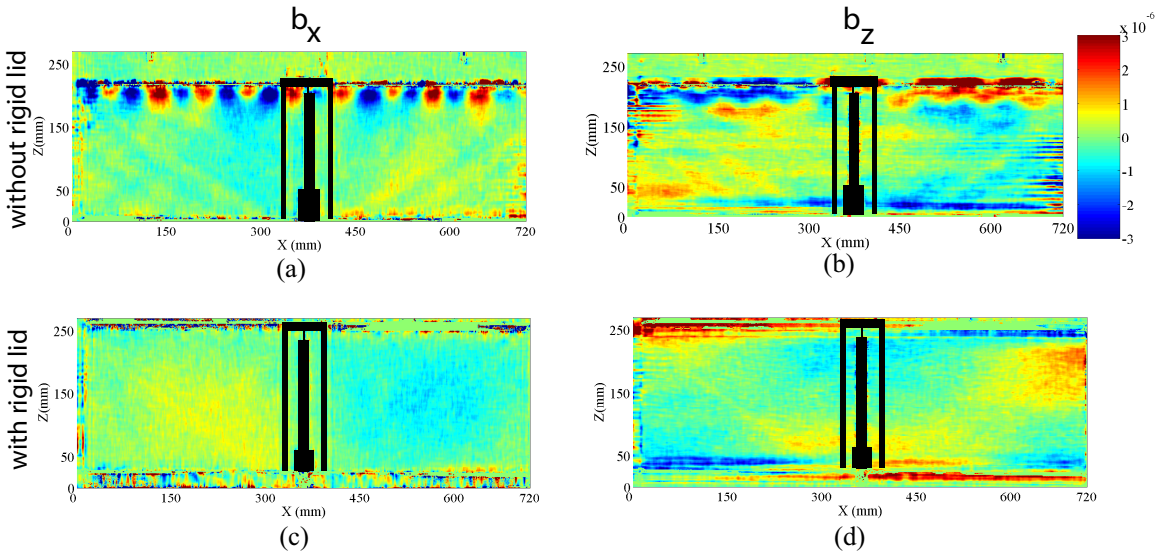

Figure 4.10: (a) b_x and (b) b_z of "at_48", without a rigid lid and (c) b_x and (d) b_z of "at_47", with a rigid lid. The surface modes are diminished by the rigid lid. During these experiments the long side of the tank face the camera, the black lines represent where the lifting construction of the platform obscures the tank and the dot-pattern.

4.4.2 Horizontal oscillation of the tank

Since barotropic movements appear to generate internal waves, moving the table purely horizontally might generate internal waves as well. Unfortunately the surface modes are very dominant and internal waves were not visible. Harmonic analysis might reveal some signal, but since the horizontal movement was done manually, the periodicity of the signal is not well defined. If the movements are forced by a motor, better results are expected.

4.4.3 Dye-lines

Experiments have been performed with dye-lines ("at_31"-"at_34"), as in Maas *et al.* (1997) . We generated the waves harmonically. The platform oscillated about 300 periods (with T =4.7/ 4.7/ 3.7/ 4.5 s), with an amplitude of 4.1/ 8.7/ 8.7/ 9.9 cm and $N = 1.85$. No visible movement of the dye-lines was observed. This shows that the movements we studied with synthetic schlieren, are not visible by eye.

4.5 Encountered problems, suggestions for further research

The platform was originally designed to generate waves by parametric instability, the amplitude range appeared to be insufficient to do this. The strongest internal waves were generated harmonically, a barotropic movement was generated as a result of small horizontal movements, accompanying the vertical movements. The generated waves were very small and the strength of the barotropic signal was not controllable, and was thus unknown at the start of an experiment. In order to generate stronger waves it could be an option to move a tank horizontally and periodically and generate a strong barotropic signal. A slope will then partly transfer this barotropic wave into a baroclinic wave. A set-up is now being made by technicians in Cambridge and Jeroen Hazewinkel and the first experiments were successfully performed with this method. The noise in the signal can be reduced by preventing air movements (caused by for example the air-conditioning) to pass by between the camera and the tank. Curtains separated the computers (and the experimenters) from the rest of the set-up, but could not prevent all "thermal noise". A tunnel (the "tent") to prevent this is now included in the set-up. The growth of an attractor by parametric instability is expected to be exponential (Benielli & Sommeria 1998; Lam & Maas 2007), while in the case of harmonic generation, the growth is expected to be linear (since the generation of waves on the slope is a continuous process), see chapter 5. This difference makes it interesting to experiment with parametric instability and including a platform with the required range of oscillation for this purpose is still worth considering. Within the scope of the IW3D-project this is not very relevant (yet), but it should be considered that a horizontal oscillation supplies an orientation to the forcing. Furthermore, the distance between the table and the camera should be increased, especially in the case of the parabolic channel and the big rectangular tank. The parallax was now too large, this means the reflections of the dots at the (side)walls were observed and the rays reaching the camera did not cross the tank perpendicular to the y-axis (see section 5.3).
We saw that in the big tanks a significant mixing layer could develop, dramatically reducing τ. It

is thus important to be aware of the τ one wants to obtain and choose τ in such a way that an attractor can be expected, even when a mixing layer arises.

CHAPTER 5

Analysis and discussion

In this chapter further analysis and discussion of the experimental results (chapter 4) are presented. Timeseries and Fourier Transforms were used in the analysis to study the results from the semi-2D tank (section 5.1). The experiments with the 3D tanks were analysed more qualitatively (section 5.2), since they contain large errors, as will be discussed at the end of this chapter (section 5.3).

5.1 The semi-2D trapezoidal basin

5.1.1 Varying the amplitude of the forcing

Fig. 4.2 shows that the branches of the attractor became more pronounced as A increased. Mixing layers were clearly present near the bottom during "at_66", "at_67" and "at_68" (Fig. 4.2 (d), (e) and (f), respectively). This is partly caused by the stronger forcing, since the strength of the mixing layers increased with A. The mixing layer near the surface was deeper in these experiments as well. This is probably because experiments "at_66", "at_67" and "at_68" were performed a day later and evaporation might have contributed to the depth of the mixing layer. The mixing layers near the bottom were produced during the filling, but they apparently grew during the night. The deep mixing layer near the surface influenced the shape of the attractor, since reflection takes place at these layers; the attractors in "at_61" - "at_64" were rectangular, while in "at_66" - "at_68", they were square. The surface mixing layer, influenced the effective depth, thus τ.
The measured angle, α, was 40 $\pm 2^\circ$, which corresponds to the estimated $N = 1.8$.
To analyse the experiments, timeseries were made of observations along a line AB, for the seven experiments. AB is indicated in Fig. 5.1.
The AB has a length of 7.2 cm, its resolution is 1.8 pixel/mm.

Timeseries

Fig. 5.2(a)-(g) shows the evolution of b_x (ordinate) of one point on the timeseries in time (abscissa, time is expressed in oscillation periods, $T = 4.7$ s). No oscillation is visible in the timeseries of stage 1, since one frame per period was captured. The value of b_x is used because during the

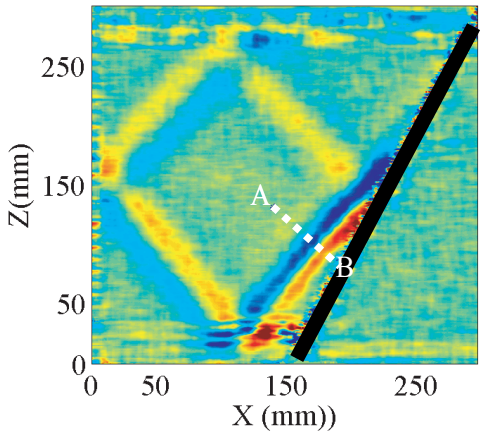

Figure 5.1: Experiment "at_68" (same as in Fig. 4.2 (g)) with the line AB of which a timeseries was made.

oscillation b_z is perturbed stronger by small variations in height of the platform, the moment a frame is captured. As can be seen in Fig. 5.2 (a), (b), (e), (f) and (g) a steady state is reached after about 20 periods of oscillation and linear growth. Fig. 5.2(h) shows the averaged timeseries of the periods 100-150. The maxima of these average timeseries (* in Fig. 5.2h) are the points on the timeseries plotted in Fig. 5.2(a)-(g). The red curves are a temporal zoom of stage 2. In Fig. 5.2(c) and (d) ("at_63" and "at_64"), a linear growth of the amplitude during stage 1 is visible. This apparent growth is probably caused by a slight shifting of the tank during the oscillation. This can be concluded from the maximum perturbation in the plots of stage 2 and from the averaged timeseries of "at_63" (red) and "at_64" (cyan) in Fig. 5.2(h), where a uniform offset in b_x is present.
These plots reassure that the amplitude of the attractor increases as A increases. The difference in amplitude of "at_66" (e), "at_67" (f) and "at_68" (g) appears to be small, but the minima in Fig. 5.2 (h) (at the right side of the maxima), reveal strong differences, here the minumum of "at_68" has the lowest value. Fig. 5.3 shows the minimum and the maximum values of the observed points (from Fig. 5.2a-g) in stage 2, of which more frames per period were captured (9 frames per period are plotted). This plot reveals a linear relation between amplitude and forcing, the solid lines are linear fits. This indicates a linear relation between the amplitude of the forcing and the barotropic movements and between the barotropic movements and the baroclinic signals, i.e. a certain ratio of the barotropic energy is converted to a baroclinic signal. Remember: The perturbations are very small, with stronger forcing, the linear relation will probably break. The range where the linear fits cross the abscissa might indicate the threshold for the harmonic generation of the internal waves.

Fast Fourier Transform (FFT) of the timeseries

We analysed the timeseries of the experiments, using a Discrete Fourier transform. As shown in Fig. 5.1, the line AB is taken perpendicular to the lines of equal phase, so the wave vector, k, can be resolved. The Matlab routine `fft.m` was used, this makes use of a Cooly-Tukey algorithm (Cooley & Tukey 1965). The temporal evolution of the wavenumber spectrum (of b_x) is shown in

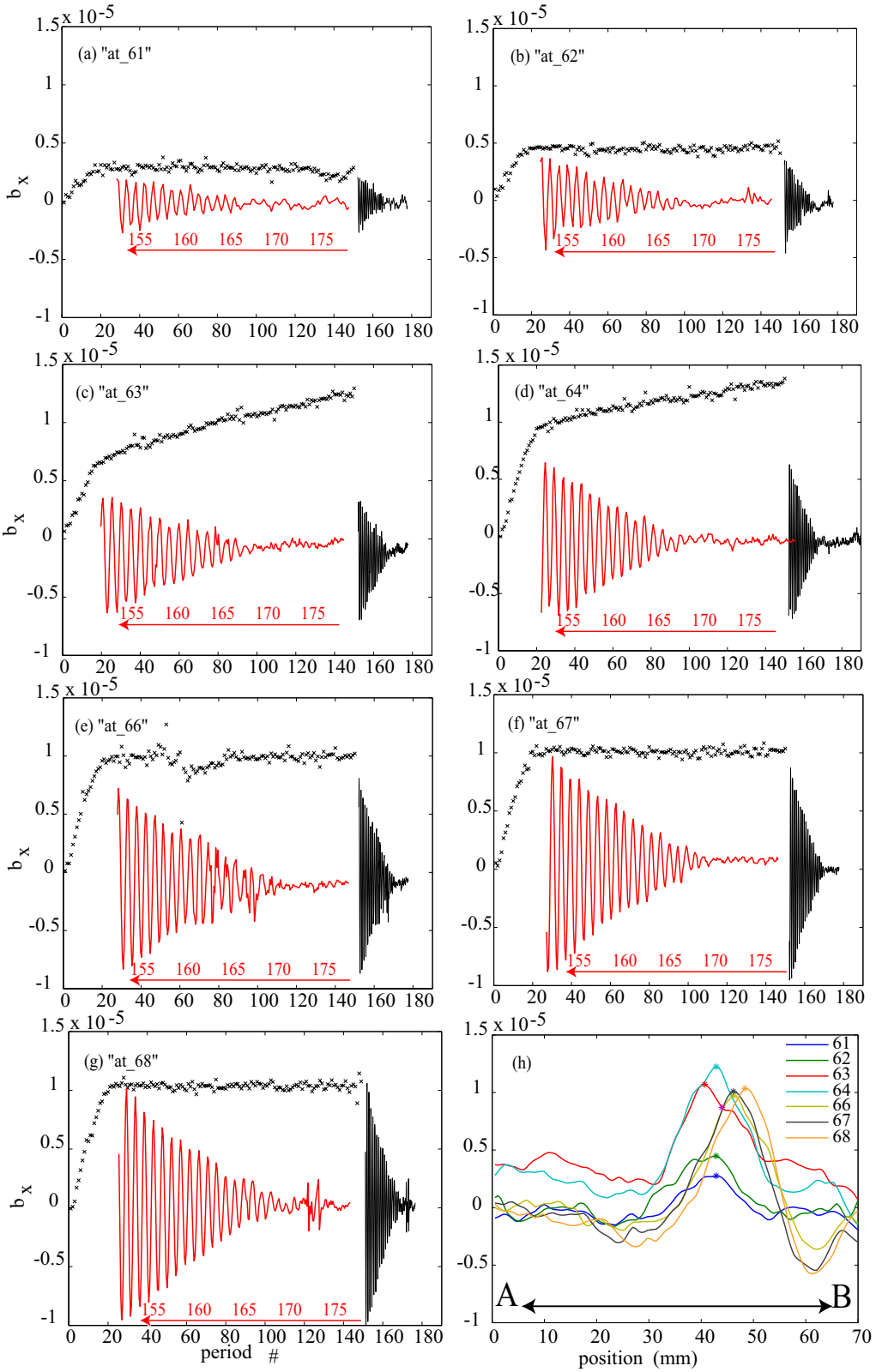

Figure 5.2: Time evolution of b_x at the points indicated by a * in (h), on AB, for the different experiments having successively stronger A (table 4.1). Of stage 1, one point per period is plotted and of stage 2 nine points per period. The red curves are a zoom of stage 2. Panels (c) and (d) show a linear growth in the amplitude, this is probably caused by a shift of the tank, since in these panels the amplitude at the beginning of stage 2 is the same as in stage 1 after about 20 periods. Panel (h) shows b_x along AB, sampled once per period, averaged over periods 100-150.

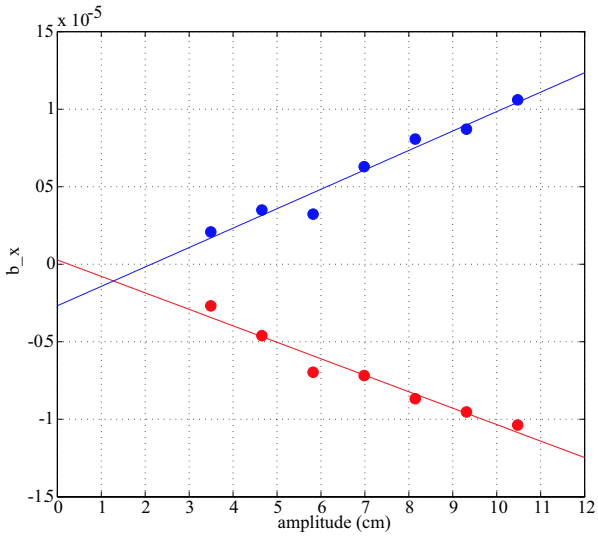

Figure 5.3: Maximum and minimum perturbation (b_x) measured in stage 2, as a function of the forcing amplitude. The solid lines indicate linear fits.

Fig. 5.4(a)-(g), the vertical axis indicates time (in periods), the horizontal axis the wavenumber (rad/mm) and the colour indicates the squared, absolute power of the wave numbers. The lower part of the figures is obtained from stage 1 and the top from stage 2, the decay of the attractors. The colour scale is not equal for all the plots, see the colourbars on top of each plot. Fig. 5.4 (h) shows the wave number spectrum averaged over the first period of stage 2, of the seven experiments. It shows that in this amplitude domain, the wave number distribution does not vary with amplitude (see section 5.1.4), the strongest k is around 0.17 rad mm^{-1}, i.e. the dominant wavelength was 3.7 cm. Performing a FFT using the values of b_z along AB results in the same shape of the spectra, though subjected to errors introduced by the vertical oscillation in stage 1.

The timeseries has been padded with zeros, in order to enhance the spectral resolution. This does not introduce errors, though it gives the spectra a smooth shape. Without padding the wave number resolution of the FFT would be $\Delta k = 0.1$ mm^{-1}. A higher spatial resolution of the timeseries would result in more noise in the spectra, though the basic shape would be the same. The timeseries have a finite length of 7.1 cm, this means that the largest wavelength which can be resolved by the FFT is 14.2 cm, i.e. $k = 0.04$ mm^{-1}, indicated by a dashed line in Fig. 5.4(h). The lower wave numbers apparent in the spectra are a result of a trend or an offset in the timeseries. These lower wave numbers are very strong in "at_63" and "at_64", from period 30 on, as a result of a movement of the tank during stage 1 (see section 5.1.1).

This analysis reveals for all the experiments an increase of the dominant wave number during the build up in stage 1. After about 20 periods, the internal wave field reached a steady state: At a certain wave number, the production of this wave number was in balance with the dissipation by viscosity. Because the steady stage was reached after about 20 periods, period 40-150 are not shown. When the oscillation was stopped, a weakening of the amplitude took place and

the dominant wave number increased. These observations are discussed in Appendix B and are briefly discussed in the next section. The paper in Appendix B is an article by Hazewinkel *et al.*, submitted to the Journal of Fluid Mechanics. It discusses a widening of the branches along the attractor (following the group velocity vector) as well.

Discussion

The evolution of the wave number spectrum can be explained by a simple model. This is discussed in Appendix B, where an analysis is presented of "at_150". Here a summary is given.
We consider the fact that the group velocity of internal waves depends on the wave vector length, k: $|\mathbf{c}_g| = \sin\alpha/k$. Furthermore, we consider that the wave number increases by a factor γ upon each reflection (Fig. 1.3):

$$\gamma = \frac{\sin(\alpha+\theta)}{\sin(\alpha-\theta)}, \tag{5.1}$$

(e.g. Gostiaux 2006). For "at_61" - "at_70" $\gamma = 3.6$. If a wave with wave number k_0 travels around the attractor, it will be focused upon reflection at the slope. Now it will have wave number $k_1 = \gamma k_0$. It will take the wave t_{loop} to cycle the attractor once:

$$t_{loop}(k) = \frac{L}{c_g(k)} \tag{5.2}$$

where L is the total length of the attractor (in this case 60 cm). A wave with wave number k_0 will have wavenumber $k_n = k_0\gamma^n$, after n reflections. The n^{th} reflection takes place after:

$$t_{sum}(k_n) = \sum_{i=0}^{n-1} t_{loop}(k_i) \tag{5.3}$$

In Fig. 5.4(g) t_{loop} is indicated in the decay phase as a function of k as a solid, white line. When the forcing is stopped, a wave with wave number k_i will be converted to a higher wave number after $t_{loop}(k_i)$. This means that the lowest existing wavenumber k_{min} will be lost after $t_{loop}(k_{min})$, since it will then be converted to γk_{min}. The line shows that the smaller wave numbers vanished after one cycle around the attractor. The dashed line in stage 2 indicates t_{sum}. The evolution of the dominant wave number follows this line very well, which means the dominant wave numbers vanished because they are converted to higher wave numbers. This line is shifted in such a way that it starts at the dominant wave number. When the forcing stopped, the dominant wavenumber immediately decayed, it takes more time for the higher wave numbers to decay (to cycle the attractor once), so the higher wave numbers could become dominant. The grey line is a line parallel to t_{loop}, this line follows the evolution of the dominant wave number later in the decay, which means the weaker, higher wave numbers (still produced during the decay), vanish quicker. The fact that the *shifted* lines of t_{loop} and t_{sum} describe the evolution of the dominant wavenumber indicates that the described process already took place during stage 1, but was overshadowed by the production of lower wave numbers. The spectral evolution during stage 2 is thus determined by:

- The elimination of the dominant wave number by focusing, i.e. conversion towards a higher wave number.

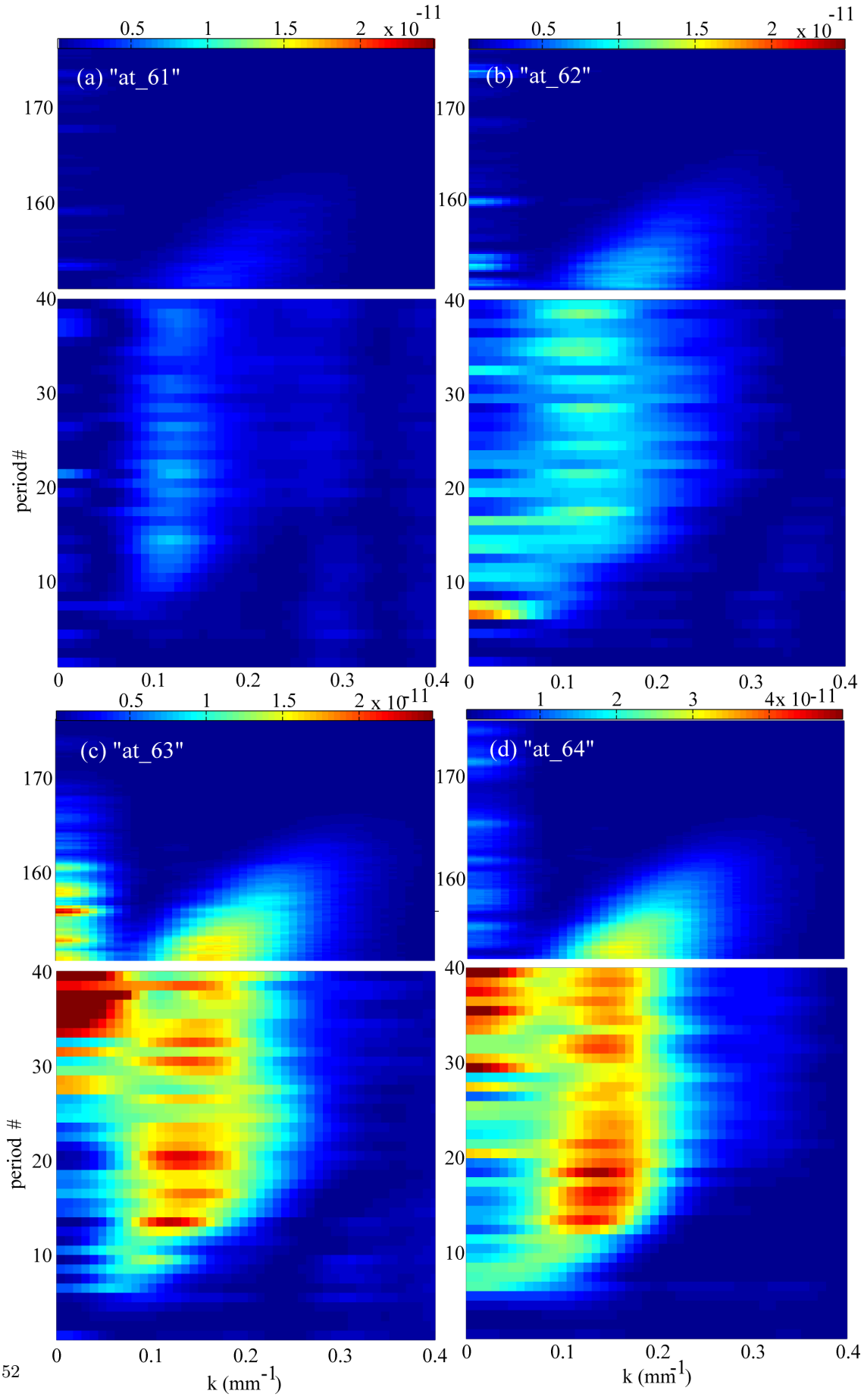
(a) "at_61"
(b) "at_62"
(c) "at_63"
(d) "at_64"
0.5 1 1.5 2 x 10-11
1 2 3 4x 10-11
period#
period #
k (mm-1)
170
160
40
30
20
10
0 0.1 0.2 0.3 0.4

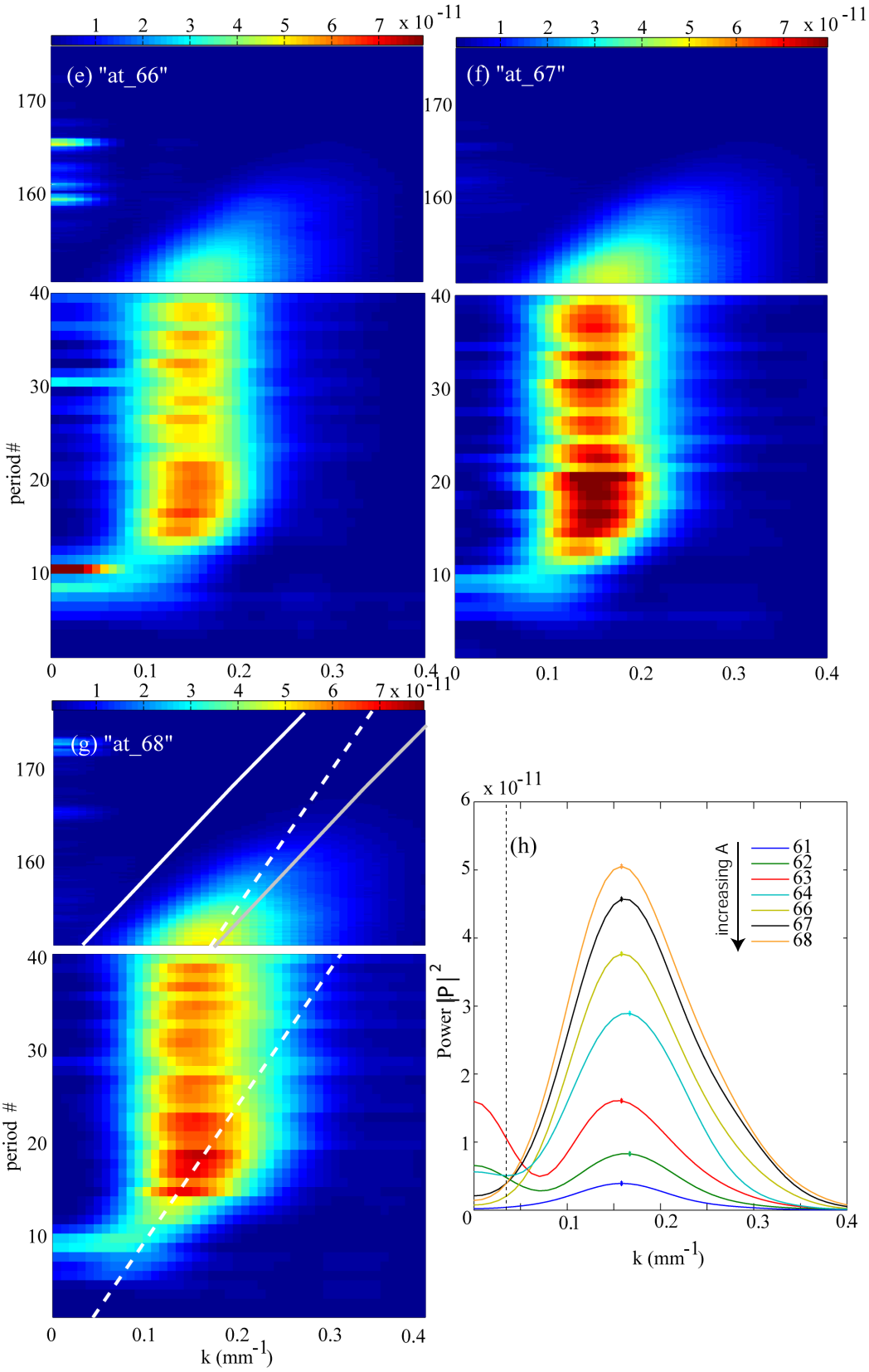

Figure 5.4: ((a), (b), (c) and (d) on previous page) Discrete Fourier Transform of the wave number spectrum of b_x. The colour scale indicates the absolute, squared power of the wave numbers. In (g) the dashed lines indicate t_{sum} as a function of k and the solid white (grey) line indicate t_{loop} (a line parallel to t_{loop}) Panel (h) shows the wave number spectra, averaged over the first period of stage 2, of the same experiments.

- The dissipation of the dominant wave number along a cycle around the attractor, which takes more time for higher wave numbers, with smaller c_g

During stage 1, the evolution of the maximum wave number is described very well by t_{sum} (dashed white lines), where k_0 was calculated from the maximum wavelength possible in the tank, i.e. from the scale of the tank, $k_0 = 2\pi/400$ mm^{-1}. So waves at the scale of the tank are generated, the long waves have a larger c_g, and cycle around the tank to become smaller by focusing.
The shape of the spectrum for smaller wave numbers (relative to the dominant wave number) is determined by the decreasing c_g for higher k. Longer waves are converted very fast to shorter waves, which have a smaller c_g and thus exist longer. At the right side of the dominant wave number the shape is determined by the balance between production and dissipation of wave numbers. Dissipation of higher wave numbers is stronger, since their c_g is smaller, allowing viscosity to act longer on these wave numbers and the fact that viscosity acts on the smaller scales.

5.1.2 Mixing

Experiments "at_68" is also used to study the mixing. The mixing layers were produced during the filling as a result of a leaking slope. The reference frame, which was used to calculate the apparent movements of the dots, was the last frame of stage 2. This frame was captured at $t_{ref} = 300$ s after the oscillation of the table was stopped. If another reference frame is used, the behaviour of the mixing layers can be studied. If a mixing layer is not present anymore after 300 s, but is still present around 120 s, the mixing layer will appear weaker in the field of $\mathbf{b}$ when the reference frame with $t_{ref} = 120$ s is used. The mixing layer in the reference frame will cancel the mixing layers in the analysed frames. Fig. 5.5 shows the field of b_z at $t = 60$ s, calculated with a reference frame at (a) $t_{ref} = 120$ s and (b) $t_{ref} = 300$ s. An apparent *weaker* mixing layer will indicate a *stronger* mixing layer in the reference frame. Indeed, the mixing layers near the bottom appear weaker when a $t_{ref} = 120$ s is used. This means that the weakening of the mixing layers took place in the order of minutes. The mixing layers were still present, since they appeared on the same height in each experiment ("at_66", "at_67" and "at_68") but they were amplified during the experiments.

Fig. 5.5, showing b_z at $t = 60$ in stage 2, displays an attractor with shorter waves than in Fig. 4.2(g), taken in the first period of stage 2. This illustrates the evolution of the wave number spectrum, from longer to shorter waves, in stage 2.

5.1.3 Varying the period of oscillation

Fig. 4.4 shows that strong (1,1)-attractors (one reflection at the surface, one on the wall) existed which corresponds to the (1,1) area in figure 4.1. As τ was decreased, the shape of the attractor changed, until it was just a line ("at_155"). The fields of $\mathbf{b}$ in "at_153" and "at_159" did not have any internal structure, this can be expected since their τ was located in the more grey and black areas in figure 4.1, i.e. the convergence towards an attractor was very weak in this region. Decreasing τ further, resulted in the appearance of a (2,1)-attractor. Note that the perturbations were significantly weaker, indicating that reflections and the length of the attractor damp the waves. "at_152" was located on the border between the white, (2,1) area and the less converging regime. Not much structure can be distinguished, though a weak V-shape is visible.

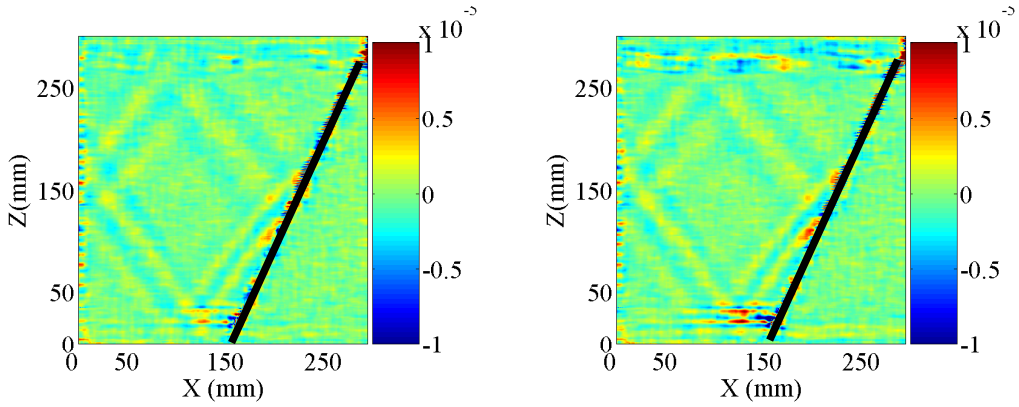

Figure 5.5: b_z, at $t = 60$ s in stage 2, of "at_68" calculated with a reference frame at (a) $t = 120$ s (b) $t = 300$ s. In (a) the mixing layers appear weaker, which means a stronger mixing layer is present at $t = 120$ s than at $t = 300$ s.

In the experiments where no attractors was observed a lot of movements were apparent near the bottom (and the slope, in "at_153"). When there is no convergence, internal waves are still generated along the slope. So what we see near the bottom might be caused by internal waves reflecting along the whole length of the bottom.

Fast Fourier Transform of the timeseries

Timeseries were made of stage 2 of "at_150" (line segment length=8.1 cm, resolution=1.8 pixel/mm), "at_154" (length=7.7 cm, resolution=1.3 pixel/mm) and "at_156", where b_z was used. The timeseries were taken in the strongest branch of the attractors (as in Fig. 5.1), again perpendicular to a beam. For "at_156" this is complicated since the two branches coincided (one with c_g directed to the slope and one from the slope), for this experiment 3 timeseries were used, as indicated in Fig. 5.6(f). One timeseries was made on the line indicated by "low", one on the line "top" and one of the two together (length=16 cm, resolution=1.6 pixel/mm). The timeseries of three experiments were analysed with a Discrete Fourier transform, as in section 5.1.1. The results are shown in Fig. 5.6(a)-(e), the evolution of the wave numbers during the decay are similar to those discussed in the previous section. The solid (dashed) lines indicate t_{loop} (t_{sum}). The decay of the smaller wave numbers in the spectrum is not described by t_{loop} (as in Fig. 5.4) for "at_150" and "at_156". In "at_154" t_{loop} follows the evolution of the smaller wave number very well. An explanation for this difference can be the strength of the attractor, the perturbations in "at_150" and "at_156" are stronger than "at_154" and "at_61" - "at_68". Stronger waves, with lower k's, might survive a reflection. The experiments took place in side "b" of the tank, which is longer than side "a". The sloshing is stronger in side "b", also in stage 2, and might have contributed to production of the lower wave numbers during stage 2.
The evolution of the strongest wave number is described by t_{sum} very well, in all the experiments. This indicates the influence of focusing of wave numbers on the evolution of the spectrum, during the decay.

The FFT's in Fig 5.4 and Fig. 5.6 reveal that the maximum wave number varied with the shape of the attractor. The length of the attractors in "at_61" - "at_68" is approximately 65 cm, of "at_150" 80 cm, of "at_154" 100 cm and of "at_156" 75 cm. If "at_150" is compared with "at_68", it can be concluded that in the longer attractor the balance between dissipation and production of higher wave numbers (smaller wavelengths) is reached at a lower wave number than in the shorter attractor. The attractor of "at_154" reflects six times in one cycle, and the attractor is much weaker, which suggests that these reflections (and intersection of the branches) influence the strength of the attractor, but the dominant wave number might be influenced as well. The relation between attractor length and wave number is also discussed in Appendix B: The longer the attractor, the more time viscosity has to acts on the wave. Shorter waves travel slower, so viscosity acts longer on a wave during one cycle, thus diminishing the strength of these wave numbers. The difference in the dominant wave numbers is shown in Fig. 5.7, where the normalised power of the FFT vs. the wave numbers is shown for "at_68", "at_150", "at_154" and "at_156". The averaged FFT of the first period in stage 2 was used. The wave number of "at_156" was influenced by the interaction between the two branches, this might explain the relatively large difference between its spectrum and those of "at_150" and "at_154". Furthermore, the smaller dominant wavenumber is not resolved by the timeseries "top" and "bottom". This is because this wavenumber corresponds to a wave which "emerged" from the line, dividing the two timeseries. This wave splits in an upward and downward propagating part, this wave number is thus composed of two waves and hence artificial.

The insensitivity of peak wave number on A, as analysed in section 5.1.1, implies that the shear in velocity (larger amplitudes imply stronger shear) is less important for the wave number spectrum than the length of an attractor, as discussed in this section. *The wave number spectrum is thus determined by the shape of the attractor rather than its amplitudes.* Again, it is important to emphasise the relatively small amplitudes in all the experiments.

5.1.4 The wave number spectrum, forcing amplitude vs. length

In this section, the statement that the wave number spectrum is determined by shape of the attractor is investigated. The *right hand side* (with respect to the peak) of the spectra is studied here, since this is determined by dissipation. Fig. 5.8(a) shows the normalised wave number spectra of the experiments discussed in section 5.1.1, the spectra which were normalised are shown in Fig. 5.4(h). No apparent differences in shape are revealed, though the right side of the peak shows more variation than the left side. The shape of the left side is determined by focusing of the wave number, the right side by viscosity. The Kolmogorov microscale is defined as: $\eta = (\nu^3/\epsilon)^{1/4}$, where ν is the kinematic viscosity and ϵ the energy transfer rate (so the transfer of energy to higher k, to be dissipated). The Kolmogorov microscale is a turbulence length scale, which indicates the scale at which turbulent movements are independent of the large scale motions. This scale sets the decay rate of the energy as a function of k. It is used to describe the energy distributions in open, 3D systems (e.g. the atmosphere and oceans Phillips 1977). Since ϵ is a function of the amount of energy in the system, η depends on the energy in the system. Since the shape of the spectrum in 5.8(a) hardly depends on the forcing amplitude, thus the energy input, the Kolmogorov scale is not helpful in predicting the shape of the spectra. This can be understood from the geometries we study here: closed domains, where wave numbers increase upon supercritical reflections.

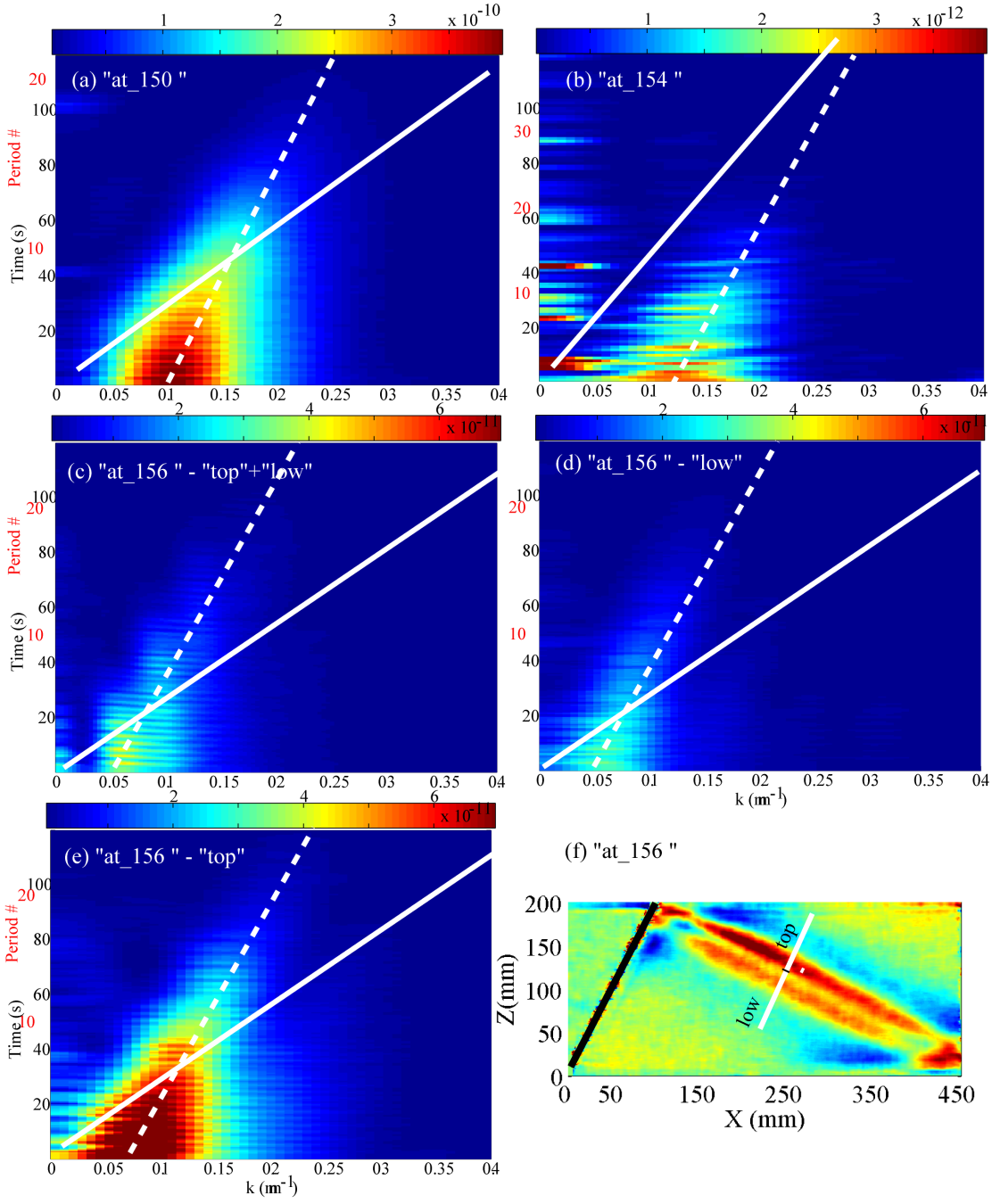

Figure 5.6: Discrete Fourier Transform of the wavenumber spectrum of b_z. The colour scale indicates the squared, absolute power of the wave numbers. (f) shows a snapshot of "at_156" and the lines "low", "top" and "low"+"top" of which timeseries were made and used for the FFT.

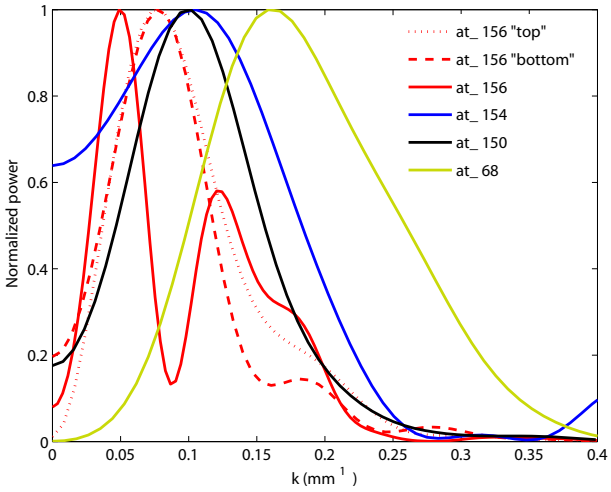

Figure 5.7: Normalised power of the FFT vs. wave number of "at_68", "at_150", "at_154" and "at_156". The spectrum is averaged over the first period of stage 2. A shift in the peak wave number is clearly visible

The scale, which is assumed to determine the shape of an attractor is the length of the attractor, L. Fig. 5.8(b) shows the spectra of "at_68"(green) and "at_150" (black), but now as a function of a scaled wavenumber, kL. L of "at_68" is 65 cm and L of "at_150" is 80 cm. Experiments "at_68" and "at_150" are compared because they are both measurements (1,1)-attractors with a significantly different length. The wave number spectra are normalised in order to be able to compare them, cf. the spectra in Fig. 5.4 and Fig. 5.6.
The scaled spectra do not coincide, but the envelope of the (scaled) spectra have more similarities than the spectra in Fig. 5.7 and their peak wave numbers are drawn closer. From this, we can conclude that the length of an attractor is a relevant scale in its wave number spectrum. More spectra, of attractors with significant length differences, must be compared to assure this claim.
It is important to note that the FFT's were obtained from timeseries describing the value of **b**, not the velocity v (which has a straightforward relation with the energy: $E \sim v^2$). This means the spectra do not express the energy distribution, $E(k)$ over the wave numbers.
The dominant wave number in $E(k)$ is expected at smaller wave numbers, as confirmed by the spectra obtained from a PIV measurement (Hazewinkel *et al.* 2007). So a similar analysis has to be performed on a number of "PIV-spectra". See Appendix B for more analysis of the wave number spectra and their relation to the attractor length.

In this section, it is confirmed that the length of an attractor is an important scale to describe its wave number spectrum, more important than the Kolmogorov microscale, which depends on energy input. But this accounts for the spectra obtained from **b** and not the velocity fields.

5.1.5 With and without a rigid lid

When a rigid lid was placed on the surface, the internal waves became very weak. The oscillation of the table generated a barotropic movement in the tank. A part of this movement was converted to a baroclinic signal on the slope. If a rigid lid is placed it restricts the barotropic movement,

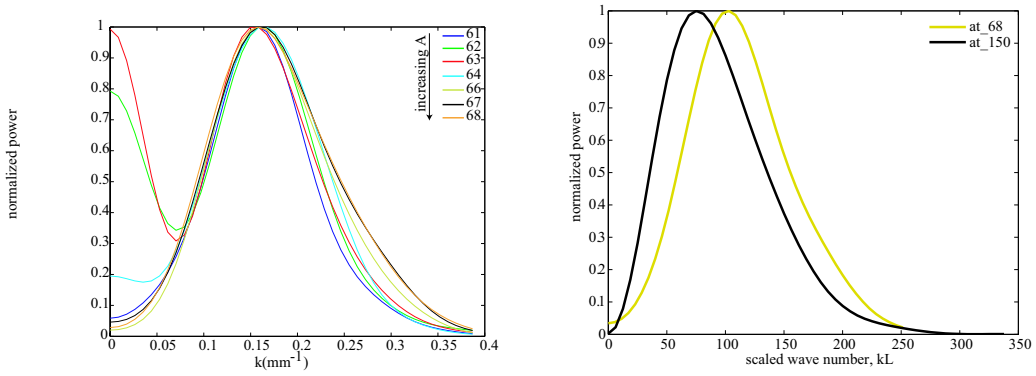

Figure 5.8: Panel (a) shows Fig. 5.4(h), but now normalised and panel (b) shows the normalised spectra of "at_68" and "at_150" (Fig. 5.7) but now vs. the scaled wave number: $k \times L$, where L is the length of the attractors.

hence the weakening in the generation of the baroclinic signal.
To analyse "at_64" and "at_70", timeseries along a line near the surface were made. Since the surface movements are revealed by variations in the vertical gradient, b_z was used. Fig. 5.9(a) and (b) show these timeseries of "at_64" (with) and "at_70" (without rigid lid), respectively. To remove noise, the averaged value of each point over time was subtracted from the timeseries. These plots reveal strong surface movements in "at_64", and weaker surface movements of "at_70". Fig. 5.10(a) and (b) show b_z on the timeseries at two moments in the beginning of stage 2. In Fig. 5.10(a) ("at_64") the two lines show a clear up and down movement, while Fig. 5.10(b) ("at_70"), shows hardly any differences between the two lines, this was also the case for other moments during stage 2. Fig. 5.10(c) and (d) show the evolution in time of a point at the left end of the timeseries for both experiments (blue) and the evolution of b_z on the attractor (on the line AB, Fig. 5.1) in red. Fig. 5.10(c) ("at_64") reveals a periodic movement, the period of this movement is close to $T/2$, but not exactly, so it is can not be directly related to the attractor. The periodic surface movements are not apparent in Fig. 5.10 (d) ("at_70").
The analysis above show that the movements just below the surface are damped by the attractor. The period of the surface movements in "at_64" is too long for a surface wave, it might be a standing wave in the interface between the surface mixing layer and the stratification. Assuming a shallow water wave with reduced gravity having frequency $\omega = \sqrt{g'k^2H}$, where $\omega = 2\pi/1.6$, $k = 2\pi/0.6$ (a wave length of twice the length of the surface) and $H = 29.5$ would imply a reduced gravity of 0.5 m s^{-2}. This implies a density difference of 0.05 gr cm^{-3} between mixing layer and stratification. This is half the density difference between bottom and surface, so this difference is not expected between mixing layer and stratification. Measurements with a density probe are suggested for future experiments, to observe the mixing layer.
The rigid lid probably prevented the barotropic movement, but the rigid lid did not cover the whole surface (at a few location the rigid lid did not touch the walls), a little barotropic movement was still possible. So for future research inserting a better closing rigid lid is recommended.
Integrating b_x and b_z, with the correct constants of integration and boundary values, gives a

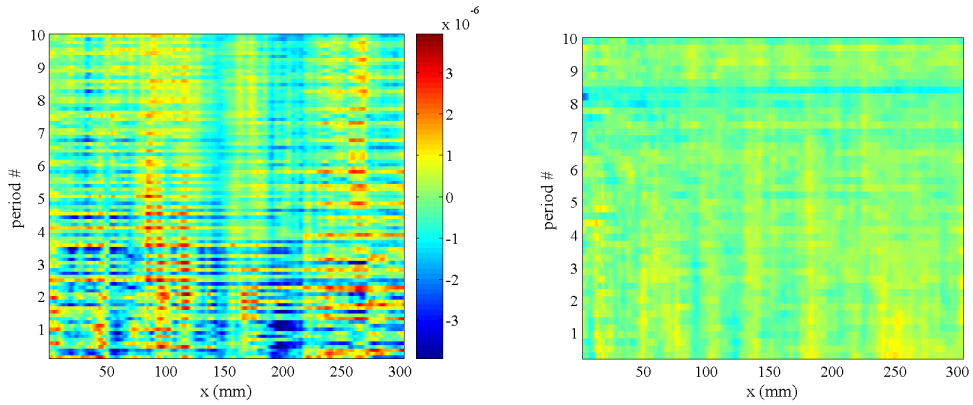

(a) "at_64" (b) "at_70"

Figure 5.9: Timeseries of a line near the surface of (a) "at_64" and (b) "at_70", the colour scale represents b_z since the surface movements are revealed by variations in the vertical gradient.

density field. Jeroen Hazewinkel performed this integration of the field of "at_150" and a strong sloshing with period $T = 5.1$ appears in the whole tank.

5.1.6 Waves generated by parametric excitation?

In Maas *et al.* (1997) the water movements in the attractor were of the order of cm's, the movements in "at_137" were only in the order of mm's. This means the forcing was just above the threshold of parametric instability, if the waves were generated by this mechanism. As in the previous section, timeseries were made along a line near the surface (of b_z) of "at_136" (forced harmonically) and "at_137" (forced sub-harmonically). The surface movements in "at_137" were very strong as shown in Fig. 5.11, where one period in both plots means 3.3 s. This suggests the internal waves in this experiment might be generated by this sloshing as well. The period of the sloshing is close to 3.3 s, so $2T$, as indicated in Fig. 5.12 (blue, the red line indicates b_z on the attractor), but not exactly, so the surface modes are probably not related to the generation of internal waves. Note that the sloshing in "at_136" was an order of magnitude smaller than in "at_137", see the colourbars in Fig. 5.11. The larger accelerations during "at_70" caused the excitation of stronger surface waves.
Since stage 2 of "at_137" was not captured very well, parametric excitation cannot be proved, since this can be recognised by an exponential growth of the amplitude (Benielli & Sommeria 1998; Lam & Maas 2007). Integrating the density fields of both experiments might show the absence of a barotropic movement during "at_137", which would give a stronger indication that the internal waves were excited by parametric instability.

5.2 The parabolic channel

The measurements of "at_107" are distorted by surface movements, so a harmonic analysis of the field of b_x was performed, on the first period of stage 2 (4.5 s, 24 fps). Fig. 5.14(a) shows the

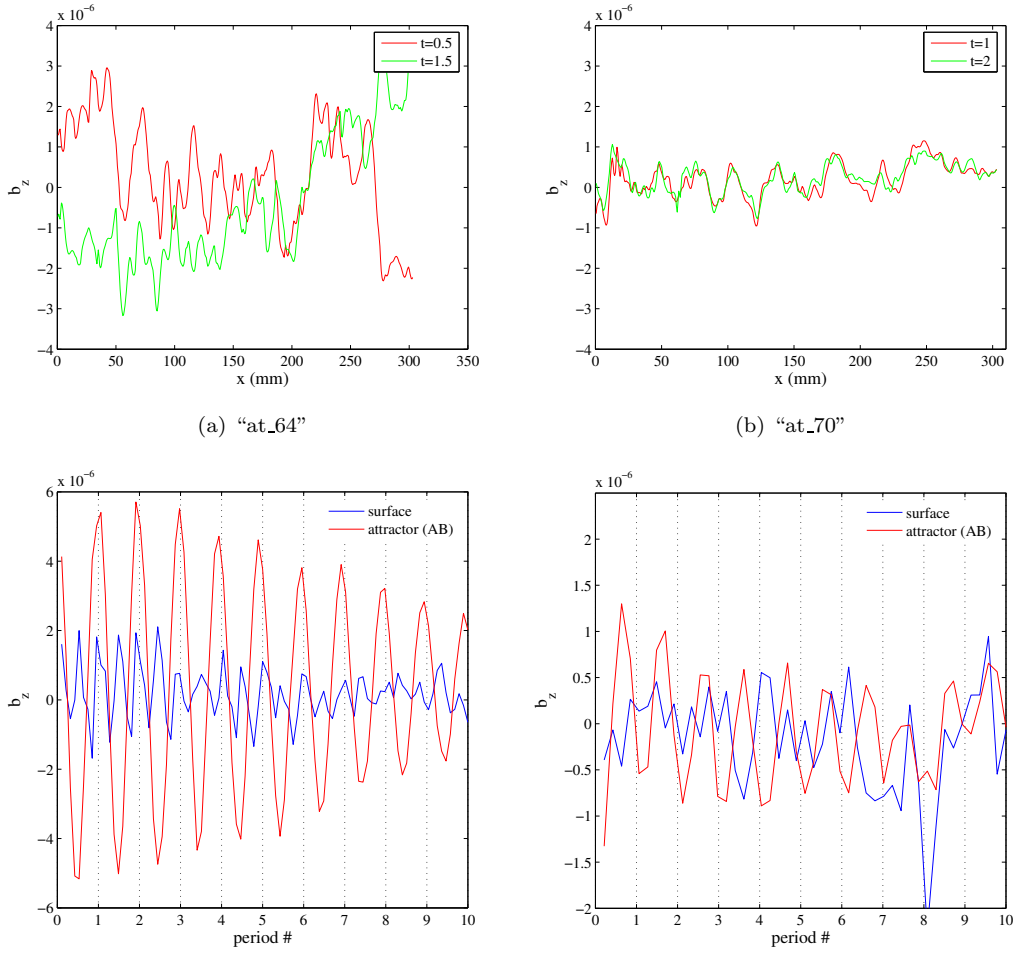

(a) "at_64"

(b) "at_70"

(c) "at_64"

(d) "at_70"

Figure 5.10: Upper panels: Values of b_z on a line near the surface in stage 2 of (a) "at_64" at $t = 0.5$ and $t = 1.5$ and (b) "at_70" at $t = 1$ and $t = 2$ in stage 2. Lower panels: The temporal evolution of a point at the left end of the surface (blue, at $X = 0$ mm) of (a) "at_64" and (b) "at_70". The evolution of b_z on the attractor (on the line AB, $X = 40$ mm) is indicated in red. It is clear that the red and blue lines do not have the same period.

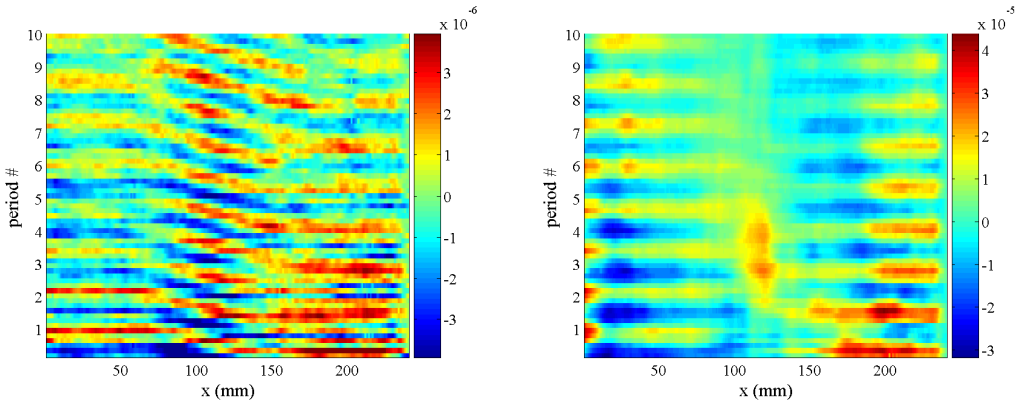

(a) (b)

Figure 5.11: Timeseries on a line near the surface of (a) "at_136" ($T = 3.3$ s) and (b) "at_137" ($T = 1.65$ s), the colour scale represents b_z since the surface movements are revealed by variations in the vertical gradient. The sloshing in "at_137" is an order of magnitude larger than in "at_136". In both plots one period indicates 3.3 s

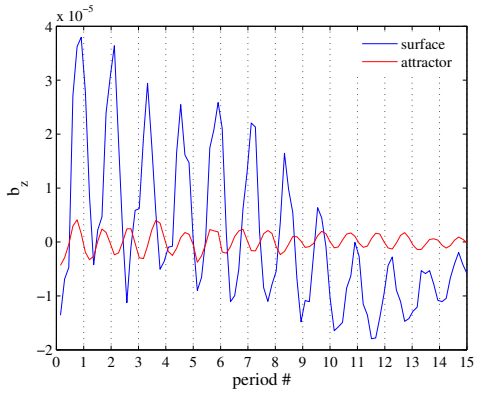

Figure 5.12: Variation of a point at the left side of the surface of "at_137" (blue). Here one period= $2T = 3.3$ s. The period of the surface sloshing is not equal to the period on the attractor (red) but: $5/4 \times 2T$ s.

amplitude of the signal with a period of $T = 4.5$. Black lines indicate the shape of the possible attractor. The analysis was distorted near the walls of the channel, this is visible by the deep red area at the left side and the noise at the right side, see Fig. 5.16(b). The lines have an angle of 50° with the vertical. From the period of forcing $T = 4.5$ s and $N = 2.2$ s^{-1}, the angle with the vertical of the internal wave beams is expected to be 53°. The reflection of the attractor did not occur at the surface, but about 5 cm below the surface. The reflection occurred at a strong mixing layer which is visualised by the tick horizontal lines in Fig. 4.7(b), which indicates the strong surface movements as well. A similar attractor structure was obtained from a numerical model by Drijfhout & Maas (2007).

5.2.1 The model used by Drijfhout and Maas

The three dimensional ocean model had 43 three layers, linearly stratified, a length of 1200 km, a width (at the surface) of 191.25 km and a total depth op 4300 m. They considered a parabolic channel with an open boundary at one side and a continental slope at the other end of the channel. The slope had a sinusoidal shape, with a width op 120 km. The minimum depth at the end of the slope was 50 m. A semidiurnal, barotropic forcing was applied to the open boundary, internal wave beams were generated at the continental slope. Diffusion, bottom stress and friction were included, but mixing of the layers was not.
As discussed in section 2.3, it is expected that internal waves in a 3D geometry can be trapped in a 2D plane, see Fig. 2.6(a). Fig. 5.15 shows this situation for the parabolic channel. One of the introduced rays propagates along the channel (around the critical slope, indicated by arrows in Fig. 5.13b), the other ray is trapped in a plane, as in Fig. 2.6(a). Drijfhout & Maas considered the system with and without rotation, but here the results without rotation are compared with our observations.

5.2.2 Qualitative comparison between model and observations

Fig. 5.13(b) shows the amplitude of the periodic interface displacements in a cross-channel plane, 900 km from the open boundary. Fig 5.14(b) shows the phase of these periodic movements. The cross sections show a trapped mode, indicated by the solid black lines in (b).
Besides the differences, Fig. 5.13(a) and (b) show similarities; the three “fingers” on both sides of the attractors, near the surface (model) or mixing layer (experiment), stronger amplitudes near the slopes (though reflections disturb the signal in (a)) and a point, near the middle of the bottom, with a local maximum in amplitude. An important difference is that the three points in the middle, where branches intersect, have a relative stronger amplitude in “at_107”.
The phase fields in Fig. 5.14(a) and (b) have similarities in their structure; in the middle, the phase near the bottom is opposite from that at the surface and the spatial phase variations are stronger near the sides. But the amphidronic points around the green dots ($\phi = -\pi$) in (c) are not present in (d).
It should be emphasised that the difference in scale between model and experiment is large (O(m) and O(100 km)) and that the parallax in the experiment was too large, i.e. the rays reaching the camera did not propagate parallel in the tank. The calculation of b_x and b_z are a result of the total path of a ray through the tank. But since these rays did not propagate parallel, the

measured density perturbations can not be allocated to a certain x and z. This introduces errors in the observations.
One other question which is open is whether the attractor observed in "at_107" was located in a plane (as in Drijfhout & Maas 2007) or existed along the length of the tank. This is an interesting question that can be answered by using two camera positions. Inserting a slope as introduced in Drijfhout & Maas (2007) in the parabolic channel would be interesting as well, in order to make a better comparison between the model and experiments.

5.3 The 3D rectangular tank

Fig. 4.9(b) reveals a signal which looks like an attractor. However, the parallax was too large to observe the fluid in a 3D tank, so the internal signal will not be analysed. Here I will discuss the error introduced by the parallax. To illustrate the influence of the reflections, the field of b_z is mixed with a figure of the square tank in Fig. 5.16(a). This clearly shows where the measurements are distorted by (reflection of light at) the walls of the tank. Since the tank has a length of 70 cm, the question rises from which point along this length a perturbation originates. This is hard to answer since **b** is a result of the path through the tank. The mixing layers, visible in Fig. 5.16(a) appear to emerge from the front of the tank, since they continue over the slope. But the main beam appears to be located more in the back of the tank, since it appears to reflect from the back of the bottom. These points illustrate the difficulties in analysing these results.

5.3.1 The path of rays through the 3D tank

We consider rays entering at the edges of the tank and reaching the camera. They travelled in the $x(z)$-direction a distance ΔX (ΔZ) through the tank, as indicated in Fig. 5.17. We assume the camera to be positioned exactly at $\frac{1}{2}B$, horizontal and vertical. In the z-direction $B = 20$ cm, approximately the depth of the water in the tank. In the x-direction $B = 60$ cm, the width of the tank, and $L = 70$ cm. We assume $\Delta X(\Delta Z) + S = \frac{1}{2}B$. S is indicated in Fig. 5.17. From Snell's law, we know:

$$\frac{n_g}{n_w}\sin\theta_1 = \frac{1}{n_g}\sin\theta_2$$

where the refractive index of glass, n_g, is 1.5 and of water, n_w, 1.33. The path length through the glass is ignored. From the information above, ΔX and ΔZ can be calculated: ΔX=3 cm and ΔZ=1 cm. This means that the perturbation, **b**, measured near the edges of a tank is a result of perturbations originating from an area of a few cm's around this point. For a tank of width $L = 10$ cm, as in the semi-2D tank, ΔX and ΔZ are smaller than one mm (depending on the depth and width of the tank). To reduce ΔX to values below cm's in the case of the big tanks, the distance between tank and camera has to be increased to about 20 m. Using mirrors might save space, though this might require new risk assessments.

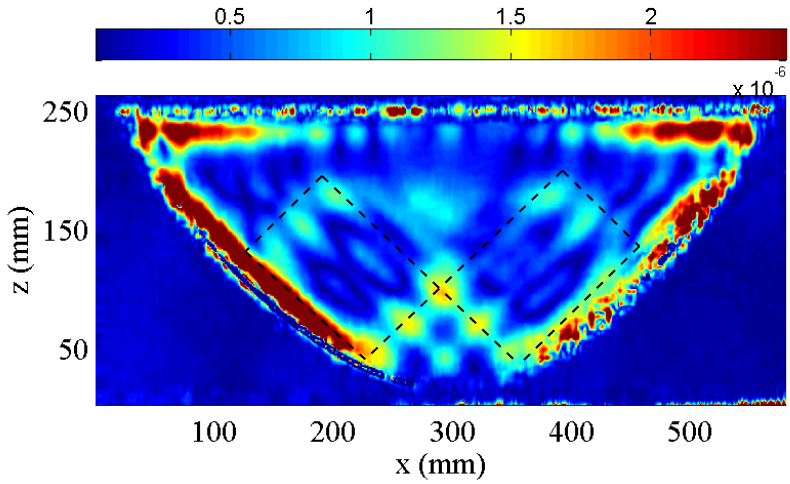

(a) Amplitude "at_107"

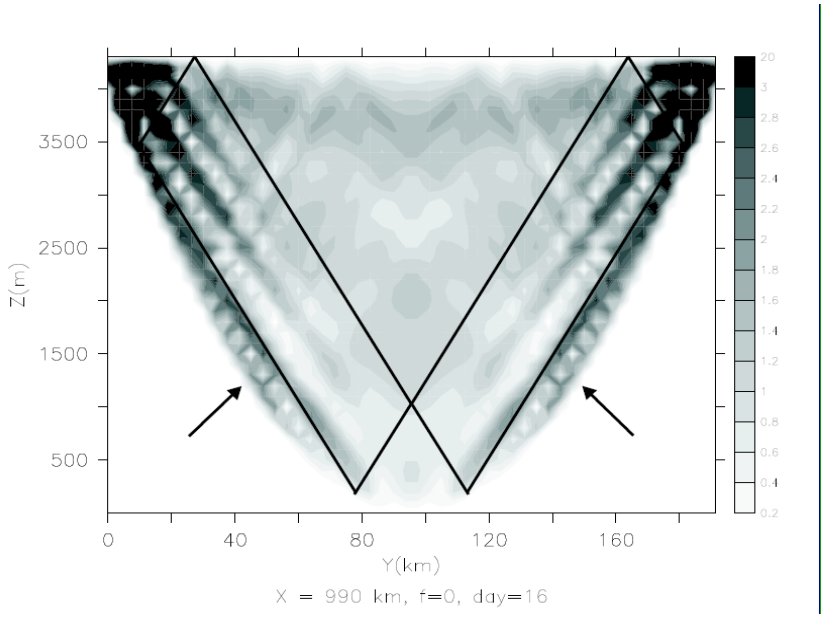

(b) Amplitude model

Figure 5.13: The amplitude of (a) of the periodic signal with $T = 4.5$ of b_x of "at_107", the dashed lines indicate the possible attractor and (b) the semidiurnal amplitude in the model of Drijfhout & Maas (2007), the solid lines indicate the attractor.

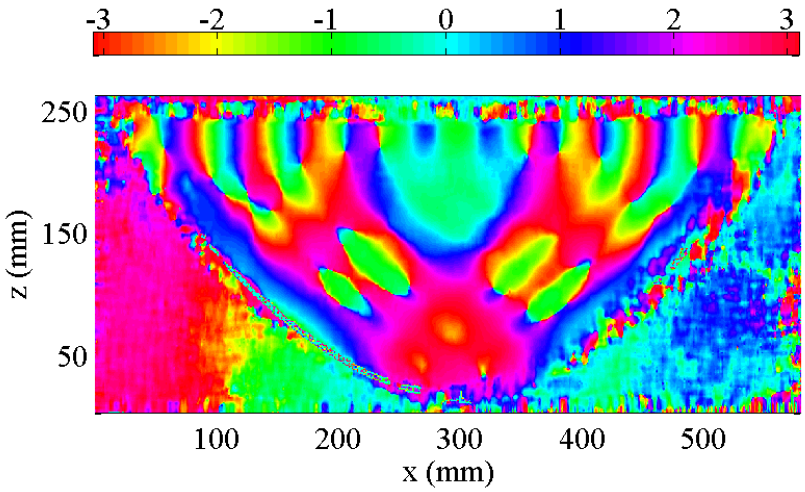

(a) Phase "at_107"

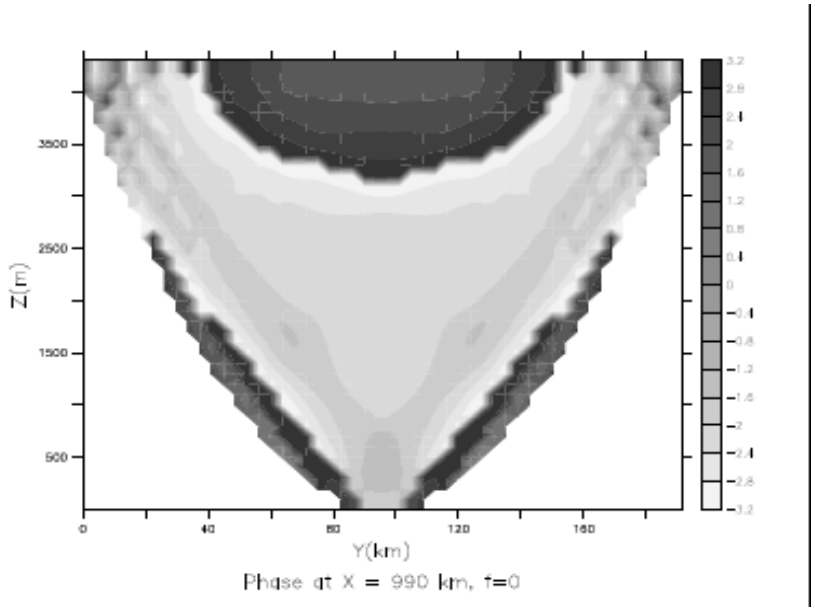

(b) Phase model

Figure 5.14: The phase of (a) the periodic signal with $T = 4.5$ of b_x of "at_107" and (b) the semidiurnal signal in the model of Drijfhout & Maas (2007).

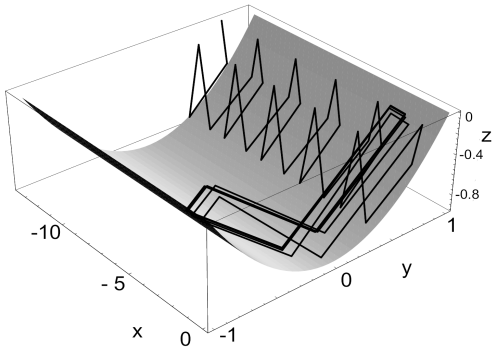

Figure 5.15: Two rays introduced at $x = 0$, $y = 0.75$ at the surface. One is directed down-channel, this one propagates towards the other end of the channel. The other ray partly propagates in the cross-channel direction and is trapped in a plane. Figure from Drijfhout & Maas (2007).

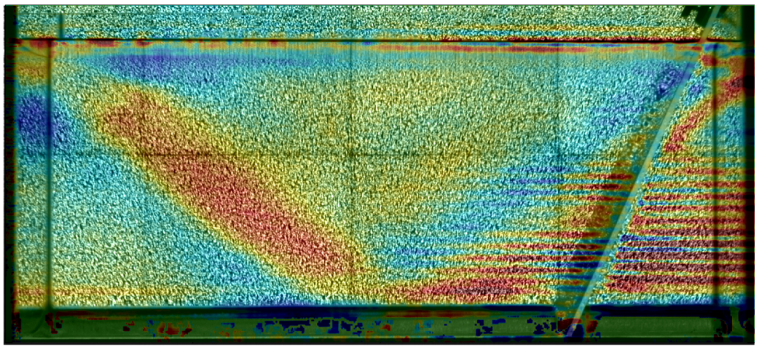

(a)

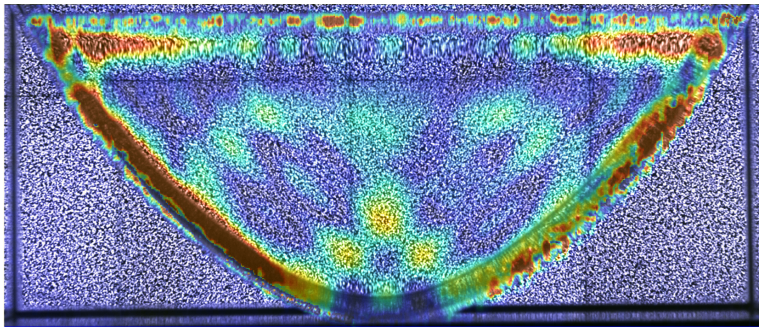

(b)

Figure 5.16: (a) b_z of "at_45", but with a picture of the tank mixed in it. Now the locations where reflection distorts the result can be seen (b) is Fig. 5.13(a), with a picture of the tank mixed in it.

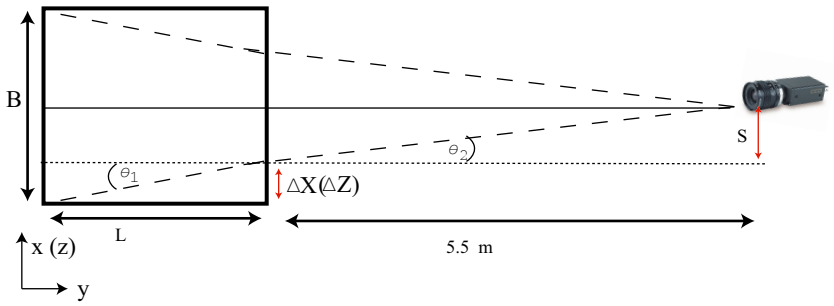

Figure 5.17: Rays entering around the edges of the tank, travel a distance ΔX (ΔZ) in the $x(z)$-direction.

5.4 Concluding remarks

The experiments resulted in new insights in the behaviour of internal waves. It should be kept in mind that in the analysis above the fields of b_x and b_z were used, not the real density fields. The density field (obtained by integrating b_x and b_z), reveals the barotropic movements in the whole tank.

We initially aimed at subharmonic generation of internal waves, parametrically excited, but the platform allowed harmonic generation over a much larger frequency and amplitude range. This has an advantage: Since the horizontal movements were small, the amplitude of the internal waves was small as well. This means hardly any mixing, caused by the movements in the attractors, took place. In the experiment by Maas *et al.* (1997), the amplitudes in the attractor were larger (cm's) and mixing took place. Benielli & Sommeria (1998) also observed wave breaking of (standing) internal waves excited by parametric excitation. If the mixing is too strong, experiments can not be repeated with the same stratification. In our case, repeating the experiments in the same stratification was no problem (up to ten times), though existing mixing layers, were slightly amplified during the experiments.

In our range of forcing a linear relation between response and forcing was found, and in future experiments it might be interesting to study the forcing when this linear relation breaks. This is much easier in a setting with a horizontally oscillating tank, since very small amplitudes (mm's) are required to obtain the same barotropic movements as we obtained with the vertical oscillation. Smaller horizontal oscillation might reduce the smaller surface movements in the larger tank as well, since they appear to be induced by the vertical accelerations.

How can we quantify the perturbations in **b**? Jeroen Hazewinkel performed an experiment, using PIV (Hazewinkel *et al.* 2007). In this method one uses reflecting particles with different buoyancies, distributed in such a way that the particles are floating throughout the whole stratification. If a light source is directed on the particles, their movements can be detected by a camera. Digiflow can correlate the particles in different frames and deduct the movement and velocity of such a particle. In the experiment velocities in the attractor around 0.5 mm/s were observed, see Fig. 5.18. With an oscillation period of 5 s, this velocity is associated with a particle displacement of 0.4 mm.

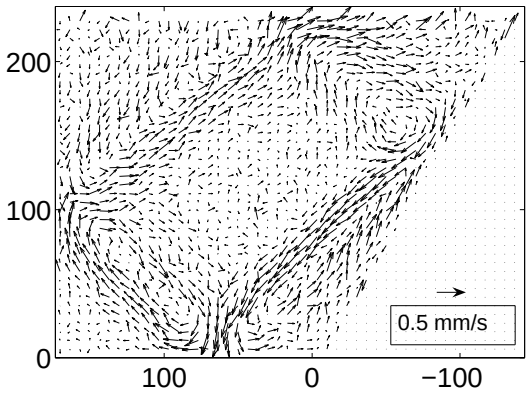

Figure 5.18: Velocity field, observed with PIV, in an attractor. From (Hazewinkel *et al.* 2007).

I conclude with some suggestions for future experiments (some out of the blue, some distilled from the discussed experiments):

- The effect of a bottom topography can be studied by introducing a rough bottom, the volume of the bottom variations should be small in order to preserve a linear stratification.
- If a horizontal oscillation is used, it might be an option to oscillate the tank along the y-axis (as defined in Fig. 3.4). Since the amplitude of the oscillation is only a few mm's, they can be analysed with the same reference image, since this introduces only a small error. This allows a more continuous capturing during stage 1.
- The attractor with the highest period, mentioned in this thesis, was a (2,1)-attractor. Can an (3,1)-attractor be observed as well?
- The relation between forcing and response appeared to be linear, in the domain we studied. A horizontal oscillation is probably able to supply a strong harmonic forcing, this allows the study of this relation in a larger amplitude range. When does this linear relation break down and how does this influence the shape of the wave number spectrum?
- In section 5.1.4 it is suggested that the shape of the wave number spectra of internal wave attractors are partly determined by the length of the attractors. A series of experiments with (1,1)-attractors with significant length differences could supply more proof of this. The behaviour of the energy spectrum can be tested with additional PIV measurements.

CHAPTER 6

Conclusions

In this chapter a summary of the conclusions from chapter 4 and 5 is given.

The platform was not able to apply sufficient forcing to excite waves by parametric instability, as explained in section 3.2.2. A few attempts to generate waves sub-harmonically have been made, one experiment is described in section 4.2.4, in which an attractor was observed. This experiment was analysed in section 5.1.6, from which we concluded that parametric excitation can neither be proved nor ruled out since the growth of the attractor could not be analysed. Harmonic generation was supported in the set-up, probably caused by small horizontal movements, which accompanied the vertical oscillation. Section 5.1.1 showed that the harmonic generation resulted in a linear growth of the amplitudes of the attractors, until a steady state was reached after about 20 periods. The steady state amplitudes were small compared to the amplitudes in the attractor described in Maas *et al.* (1997). This is because the barotropic forcing was small, resulting in a weak baroclinic signal. The small amplitudes prevented mixing and allowed multiple experiments in the same stratification.

In section 4.2.1, Fig. 4.2, we observed an increase in the forcing amplitude being accompanied by a stronger response in the attractor. In section 5.1.1, Fig. 5.3, we found that this relation was linear.

The peak wave number in the attractor was not influenced by the forcing strength, at least not in the range we studied, as shown in section 5.1.1, Fig. 5.4(h). The spectral evolution during the build up and decay of an attractor appeared to depend on the time it takes for a wave with a certain wave number to cycle the attractor. In the steady state a balance existed between production of wave numbers (produced by barotropic-baroclinic conversion and focusing at the slope) and viscous damping. The dissipation was stronger at larger wave numbers since they travel with smaller group velocities and are associated with greater lateral shear. A smaller group velocity implies that viscosity has more time to act on a wave.

Section 4.2.2, Fig. 4.4, revealed that the shape and existence of an attractor can be predicted by the inviscid description, as shown in Fig. 4.1. The shape and existence of an attractor depends on the parameters (τ and d) describing the geometry of the fluid domain, stratification and wave frequency.

Fig. 5.7 revealed that the peak wave number does depend on the shape of the attractor and hence the forcing *frequency*. We suggested in sections 5.1.3 and 5.1.4, that the wave number spectrum

depends on the length of an attractor, as explained in more detail in Appendix B.
In the parabolic channel an attractor was observed and cleared-up with harmonic analysis as shown in Fig. 5.13(a). Whether this attractor existed throughout the length of the tank or in a plane cannot be answered since only one camera position was used. For future experiments, inserting a slope in the parabolic channel would give an opportunity to compare the model of Drijfhout & Maas (2007) with experiments in more detail.
We suggested in section 4.5 to use a horizontal oscillation as a forcing mechanism. In the set-up we used, the amplitude of the horizontal motions were unknown. Since a small barotropic forcing proved itself to be sufficient for the experiments, a horizontal oscillation is preferable, since the forcing is more predictable and allows a larger range of forcing. An important difference between the two forcing mechanisms is that a horizontal oscillation introduces an orientation in the experiment and parametric excitation not.
In the experiments with the wide 3D rectangular tank, with one sloping wall, oblique signals were observed, as shown in section 4.4, but the tank was too close to the camera, which introduced errors in the measurements (section 5.3). Increasing the distance between camera and tank to about 20 m will give more accurate results, as this reduces the parallax.

We can conclude that the experiments resulted in new insights in the behaviour of internal wave attractors, for different geometries and different amplitudes and frequencies of forcing. The effect of viscosity could be studied very precisely and might be relevant to research outside the scope of attractors. Furthermore, a more detailed experimental study of attractors in 3D is possible with the current set-up, after applying the suggested adjustments. Not much is known about internal wave attractors in 3D and experimental knowledge will be helpful in the search for a mathematical description of these patterns.

APPENDIX A

Overview of the experiments

Snapshots of all the experiments performed in November and December 2006 in Cambridge are shown here. The first frame in stage 2 is shown. The figures show b_z or b_x, depending on which field revealed the best information (the least amount of (thermal) noise).
Below the figures the experimental parameters are given as:

"at_xxx"; T= (seconds); A= (cm's); N= (rad/s); H= (cm's)

If a rigid lid was used, "rigid lid" indicates on which side the rigid lid was placed (side "a" (left) or "b"(right)).
Most of the figures are from experiments with the semi-2D tank unless "3D" is indicated, which means the big rectangular tank, or "para", which indicates the parabolic channel.
If "parametric" is displayed, this means a subharmonic forcing was applied (with $T < 2\pi/N$) in order to invoke parametric instability. The colour scale is a qualitative indication. A red cross indicates a failed and deleted experiment.

The values of τ and d of all the experiments in a trapezoidal basin are indicated in Fig. A.1.

Appendix A: Overview of the experiments

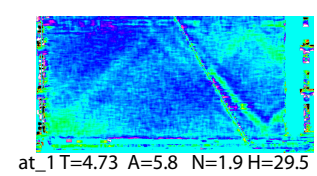
at_1 T=4.73 A=5.8 N=1.9 H=29.5

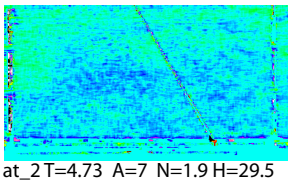
at_2 T=4.73 A=7 N=1.9 H=29.5

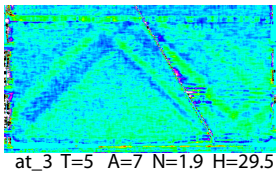
at_3 T=5 A=7 N=1.9 H=29.5

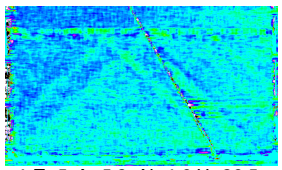
at_4 T=5 A=5.8 N=1.9 H=29.5

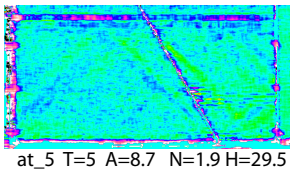
at_5 T=5 A=8.7 N=1.9 H=29.5

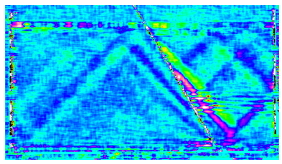
at_6 T=4.74 A=8.7 N=1.9 H=29.5

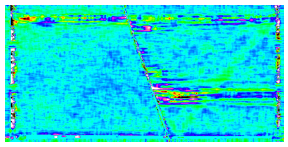
at_7 T=4.74 A=7 N=1.8 H=29

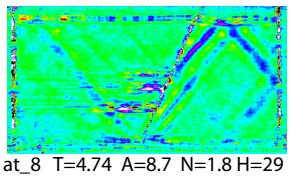
at_8 T=4.74 A=8.7 N=1.8 H=29

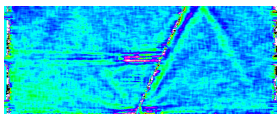
at_9 T=4.2 A=8.7 N=1.7 H=29

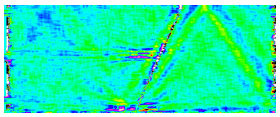
at_10 T=4.45 A=8.7 N=1.7 H=29

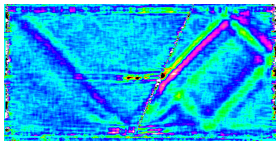
at_11 T=5.1 A=8.7 N=1.7 H=29

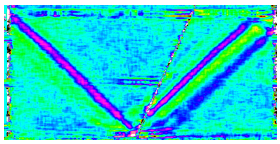
at_12 T=5.35 A=8.7 N=1.7 H=29

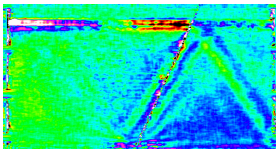
at_13 T=4.45 A=8.7 N=1.7 H=29

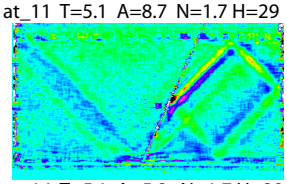
at_14 T=5.1 A=5.8 N=1.7 H=29

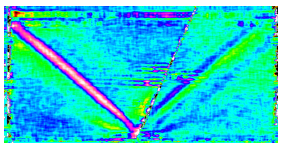
at_15 T=5.7 A=8.7 N=1.7 H=29

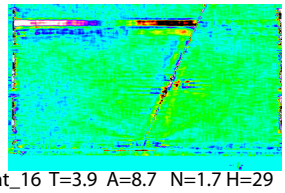
at_16 T=3.9 A=8.7 N=1.7 H=29

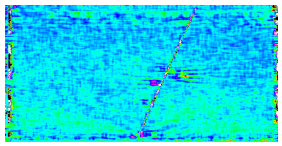
at_17 T=2.55 A=8.7 N=1.7 H=29

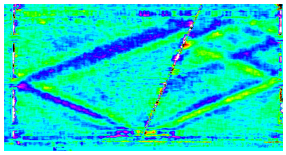
at_18 T=10.2 A=10.4 N=1.7 H=29

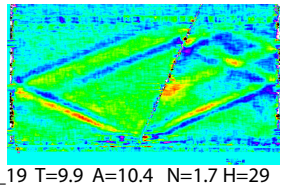
at_19 T=9.9 A=10.4 N=1.7 H=29

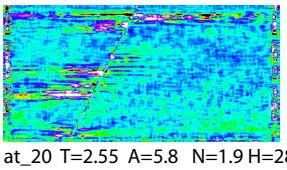
at_20 T=2.55 A=5.8 N=1.9 H=28.5

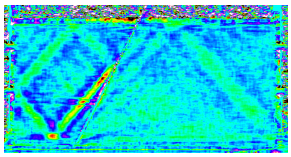
at_21 T=4.7 A=4.1 N=1.9 H=28.5

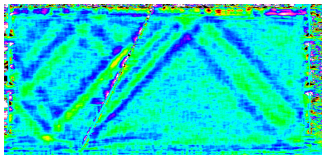
at_22 T=4.8 A=4.1 N=1.9 H=29

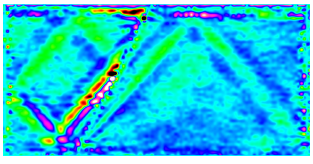
at_23 T=4.7 A=4.1 N=1.9 H=29

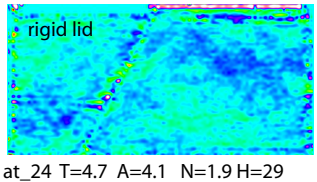

at_24 T=4.7 A=4.1 N=1.9 H=29

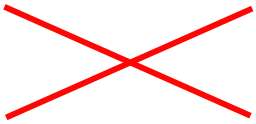

at_25 T=4.7 A=4.1 N=1.9 H=28.5

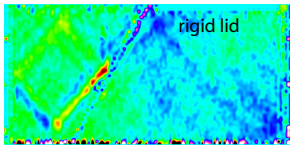

at_26 T=4.7 A=4.1 N=1.9 H=28.5

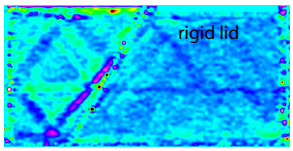

at_27 T=4.7 A=4.1 N=1.9 H=28.5

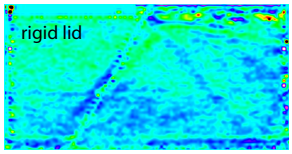

at_28 T=4.7 A=4.1 N=1.9 H=28.5

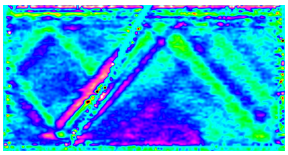

at_29 T=4.7 A=4.1 N=1.9 H=28.5

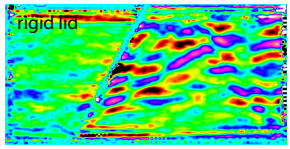

at_30 T=4.7 A=4.1 N=1.9 H=28.5

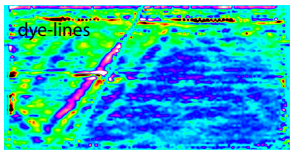

at_31 T=4.1 A=4.1 N=1.8 H=28.5

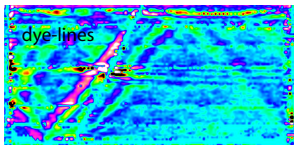

at_32 T=4.1 A=8.7 N=1.8 H=28.5

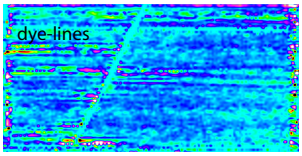

at_33 T=3.7 A=8.7 N=1.8 H=28.5

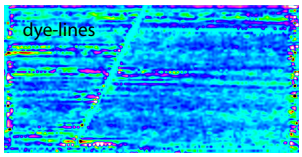

at_34 T=4.5 A=10.4 N=1.8 H=28.5

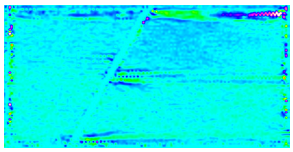

at_35 T=4.1 A=9.9 N=1.1 H=28

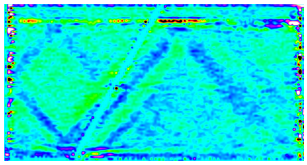

at_36 T=8.2 A=9.9 N=1.1 H=28

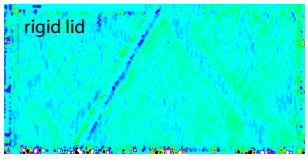

at_37 T=8.2 A=9.9 N=1.1 H=28

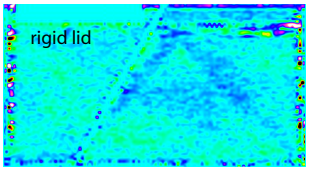

at_38 T=8.2 A=9.9 N=1.1 H=28

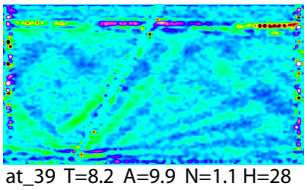

at_39 T=8.2 A=9.9 N=1.1 H=28

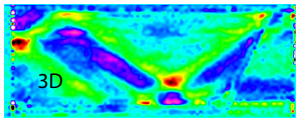

at_40 T=4.7 A=4.1 N=2.2 H=25

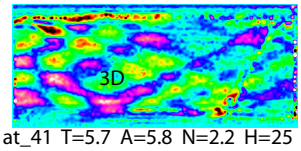

at_41 T=5.7 A=5.8 N=2.2 H=25

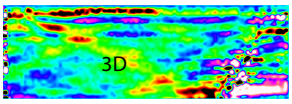

at_42 T=5.85 A=5.8 N=2.2 H=25

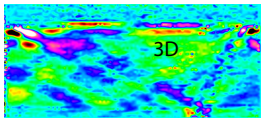

at_43 T=5.85 A=5.8 N=2.2 H=25

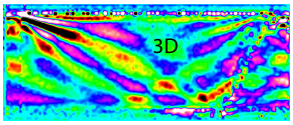

at_44 T=5.85 A=5.8 N=2.2 H=25

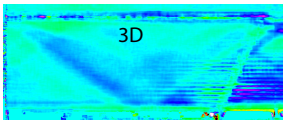

at_45 T=4.7 A=5.8 N=2.2 H=25

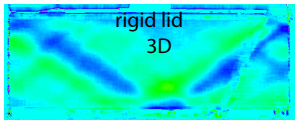

at_46 T=4.7 A=5.8 N=2.2 H=25

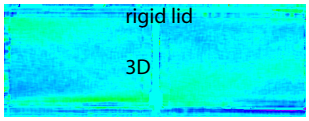

at_47 T=4.7 A=5.8 N=2.2 H=25

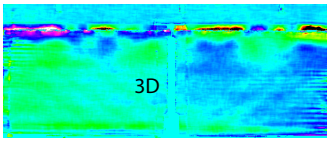

at_48 T=4.7 A=5.8 N=2.2 H=25

Appendix A: Overview of the experiments

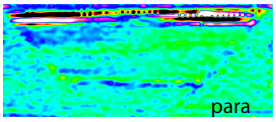

at_49 T=5 A=4.6 N=? H=?

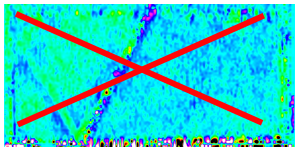
at_50

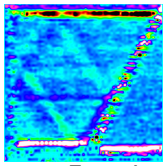
at_51 T=4.7 A=5.81 N=1.7 H=29

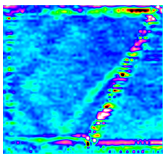
at_52 T=4.9 A=5.8 N=1.7 H=29

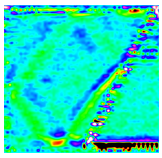
at_53 T=4.9 A=5.8 N=1.7 H=29

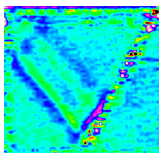
at_54 T=4.9 A=5.8 N=1.7 H=29

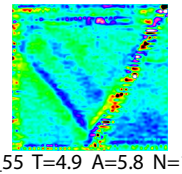
at_55 T=4.9 A=5.8 N=1.7 H=29

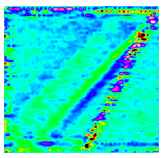
at_56 T=4.9 A=5.8 N=1.8 H=29.5

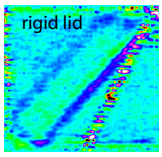

at_57 T=4.9 A=5.8 N=1.8 H=29.5

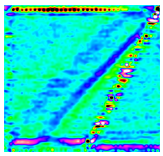
at_58 T=4.9 A=5.8 N=1.8 H=29.5

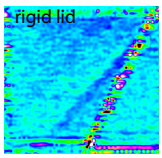

at_59 T=4.9 A=5.8 N=1.8 H=29.5

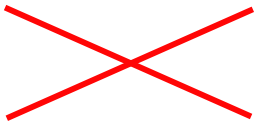
at_60

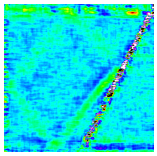
at_61 T=4.7 A=3.5 N=1.8 H=29.5

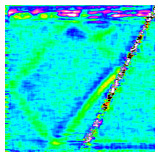
at_62 T=4.7 A=4.6 N=1.8 H=29.5

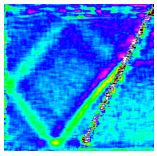
at_63 T=5.8 A=4.6 N=1.8 H=29.5

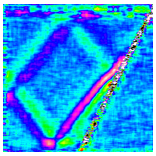
at_64 T=4.7 A=7.0 N=1.8 H=29.5

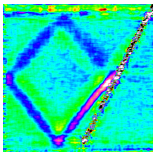
at_65 T=4.7 A=7.0 N=1.8 H=29.5

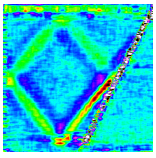
at_66 T=4.7 A=8.1 N=1.8 H=29.5

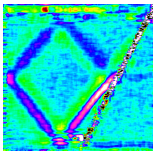
at_67 T=4.7 A=9.3 N=1.8 H=29.5

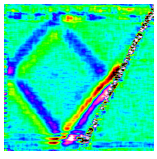
at_68 T=4.7 A=10.4 N=1.8 H=29.5

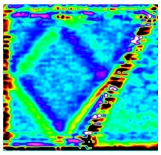
at_69 T=4.7 A=7 N=1.8 H=29.5

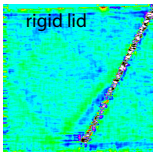

at_70 T=4.7 A=7.0 N=1.8 H=29.5

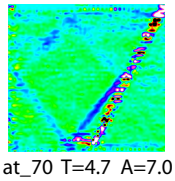
at_70 T=4.7 A=7.0 N=1.8 H=29.5

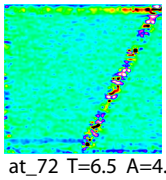
at_72 T=6.5 A=4.1 N=1.8 H=29.5

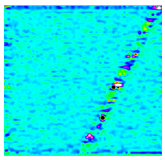

at_73 T=6 A=4.1 N=1.8 H=29.5

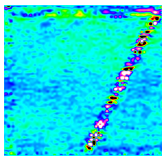

at_74 T=5.5 A=4.1 N=1.8 H=29.5

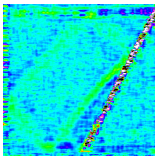

at_75 T=4.7 A=4.1 N=1.8 H=29.5

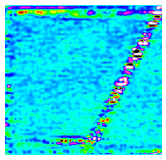

at_76 T=6 A=7 N=1.8 H=29.5

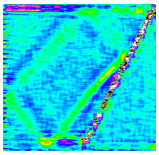

at_77 T=4.7 A=7 N=1.8 H=29.5

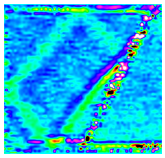

at_78 T=4.7 A=7 N=1.8 H=29.5

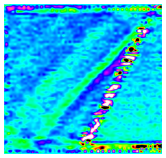

at_79 T=4.9 A=7 N=1.8 H=29.5

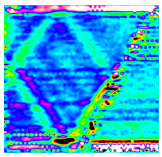

at_80 T=4.5 A=7 N=1.8 H=29.5

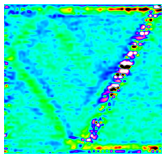

at_81 T=4.3 A=7 N=1.8 H=29.5

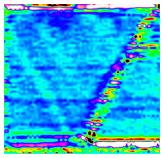

at_82 T=4.2 A=7 N=1.8 H=29.5

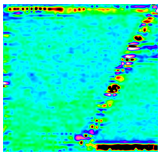

at_83 T=4.1 A=7 N=1.8 H=29.5

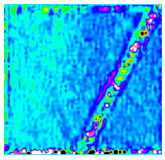

at_84 T=4 A=7 N=1.8 H=29.5

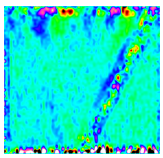

at_85 T=3.9 A=7 N=1.8 H=29.5

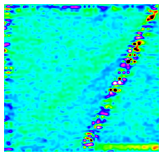

at_86 T=5.1 A=7 N=1.8 H=29.5

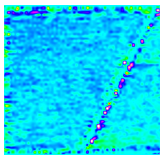

at_87 T=3.8 A=7 N=1.8 H=29.5

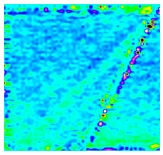

at_88 T=5.2 A=10.4 N=1.8 H=29.5

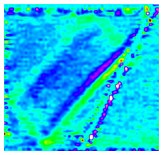

at_89 T=4.9 A=9.3 N=1.8 H=29.5

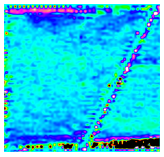

at_90 T=6.0 A=10.4 N=1.8 H=29.5

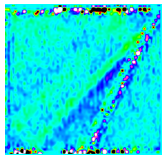

at_91 T=6.1 A=7 N=1.4 H=29.5

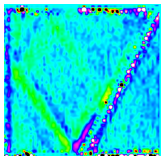

at_92 T=5.4 A=7 N=1.4 H=29.5

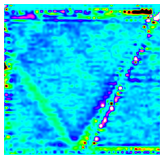

at_93 T=5.4 A=7 N=1.4 H=29.5

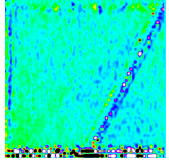

at_94 T=8.8 A=7 N=1.0 H=29.5

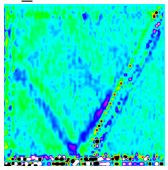

at_95 T=7.6 A=7 N=1.0 H=29.5

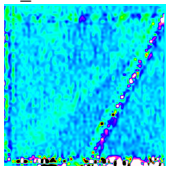

at_96 T=8.8 A=10.4 N=1.0 H=29.5

Appendix A: Overview of the experiments

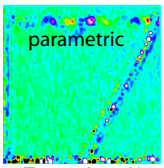

at_97 T=4.4 A=7 N=1.0 H=29.5

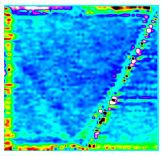

at_98 T=7.6 A=7 N=1.0 H=29.5

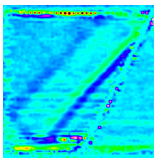

at_99 T=3.8 A=7 N=2.3 H=29.5

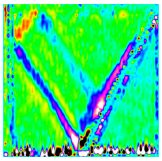

at_100 T=3.3 A=7 N=2.3 H=29.5

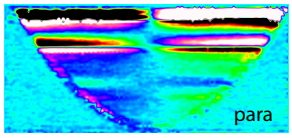

at_101 T=3 A=4.6 N=2.3 H=25

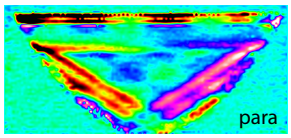

at_102 T=6 A=7 N=2.3 H=25

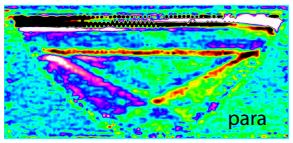

at_103 T=7 A=7 N=2.3 H=25

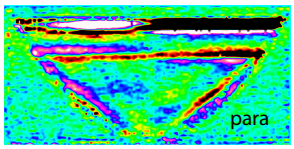

at_103 T=7 A=7 N=2.3 H=25

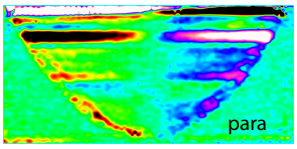

at_105 T=5 .5 A=7 N=2.3 H=25

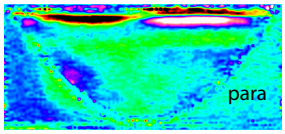

at_106 T=4.5 A=7 N=2.3 H=25

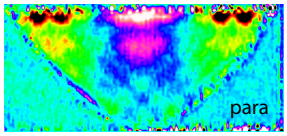

at_107 T=4.5 A=10.4 N=2.3 H=25

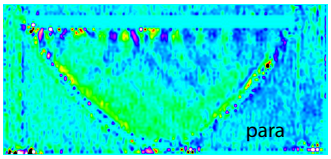

at_108 T=4.5 A=10.4 N=2.3 H=25

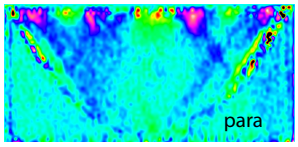

at_109 T=4.5 A=10.4 N=1.7 H=26

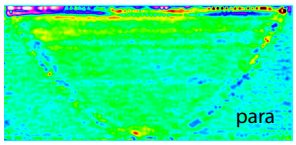

at_110 T=4.5 A=7 N=1.7 H=26

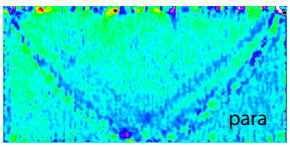

at_111 T=6 A=7 N=1.7 H=26

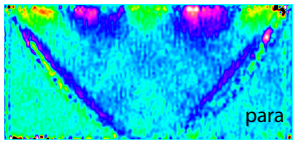

at_112 T=5 A=7 N=1.7 H=26

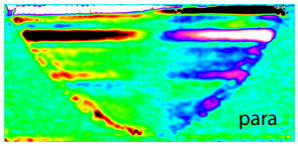

at_113 T=5 A=8.7 N=1.7 H=26

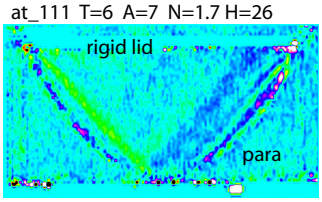

at_114 T=5 A=8.7 N=1.7 H=26

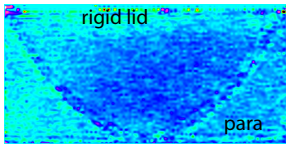

at_115 T=2.5 A=5.8 N=1.7 H=26

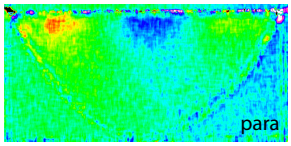

at_116 T=2.5 A=5.8 N=1.7 H=26

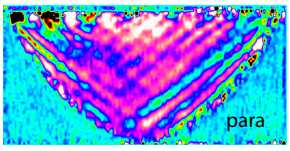

at_117 T=3 A=8.7 N=1.7 H=26

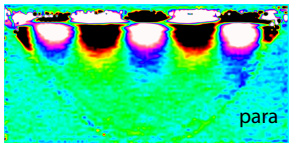

at_118 T=2.8 A=9.6 N=1.7 H=26

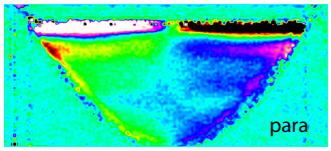

at_119 T=5 A=9.6 N=1.7 H=26

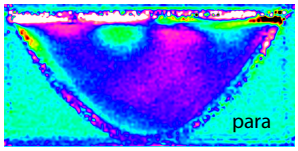

at_120 T=5 A=11 N=1.7 H=26

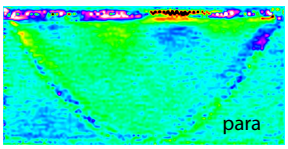

at_121 T=5 A=5.8 N=1.7 H=26

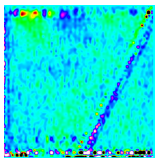

at_122 T=2.1 A=5.8 N=2.0 H=29.5

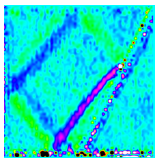

at_123 T=4.2 A=5.8 N=2.0 H=29.5

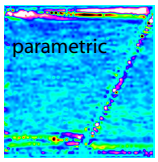

at_124 T=2.5 A=7.8 N=2.0 H=29.5

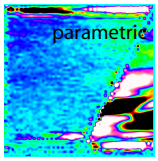

at_125 T=1.9 A=5.2 N=2.0 H=29.5

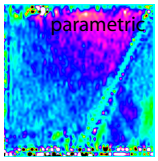

at_126 T=1.9 A=5.8 N=2.0 H=29.5

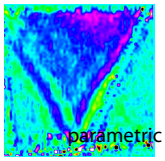

at_127 T=1.9 A=5.8 N=2.0 H=29.5

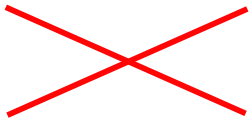

at_128

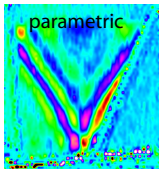

at_129 T=1.9 A=5.8 N=2.0 H=29.5

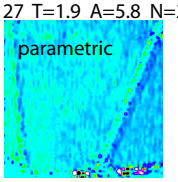

at_130 T=1.95 A=5.8 N=2.0 H=29.5

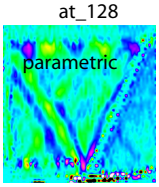

at_131 T=1.85 A=5.8 N=2.0 H=29.5

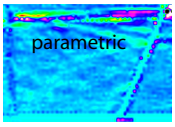

at_132 T=1.8 A=5.8 N=2.0 H=29.5

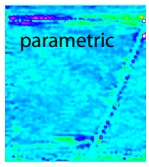

at_133 T=1.83 A=5.8 N=2.0 H=29.5

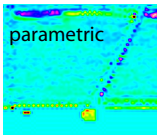

at_134 T=1.5 A=3.2 N=3 H=19

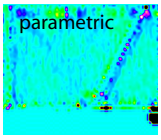

at_135 T=1.5 A=3.2 N=3 H=19

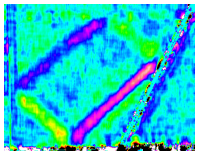

at_136 T=3.3 A=5.8 N=3 H=19

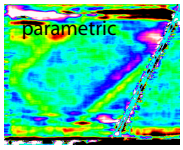

at_137 T=1.65 A=5.2 N=3 H=19

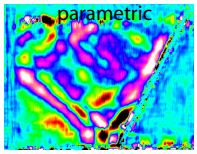

at_138 T=1.65 A=5.2 N=3 H=19

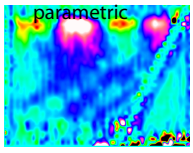

at_139 T=1.75 A=5.2 N=3 H=19

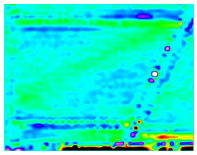

at_140 T=5 A=8.1 N=3 H=19

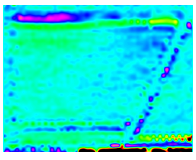

at_141 T=4 A=8.1 N=3 H=19

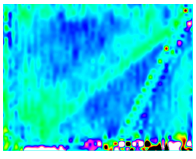

at_142 T=3.5 A=8.1 N=3 H=19

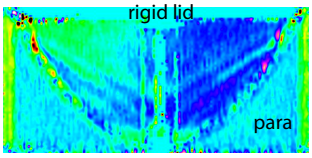

at_143 T=4.5 A=10.4 N=2.3 H=25

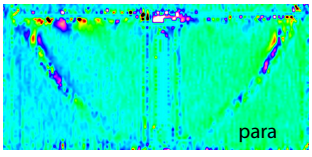

at_144 T=4.5 A=10.4 N=2.3 H=25

Appendix A: Overview of the experiments

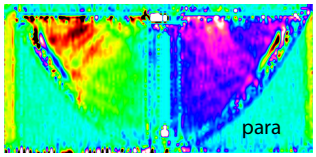

at_145 T=4.3 A=12.8 N=2.3 H=25

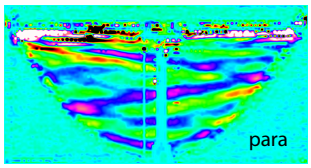

at_146 T=2.3 A=5.8 N=2.3 H=25

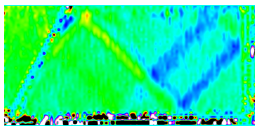

at_147 T=3.1 A=5.8 N=2.9 H=19.5

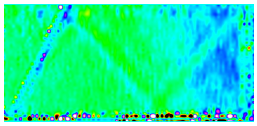

at_148 T=3 A=5.8 N=2.9 H=19.5

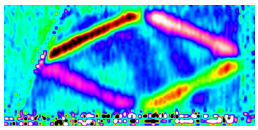

at_149 T=5.1 A=5.8 N=2.9 H=19.5

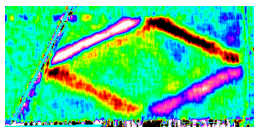

at_150 T=5.1 A=5.8 N=2.9 H=19.5

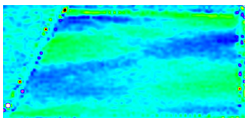

at_151 T=12.1 A=10.4 N=2.9 H=19.5

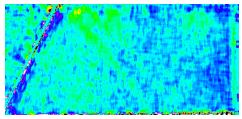

at_152 T=2.9 A=5.8 N=2.9 H=19.5

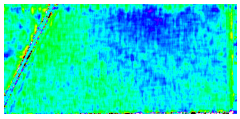

at_153 T=4 A=5.8 N=2.9 H=19.5

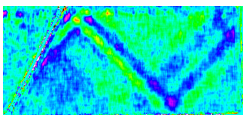

at_154 T=3.1 A=8.7 N=2.9 H=19.5

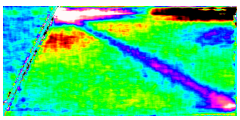

at_155 T=4.7 A=10.4 N=2.9 H=19.5

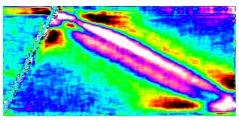

at_156 T=4.9 A=10.4 N=2.9 H=19.5

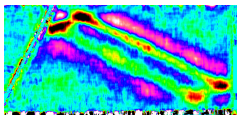

at_157 T=5 A=10.4 N=2.9 H=19.5

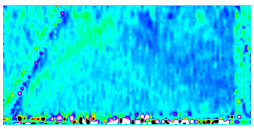

at_158 T=3.5 A=10.4 N=2.9 H=19.5

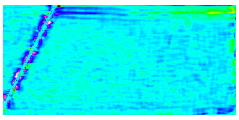

at_159 T=3.5 A=8.7 N=2.9 H=19.5

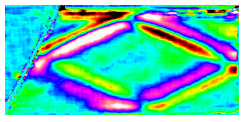

at_160 T=5.3 A=8.7 N=2.9 H=19.5

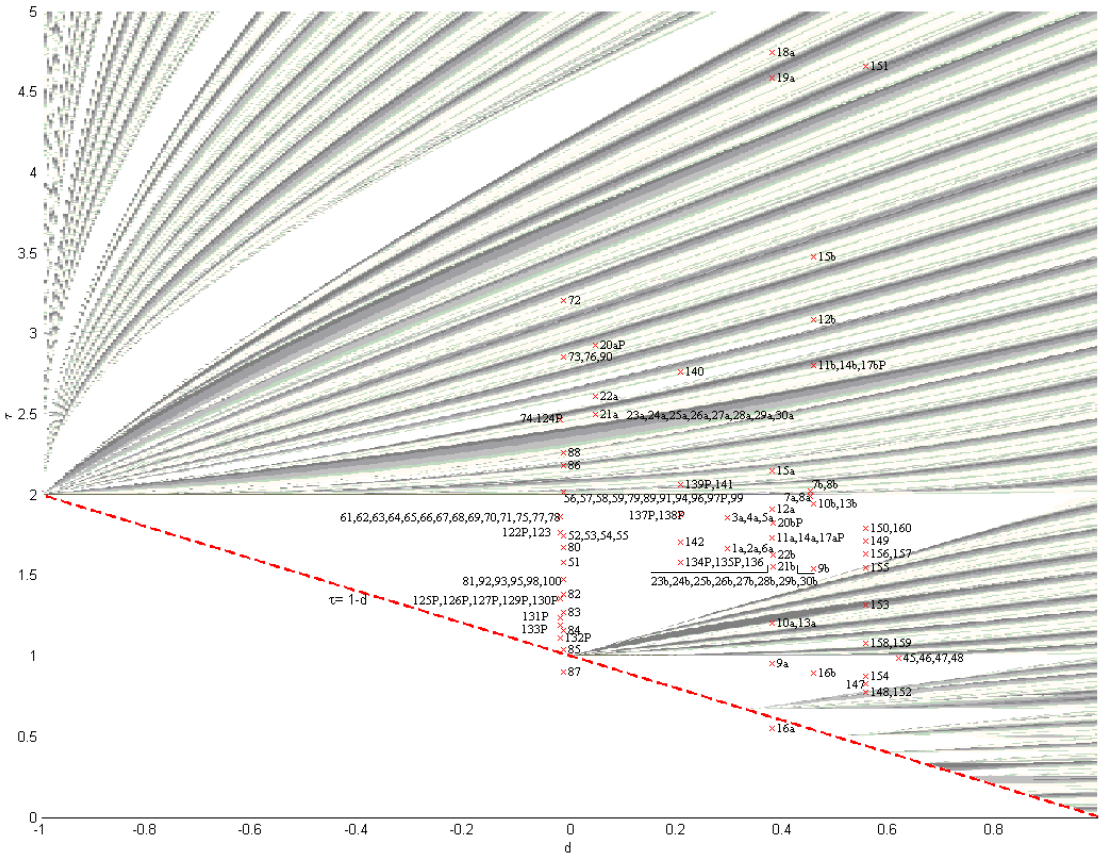

Figure A.1: Same as Fig. 4.1, but now all the experiments performed in a trapezoidal basin are indicated. Again the numbers refer to the labels of the experiments, so "61" refers to "at_61". "a" ("b") refers to side "a" ("b"), because before the slope was glued into the basin, the experiments were performed simultaneously in both sides of the basin. "P" refers to parametric excitation. Some τ's were very close to each other. When their difference was < 0.03, they were indicated with the same marker, in order to keep the diagram readable.

APPENDIX B

Growth, equilibrium and decay of an internal wave attractor

Paper submitted to the Journal of Fluid Mechanics (2007).

Under consideration for publication in J. Fluid Mech.

Observations on the wave number spectrum and evolution of an internal wave attractor in a two-dimensional domain

By Jeroen Hazewinkel [1,2], Pieter van Breevoort [3], Stuart B. Dalziel [2], Leo R.M. Maas [1,3]

[1] Royal Netherlands Institute for Sea Research, P.O. Box 59, 1790 AB Texel, The Netherlands
[2] Department of Applied Mathematics and Theoretical Physics, University of Cambridge, Wilberforce Road, Cambridge CB3 0WA, UK
[3] Institute for Marine and Atmospheric research Utrecht, University Utrecht, Princetonplein 5, 3584 CC Utrecht, The Netherlands

(Received 13 August 2007)

Reflecting internal gravity waves in a stratified fluid preserve their frequency and thus their angle with the gravitational direction. At boundaries that are neither horizontal nor vertical, this leads to a focusing or defocusing of the waves. Previous theoretical and experimental work has demonstrated how this can lead to internal wave energy being focused onto 'wave attractors' in relatively simple geometries. We present new experimental and theoretical results on the dynamics of wave attractors in a semi two-dimensional trapezoidal basin. In particular, we demonstrate how a basin-scale mode forced by simple mechanical excitation develops an equilibrium spectrum. We find a balance between focusing of the basin-scale internal wave by reflection from a single sloping boundary and viscous dissipation of the waves with higher wave numbers. Theoretical predictions using a simple ray-tracing technique are found to agree well with direct experimental observations of the waves. With this we explain the observed behaviour of the wave attractor during the initial development, steady forcing, and decay of the wave field after the forcing is terminated. We also predict the spatial scale of the wave attractor.

1. Introduction

Understanding the behaviour of linear internal waves in bounded geometries has relevance to oceanography, astrophysics and fluid dynamics in general. The dispersion relation describing the internal waves, $\omega = N\cos\theta$, relates the frequency ω of the internal waves to the buoyancy frequency N, leading to wave energy propagation with angle θ with the gravitational direction. However, unlike the more familiar surface waves, the dispersion relation does not restrict the wave vector $\mathbf{k} = k(\cos\theta, \sin\theta)$ other than being perpendicular to the group velocity (Phillips (1977), LeBlond & Mysak (1978) and Maas (2005)). The dispersion relation predicts that reflection of the internal waves at boundaries that are neither horizontal nor vertical, leads to a focusing or defocusing of the waves. Maas & Lam (1995) showed that in almost all confined fluid domains wave energy focusing dominates defocusing leading to a so called wave attractor. The experimental confirmation of such an attractor in a trapezoidal domain was presented in Maas *et al.* (1997) and reanalyzed by Lam & Maas (2007). In this experiment a nearly two-dimensional container, filled with a linearly stratified fluid, was vertically oscillated. Displacement of dye lines was used to visualize the internal dynamics. Starting from a rest position, an attractor

grew due to subharmonic parametric instability. Lam & Maas (2007) revealed that the amplitude of the attractor had an exponential growth reaching saturation. Contrary to the growth of a regular mode, the saturation time varied from position to position. They also proposed a causal connection between forcing of a surface seiche and the internal wave field.

Wave attractors are also found for the analogous class of inertial waves supported by homogeneous rotating fluids (Stewartson (1971) and Maas (2005)). Experimentally, inertial wave attractors have been observed and studied by Maas (2001) and Manders & Maas (2003). They considered a rotating rectangular tank with a sloping wall. From the comparison between the small tank of Maas (2001) and the larger tanks of Manders & Maas (2003), it appears that the attractor scale is independent of viscosity. This led Manders & Maas (2004) to the conclusion that the scales of the observed attractors are set by non-linear processes. However, in the theoretical work by Rieutord *et al.* (2001) and Rieutord *et al.* (2002) viscous processes were assumed to set the scale. Also Ogilvie (2005) considered the low-viscosity limit and provided a way of calculating the dissipation rate. In these models the dissipative spreading of the internal waves balances the geometric focusing due to reflections.

The purpose of this paper is to contribute to the discussion of what sets the attractor scale. For this we have conducted experiments and present the observed data mainly as spectra of the wave number k. We show that a balance exists between amplification by focusing at the sloping wall and dissipation at the highest wave numbers.

This paper is organized as follows. First we describe the experimental set-up in Section 2. After this we present in Section 3 the results from one particular experiment, that is representative for all experiments done. This section is followed by Section 4, in which we present two simple models that explain the observed behaviour.

2. Method

For the experiment we use a narrow rectangular tank with one sloping wall (angle of 27° with the vertical, see Table 1 for the dimensions). The tank is filled with a fluid whose density decreases linearly upwards. However, filling the tank with the well known double bucket technique is not possible as the domain has a cross section that varies with height. Instead, we use two computer controlled Masterflex peristaltic pumps that enable us to fill the tank with any desired stratification. Here, we present the findings of experiments performed with a fluid having constant buoyancy frequency N=3±0.1s^{-1}, measured by taking 10 density samples (see profile in Figure 1). Although pushing the limit of the Boussinesq approximation, using smaller values of N is found to make no difference other than that it affects the quality of the visualization.

To measure the motions in the fluid non-intrusively, we use the synthetic schlieren technique (Dalziel *et al.* (2000)). Synthetic schlieren measures the refractive index changes of a medium resulting from density perturbations. The principle is as follows. When a light-ray propagates through the fluid, the direction of propagation of this ray will be altered by the local value of the gradient of the index of refraction. A random dot pattern on a light bank 0.5 m behind the tank is monitored through the fluid. Density perturbations alter the refractive index and hence the direction of the light and are observed as apparent movement of the dots. Unfortunately, the refractive index of the air, between the tank and the point of observation, is also altered by unavoidable temperature fluctuations in the lab. This leads to some 'thermal noise' contaminating the observations. To record the apparent movements, we use a Jai CV-M4+CL camera (1.3 MPixel monochrome) positioned 8 m from the tank. Using an unperturbed reference image, the perturbed

Forcing period	T	5.1	s
Buoyancy frequency	N	3	s^{-1}
Dimensions tank	H_0 x W x L_{bot}	200 x 101 x 453	mm
Angle sloping wall	α	0.47	rad
Forcing frequency	ω_e	$2\pi/T = 1.23$	s^{-1}
Forcing amplitude	A_e	120	mm
Duration forced stage		$50 * T = 255$	s
Duration decay stage		$40 * T = 204$	s

Table 1: Parameters experiment.

position of the dots is translated into corresponding density gradient variations. For this comparison and data processing we use the DigiFlow software. As we observe the changes in the density gradient field, the stronger the undisturbed gradient field is, the more the dots appear to move. For this reason we present results of experiments with large N. We will present the observations as components of $\mathbf{b} = (b_x, b_z) = \nabla\rho'/(d\bar{\rho}/dz)$, i.e. the perturbation density gradient relative to the gradient of the unperturbed background stratification, $(d\bar{\rho}/dz)$.

Initially, we focused on internal wave generation by (subharmonic) parametric instability. The attractor reported by Maas *et al.* (1997) and Lam & Maas (2007) resulted from this sort of forcing of the fluid. To excite the instability, we use a vertically oscillating platform that carries the tank. However, with forcing amplitude A_e well below the theoretically predicted threshold of the parametric instability, another generation mechanism is already very effective. Owing to slight horizontal movements coming with the much stronger vertical motion, the stratified fluid in the tank starts sloshing a little. This barotropic motion is strong enough to generate baroclinic internal waves from its interaction with the slope. These waves have a frequency ω equal to that of the excitation, i.e. $\omega = \omega_e$. The results presented in this paper are on internal waves that are generated by this barotropic motion of the fluid.

The experiment is performed as follows. After 1 period, $T = 2\pi/\omega_e$, of linearly increasing the amplitude to A_e, the platform is vertically oscillated with frequency ω_e for $49T$. During this stage the camera is triggered to capture images at four fixed positions at each cycle of the oscillation. At $t = 50T$ the motion of the platform is linearly damped in two periods. Directly after the platform is at rest, the camera captures 24 frames s^{-1}(fps) of the decay stage, for 40 periods.

3. Results

We observe a wave attractor with the parameters given in Table 1. Figure 1 shows the result of harmonic analysis of b_x using the very accurate time series (24 fps) between $t = 52T$ and $t = 54T$. The amplitude is shown in Figure 1a. The orthogonal sections represented by the white dashed lines are for later use and will be referred to as S1-S4. The phase of the internal waves and the angles of the sloping wall, α, and of the internal waves, θ, are indicated in Figure 1b. Time series, as well as the angle θ, show that the internal wave frequency $\omega = \omega_e$. The measured density profile, $\bar{\rho}(z)$ is presented in Figure 1c.

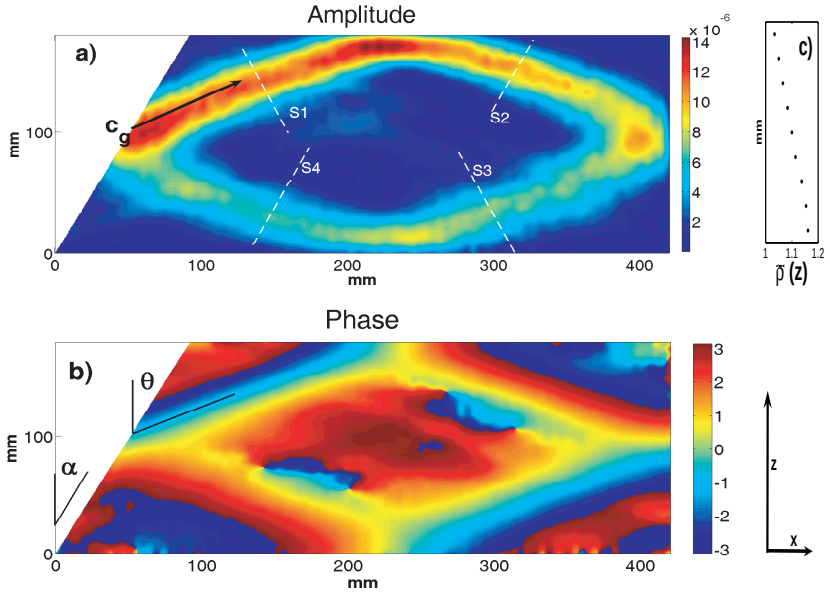

Figure 1: Harmonic analysis of the observations on b_x, a) shows the amplitude with the black arrow that points in the direction of energy propagation and the white lines indicate sections S1-S4. b) The phase and slope angle α and propagation angle θ with the vertical. c) Measured density profile, $\bar{\rho}(z)$.

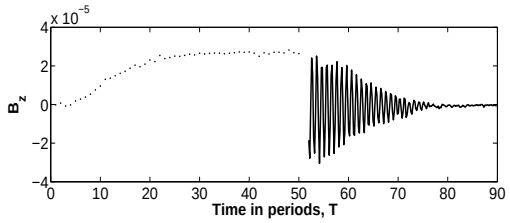

Figure 2: Observed growth and decay of b_z in the middle of S1. Note that the observation in the forced stage is once per period while the decay is shown in much more detail (125 obs/T).

The spatial structure of the perturbation and phase take the form of an internal wave attractor, as originally observed by Maas *et al.* (1997). The sloping wall focuses waves propagating in a clockwise sense. The phase propagation is perpendicular to the attractor branches indicating that the group velocity, and thus the energy, propagates as indicated by the black arrow. Following the energy from the sloping wall along the attractor, it is clear that the intensity of the density perturbation decreases, reaching a minimum just before the sloping wall. Also the intensification at the normal reflections is observed, being the result from (linear) superposition of the incident and reflected branches.

The attractor grows from the initial undisturbed state. The growth of b_z in the middle of S1 is shown in Figure 2. There is clearly an initial growth stage reaching an equilibrium after $t = 25T$. At $t = 50T$ the platform is halted and from $t = 52T$ the decay of the attractor is recorded in more detail than during the growth and equilibrium stages. Throughout the decay stage the frequency of the attractor remains well preserved, $\omega = \omega_e \pm 0.05\text{s}^{-1}$. The dispersion relation therefore ensures that θ is preserved as can be

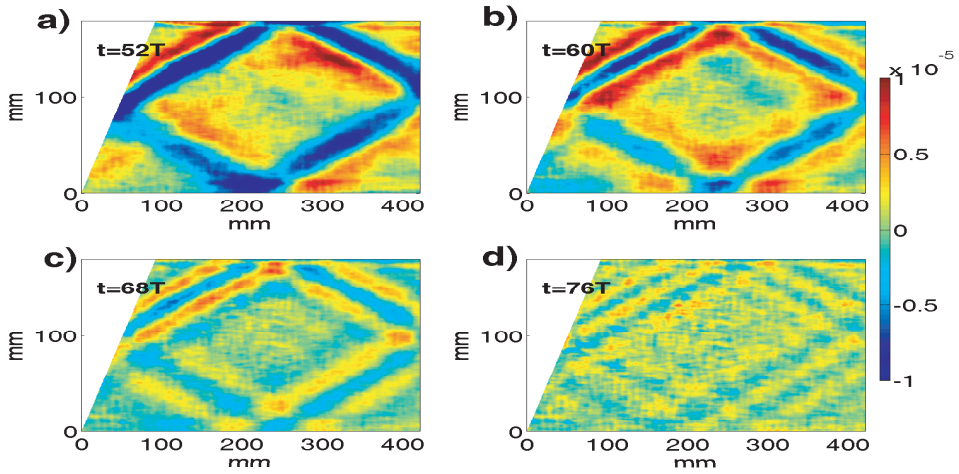

Figure 3: Four snapshots b_z, at a) $t = 52T$ (just after oscillation), b) $t = 60T$, c) $t = 68T$ and d) $t = 76T$, showing that the shorter wavelengths decay later.

seen in Figure 3, where four snapshots of the decay stage are presented. These snapshots suggest that the wave length of the attractor decreases and confirm that the magnitude of the perturbation decays everywhere in the tank.

3.1. *Spectral analysis*

The observed change in wave length suggests value in analyzing the wave number spectrum. Hereto, we introduce a coordinate system that aligns with the branches and the wave vector $\mathbf{k} = k(\cos\theta, \sin\theta)$ in the x, z-plane. We assume that b_z along S1, $B = b_z(\mathrm{S1})$, can be written as

$$B(\eta, t) = \int A(k) e^{i(k\eta - \omega t)} dk, \tag{3.1}$$

using $\eta = x\sin\theta - z\cos\theta$ for S1 (see Figure 1). Note that η is redefined along S2-S4. Using η as our independent spatial variable we then perform a spatial Fourier analysis for each of S1-S4.

The spectra of S1-S4 at fixed time $t = 50T$ are presented in Figure 4a. Comparing the spectra, we see a clear shift of the spectral peak towards low wave numbers as we move from S1 to S4. In Figure 3a, at $t = 52T$, a broadening of the branches is seen going from S1 and S4. From the spectra we learn that the high wave numbers disappear and the low wave numbers remain. This viscous broadening of the attractor branches corresponds with the decrease in dominant wave number.

However, in the decay stage we observed that the low wave numbers (large wave lengths) disappeared. The spectra along S1 for the same times during the decay as in Figure 3 are shown in Figure 4b. Indeed, apart from a decrease of total amplitude, we here see a clear shift towards the *high* wave numbers

Spectra for S1 of growth, equilibrium and decay stages are combined in Figure 5, which shows the 'energy', $|A(k)|^2$ (false colour) as a function of wave number (horizontal axis) and time (vertical axis). At the start of the experiment, $t = 0$, there are no waves. The spectrum grows from the lowest wave numbers towards the high wave numbers.

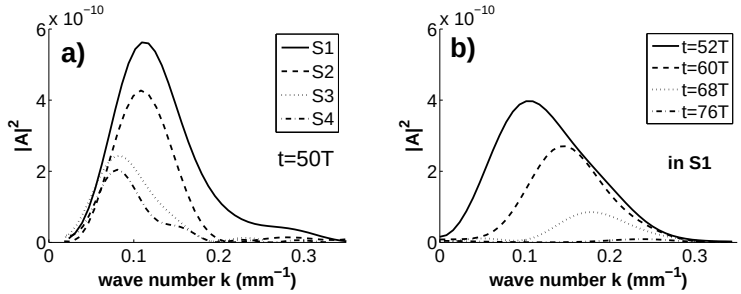

Figure 4: a) Viscous broadening from S1 to S4 at t=50T. b) Time evolution of the spectrum along S1 at $t = 52T$, $60T$, $68T$ and $70T$.

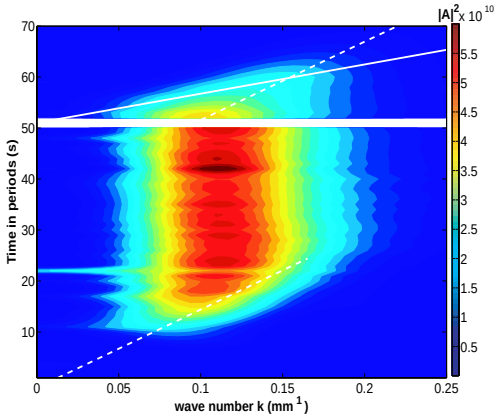

Figure 5: Evolution of the wave number spectrum along section S1 during the whole experiment. The lines indicate t_{loop} (solid white line) and t_{sum}(dashed white line)

By $t = 25T$ the spectrum reaches equilibrium, coinciding with the saturation of the amplitude of the density gradient perturbation in Figure 2. After the oscillation of the platform is stopped, between $t = 50T - 52T$, we observe the decay of the spectrum. It is clear that, as time passes, the energy at low k values decays fastest, while that at high wave numbers lingers on. This is in accordance with the qualitative observation of the structure in Figure 3. It is worth noting that high wave number energy exist from the time the spectrum reaches equilibrium onwards. However, the energy at high wave numbers is overshadowed by that of the stronger low wave numbers until the forcing is halted. Only when the high wave numbers become dominant they set the scale of the attractor branch.

4. Simple models

In this section we present a model explaining the observed characteristics of the wave number spectrum in the growth and decay stage. Subsequently, the equilibrium spectrum will be addressed.

During the growth and equilibrium stages of the experiment the largest waves are driven by sloshing of the fluid in the tank. Propagation of the waves inevitably leads to

reflection at the walls. Every time these waves reflect at the sloping wall in a clockwise (focusing) sense, their wave number increases (wave length decreases) by a factor

$$\gamma = \frac{\sin(\theta + \alpha)}{\sin(\theta - \alpha)} = 1.6. \tag{4.1}$$

The amplitude of the wave is amplified by the same ratio, as conservation laws demand. This results in a continuous transfer of energy towards the high wave numbers. This transfer is also dependent on group speed $c_g(k) = |\mathbf{c}_g| = N \sin\theta / k$, which decreases with increasing k. We define the different loop times, the time needed for the energy in wave number k to travel once around the attractor with length L_a:

$$t_{loop}(k) = \frac{L_a}{c_g(k)} = \frac{L_a k}{N \sin\theta}. \tag{4.2}$$

We also define a series of focused wave numbers

$$k_n = \gamma k_{n-1} = \gamma^n k_0 \tag{4.3}$$

with $k_0 = 2\pi/H$, the wave number corresponding to the scale of the basin. Combining (4.2) and (4.3) we define

$$t_{sum}(k_n) = \sum_{i=0}^{n-1} t_{loop}(k_i) = \sum_{i=0}^{n-1} \frac{L_a \gamma^i k_0}{N \sin\theta} = \frac{L_a k_0}{N \sin\theta} \frac{\gamma^n - 1}{\gamma - 1}. \tag{4.4}$$

This is the time passed since the wave had wave number k_0. The increase in wave number and amplitude is not unlimited. Viscosity acts on the waves and becomes more efficient at high wave numbers. This process is the sink for the energy put into the system. A balance between generation/amplification and dissipation is reached in the equilibrium stage, addressed in the next section. When we stop the oscillation, and thus the energy input, the transfer of energy towards high k continues. The source for the lowest wave number (k_0) however, is now gone. This ongoing transfer from low to high k is seen in Figure 5. Here we see that in the decay stage the high values of k are sustained much longer at a 'saturation level' than the low wave numbers.

We calculate $t_{loop}(k_n)$ and $t_{sum}(k_n)$, with $L_a = 800$ mm . The solid white line in Figure 5 represents t_{loop}, starting from $t = 52T$ at k_0. It is clear that this line is aligned with the outer flank of the spectrum. This means that after a wave with certain k has reached the slope again it disappears (decays) below noise level. The dashed white lines represent t_{sum} starting from arbitrary times. We can see that these lines align with the peak shift in the spectrum in both growth and decay stage.

4.1. *Simple model equilibrium spectrum*

We now address the observed equilibrium spectrum. A balance is assumed between amplification of the amplitude through reflection off the slope and dissipation at the high wave numbers. Rieutord *et al.* (2001) considered a travelling wave packet along an attractor and described its damping by viscosity as:

$$A(k) = A_0 e^{-\nu k^2 t}. \tag{4.5}$$

This follows by inserting (3.1) into a diffusion equation $\partial B/\partial t = \nu \partial^2 B/\partial \eta^2$. The viscous damping is of influence over multiple wave periods, $t \gg T$, and we will model damping between successive reflections from the slope for a given packet discretely. We do this

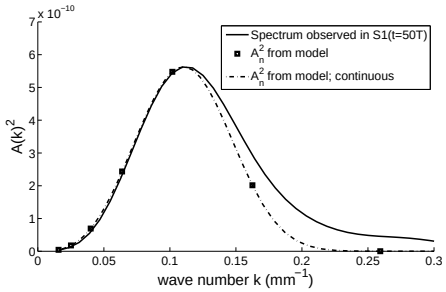

Figure 6: Comparison of the observed equilibrium spectrum and A_n^2 from (4.6)

by sampling (4.5) at each loop around the attractor. At the sloping wall the wave is focused into a smaller wave with higher wave number k_n. Upon reflection the energy flux is preserved, $F = c_g U^2/2$ =constant, where current speed U scales with the perturbation density (Phillips 1977). But, recall that, A refers to the amplitude of the perturbation density *gradient*, hence $U \propto A/k$ implying $A^2 k^{-3}$ =constant. From this we find the recursive relation $A(k_n)^2 \equiv A_n^2 = \gamma^3 A_{n-1}^2$. Combining this description of focussing with that of the dissipation in (4.5) and sampling each loop, (4.2), then leads to:

$$A_n^2 = \gamma^3 \exp\left[\frac{-2\nu L_a k_n^3}{N \sin\theta}\right] A_{n-1}^2 = \gamma^{3n} \exp\left[-\Upsilon(\gamma^{3n}-1)\right] A_0^2, \tag{4.6}$$

with $\Upsilon = [2\nu/(H^2 N)][L_a/H][(2\pi)^3/((\gamma^3-1)\sin\theta)]$. We calculate subsequent wave numbers, starting from k_0 and appropriate values for our experiment (ν =1 mm^2/s and $\omega = 2\pi/5.1$ s^{-1}). We find that in eight focusing reflections the largest wave length is transformed into the smallest wave length found in our observed spectrum. In Figure 6 we plot the observed equilibrium spectrum along S1 (line) and our computed A_n^2 from (4.6) (squares). The dashed line indicates the spectrum where n is treated as a continuous variable. It is clear that for the lowest wave numbers the amplification by focusing is dominant, left side of the spectrum $\propto \gamma^{3n}$, and that dissipation mainly acts on the high wave numbers $\propto \exp\left[-\Upsilon(\gamma^{3n}-1)\right]$. The observed and modelled spectrum have similar behaviour and indeed show that our assumption of a balance between focusing and viscous dissipation is reasonable. We argue that the difference between observation and model on the dissipation side of the spectrum is caused by noise. Note that (4.6) fixes the structure of the spectrum but not its scale. The amplitude A_0 remains arbitrary and we have matched it to that of our experimental spectrum. While we do not know the actual A_0 for our experiments, we expect that the amplitude of the forcing will play a dominant role in determining A_0 and hence the maximum value of $A(k)$.

5. Conclusion and discussion

From this work it is clear that the observed structure of internal wave attractors can be explained through the linear processes of focusing and viscous diffusion. Focusing takes the energy from the relatively large basin scale, that is most strongly excited by the forcing, to smaller scales where viscous dissipation dominates, overwhelming any further focusing. In these experiments the internal waves at the basin scale were undoubtedly linear. Whilst the wave amplitude increased as the wave length decreased during the first few cycles of the attractor, this was not here sufficient to generate any strong nonlinearities.

In their laboratory experiments, Manders & Maas (2004) observed that the attractor scaled with the tank size. From this they concluded that the scale of the attractor is independent of viscosity. Paradoxically, in the astrophysical context, Rieutord *et al.* (2001) and Ogilvie (2005) found that the scale of the attractor depends on viscosity. We find that the scale of the attractor is set by the wave length of $k_{peak} = \gamma^{n_{peak}} k_0$ at the spectral peak. Neglecting the discrete nature of n, the value of n_{peak} is obtained when the derivative of (4.6), with respect to n vanishes. As $L_a \propto H$, and recalling that $k_0 \propto H^{-1}$, we find that $n_{peak} \propto -\ln(\nu/NH^2)$. Using appropriate values as before, this relation shows that the attractor scale, $k_{peak}^{-1} \propto H^{1/3}$, shifts strongly over the range of tank sizes ($200 < H < 1000$ mm) considered by Manders & Maas (2004). Comparing their suggested linear dependence on H of the attractor scale with the $H^{1/3}$ dependence in our model, we find an error of less than 5% over the range they observed. For the very large astrophysical H, the position of the peak is relatively insensitive to the geometry. In this case, the value of viscosity ν sets the value of k_{peak}, in accordance with the predicted dependence of the attractor scale on viscosity.

We thank the support of technicians at both NIOZ and DAMTP. J.H. is supported by a grant from the Dutch National Science Foundation N.W.O. in the Dynamics of Patterns program.

REFERENCES

Dalziel, S. B., Hughes, G. O. & Sutherland, B. R. 2000 Whole field density measurements by 'synthetic schlieren'. *Experiments in Fluids* **28**, 322–335.

Lam, F.-P. A. & Maas, L. R. M. 2007 Internal wave focusing revisited; a reanalysis and new theoretical links. *Fluid Dynamics Research* **in press**.

LeBlond, P. H. & Mysak, L. A. 1978 *Waves in the Ocean*. Elsevier Oceanography Series.

Maas, L. R. M. 2001 Wave focussing and ensuiing mean flow due to symmetry breaking in rotating fluids. *Journal of Fluid Mechanics* **437**, 13–28.

Maas, L. R. M. 2005 Wave attractors: linear yet nonlinear. *International Journal of Bifurcation Chaos* **15**, 2757–2782.

Maas, L. R. M., Benielli, D., Sommeria, J. & Lam, F.-P. A. 1997 Observation of an internal wave attractor in a confined stably-stratified fluid. *Nature* **388**, 557–561.

Maas, L. R. M. & Lam, F.-P. A. 1995 Geometric focusing of internal waves. *Journal of Fluid Mechanics* **300**, 1–41.

Manders, A. M. M. & Maas, L. R. M. 2003 Observations of inertial waves in a rectangular basin with one sloping boundary. *Journal of Fluid Mechanics* **493**, 59–88.

Manders, A. M. M. & Maas, L. R. M. 2004 On the three-dimensional structure of the inertial wave field in a rectangular basin with one sloping boundary. *Fluid Dynamics Research* **35**, 1–21.

Ogilvie, G. I. 2005 Wave attractors and the asymptotic dissipation rate of tidal disturbances. *Journal of Fluid Mechanics* **543**, 19–44.

Phillips, O. M. 1977 *The Dynamics of the Upper Ocean, 2nd ed.*. Cambridge University Press.

Rieutord, M., Valdettaro, L. & Georgeot, B. 2001 Inertial waves in a rotating spherical shell: attractors and asymptotic spectrum. *Journal of Fluid Mechanics* **435**, 103–144.

Rieutord, M., Valdettaro, L. & Georgeot, B. 2002 Analysis of singular inertial modes in a spherical shell: the slender toroidal shell model. *Journal of Fluid Mechanics* **463**, 345–360.

Stewartson, K. 1971 On trapped oscillations of a rotating fluid in a thin spherical shell. *Tellus* **XXII (6)**, 506–510.

Bibliography

Antenucci, J. P., Imberger, J. & Saggio, A. 2002 Seasonal Evolution of the Basin-Scale Internal Wave Field in a Large Stratified Lake. *Limnology and Oceanography* **45** (7), 1621–1638.

Arfken, G. 1995 *Mathematical Methods for Physicists*, 5^{th} edn. Harcourt Academic Press, San Diego, CA.

Baines, P. G. 1973 The generation of internal tides by flatbump topography. *Deep-Sea Res.* **20** (2), 179–2060.

Bell, T. H. 1975 Topographically generated internal waves in the open ocean. *J. Geophys. R.* **80**, 320–327.

Benielli, D. & Sommeria, J. 1998 Excitation and breaking of internal gravity waves by parametric instability. *Journal of Fluid Mechanics* **374**, 117–144.

Cooley, J. W. & Tukey, J. W. 1965 An algorithm for the machine calculation of complex fourier series. *Mathematics of Computation* **19** (90), 297–301.

Dalziel, S. B., Hughes, G. O. & Sutherland, B. R. 2000 Whole-field density measurements by 'synthetic schlieren'. *Experiments in Fluids* **28**, 322–335.

Drijfhout, S. & Maas, L. R. M. 2007 Impact of channel geometry and rotation on the trapping of internal tides. *J. of Phys. Oceanogr.* pp. 1–60, in press.

Fricker, P. D. & Nepf, H. M. 2000 Bathymetry, stratification, and internal seiche structure. *J. Geophys. R.* **105**, 14237–14252.

Gerkema, T., Lam, F.-P. A. & Maas, L. R. M. 2004 Internal tides in the Bay of Biscay: conversion rates and seasonal effects. *Deep Sea Research Part II: Topical Studies in Oceanography* **51**, 2995–3008.

Gill, A. E. 1981 *Atmosphere-Ocean Dynamics*. *International Geophysics Series* . Academic Press.

Gostiaux, L. 2006 Étude expérimentale des ondes de gravité internes en presśence de topographie. Émission, propagation, réflection. PhD thesis.

Hazewinkel, J., van Breevoort, P., Maas, L. R. M., Doelman, A. & Dalziel, S. B., ed. 2007 *Paper submitted to the Fifth International Symposium on Environmental Hydraulics, Arizona*.

Horn, W. & Meincke, J. 1976 Note on the tidal current field in the continental slope area off Northwest Africa. *Mem Soc Roy Sci Liege* **6**, 31–42.

Huthnance, J. M.and Baines, P. G. 1982 Tidal currents in the northwest African upwelling region. *Deep-Sea Res.* **29** (A), 285–306.

Lam, F.-P. A. & Maas, L. R. M. 2007 Internal wave focusing revisited; a reanalysis and new theoretical links. *Fluid Dyn. Res.* pp. 1–31, in press.

Lerczak, J. A., Winant, C. D. & Hendershott, M. C. 2003 Observations of the semidiurnal internal tide on the southern California slope and shelf. *Journal of Geophysical Research (Oceans)* **108**, 13–1.

Maas, L. R. M. 2005 Wave attractors: Linear yet nonlinear. *Int. J. Bifurcation and Chaos* **15** (9), 2757–2782.

Maas, L. R. M., Benielli, D., Sommeria, J. & Lam, F.-P. A. 1997 Observation of an internal wave attractor in a confined, stably stratified fluid. *Nature* **388**, 557–+.

Maas, L. R. M. & Lam, F.-P. A. 1995 Geometric focusing of internal waves. *Journal of Fluid Mechanics* **300**, 1–41.

Mowbray, D. E. & Rarity, B. S. H. 1967 A theoretical and experimental investigation of the phase configuration of internal waves of small amplitude in a density stratified liquid. *Journal of Fluid Mechanics* **28**, 1–16.

Munk, W. & Wunsch, C. 1998 Abyssal recipes II: energetics of tidal and wind mixing. *Deep Sea Research Part I: Oceanographic Research Papers* **45** (12), 1977–2010.

Phillips, O. 1977 *The dynamics of the upper ocean*. Cambridge University Press.

Rattray, M., J. 1960 On the coastal generation of internal tides. *Tellus* **12**, 5461.

Stewartson, K. 1971 On trapped oscillations of a rotating fluid in a thin spherical shell. *Tellus* **23**, 506–+.

Swart, A. 2007 Internal Waves and the Poincaré Equation. PhD thesis.

Turner, J. S. 1973 *Buoyancy Effects in Fluids*. London, England: Cambridge University Press.

Weyl, F. J. 1954 Analysis of optical methods. In *Physical measurements in gas dynamics and combustion* (ed. R. W. Ladenburg), pp. 3–25. Princeton University Press.

Acknowledgements

Deze scriptie is niet op een eiland tot stand gekomen en velen hebben bijgedragen aan mijn welbevinden gedurende de afgelopen maanden. Als eerste wil ik mijn begeleider Leo Maas bedanken. Leo, ik heb met veel plezier aan mijn afstuderen gewerkt. Dank voor je geduld, dat je altijd meedacht en beschikbaar was voor moeilijke en makkelijke vragen. Regelmatig werd ik uitgedaagd om een kwalitatieve uitleg ook daadwerkelijk te testen, om door te gaan waar ik eigenlijk wilde stoppen. En vaak ontdekte ik dan hoeveel er te leren valt als je je echt iets afvraagt en hoe leuk en inspirerend dit is.
Jeroen, bedankt voor het gezelschap, met name tijdens de maanden in Cambridge, waar ik met veel plezier aan terugdenk. Ik denk dat we een goed team vormden en wens je nog veel succes tijdens de komende twee jaar van je promotie.
Verder wil ik iedereen op het NIOZ bedanken, in het bijzonder de afdeling Fysica. Ik heb me er het afgelopen jaar erg thuis gevoeld, mede dankzij de altijd goede en ontspannen sfeer.
Minke, zonder jou was ik nu een stuk bleker geweest. Hoe had het zonder jou gemoeten?
Mijn ouders dank ik voor de steun en sponsoring, het is een fijn idee dat jullie geloven dat het goed is/komt, wat ik ook doe.
Verder wil ik mijn vrienden zeggen dat ik alle mailtjes die ik de afgelopen maand heb opgespaard als 'unread' met veel plezier ga beantwoorden.

I had a wonderful time in Cambridge, thanks everybody at the GK Batchelor Laboratory, especially Stuart Dalziel. And Mario.

Samenvatting

In deze scriptie bespreek ik een serie experimenten met interne golfaantrekkers. De experimenten vormden een onderdeel van het project “Internal wave patterns in 3D”.
Interne zwaartekrachtsgolven zijn mogelijk in gelaagd water. In continu gelaagd water planten interne golven zich voort onder een hoek met de zwaartekrachtsrichting. Deze hoek is afhankelijk van de frequentie van de golven. Als interne golven reflecteren tegen een wand, dan blijft deze hoek behouden, aangezien de frequentie ongewijzigd blijft. Reflectie tegen een wand die niet horizontaal of verticaal is, leidt tot het focusseren (defocusseren) van de golf: De reflectie gaat gepaard met een afname (toename) van de golflengte en een toename (afname) van de amplitude van de snelheid. In een gesloten geometrie, met tenminste één focusserende wand, overheerst in de meeste gevallen het focusseren het defocusseren. Dit leidt tot het bestaan van golfaantrekkers. Dit is een gesloten pad waarnaar alle golfenergie wordt aangetrokken. Theoretisch gezien leid dit tot singulariteiten in het snelheids- en drukveld op de aantrekker. In de natuur kunnen golfaantrekkers worden verwacht in half-open kanalen en in meren, hoewel er op dit gebied nog weinig metingen zijn verricht.

De interne golf aantrekkers zijn gemeten met behulp van ’synthetic schlieren’. Deze methode maakt gebruik van het feit dat het pad dat licht aflegt wijzigt als de dichtheidsgradiënten in het medium veranderden. De (met een camera) gemeten variaties van het pad van het licht zijn gebruikt om dichtheidsvariaties, als gevolg van interne golven, te kwantificeren.
De meeste experimenten zijn gedaan in een platte (semi-2D) tank met één schuine wand. De interne golven werden opgewekt met een verticaal oscillerende tafel. Aanvankelijk werd er geprobeerd golven op te wekken d.m.v. parametrische excitatie, de tafel bleek echter niet voldoende forcering te bieden voor dit mechanisme. Maar de verticale beweging ging gepaard met een kleine horizontale oscillatie. Deze oscillatie veroorzaakte een barotrope beweging in de tank, deze beweging werd langs de schuine wand deels omgezet in interne golven. Dit mechanisme bleek sterk genoeg voor het ontstaan van interne golfaantrekkers.
De forceringsfrequentie en -amplitude, gelaagdheid en geometrie zijn gevarieerd tijdens de experimenten. In de experimenten waarbij interne golfaantrekkers zijn gevonden, bleek de aantrekker na ongeveer 20 oscillaties (van de tafel) een evenwicht te bereiken. Tijdens de opbouw van een golfaantrekker evolueerde het dominante golfgetal richting een groter golfgetal, tot er een evenwicht was bereikt tussen de productie en dissipatie van grotere golfgetallen. Interne golven met een groter golfgetal hebben een lagere groepssnelheid. Het kost dus meer tijd voordat deze de aantrekker zijn rondgegaan, waardoor viscositeit meer tijd heeft om op de golven te werken. Verder impliceren kortere golven een grotere laterale schuifspanning. Deze twee mechanismen zorgden ervoor dat er bij een bepaald golfgetal een evenwicht ontstond met de productie van golfgetallen a.g.v. het focusseren. De vorm van het evenwichtsspectrum bleek voornamelijk bepaald te worden door de

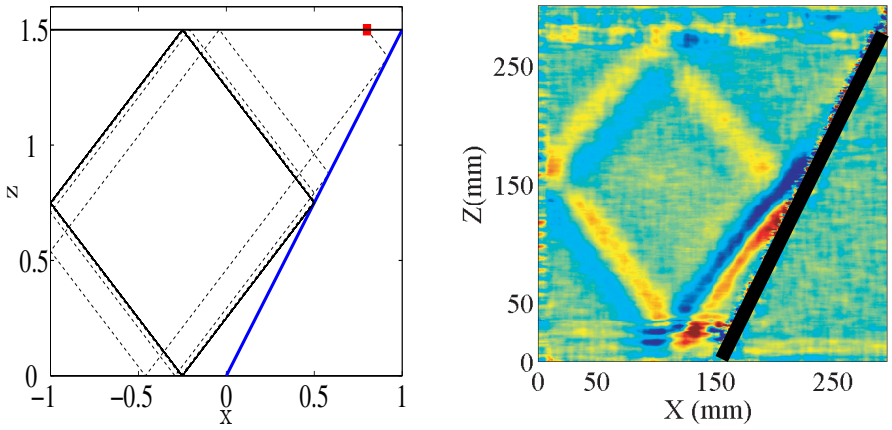

(a) (b)

Figure B.1: (a) een theoretische aantrekker: een straal, geïnitieerd bij het rode vierkant, wordt via reflecties aangetrokken tot de ruit (zwarte ononderbroken lijnen), (b) een gemeten aantrekker, de kleuren geven storingen in de vertical gradiënten van het dichtheidsveld weer.

lengte van de aantrekker en niet door de amplitude van de forcering (i.a.w. de hoeveelheid ingebrachte energie). Nadat de forcering was stopgezet ontwikkelde het golfgetal spectrum zich verder richting de grotere golfgetallen. De snelheid van de evolutie van de kleine naar de grotere golfgetallen, tijdens de opbouw en het verval, bleek bepaald te worden door de lengte van de aantrekkers, omdat deze de tijd bepaalt die een golf nodig heeft om de aantrekker rond te gaan en dus de tijd tussen de productie van een golflengte en de annihilatie (a.g.v. het focusseren).
De vorm en het bestaan van de golfaantrekkers bleek goed te kunnen worden voorspeld met de bestaande niet-visceuze theoretische beschrijving.
Een aantal experimenten werden uitgevoerd met meer uitgebreide (in 3D) tanken. Aantrekkers werden ook hier geobserveerd, maar de afstand tussen camera en tank bleek te klein, dit zorgde voor grote meetfouten. In het parabolische kanaal werd een aantrekker gevonden die overeenkomsten vertoonden met resultaten uit een eerder numeriek model. In deze scriptie bespreek ik verder hoe de experimentele opstelling kan worden verbeterd, zodat er uiteindelijk metingen gedaan kunnen worden van golfaantrekkers in 3D.